PFC/RR-95-2 DOE/ET-51013-310

Axisymmetric Control in Alcator C-Mod

Gerasimos Tinios

January 1995

This work was supported by the U. S. Department of Energy Contract No. DE-AC02-78ET51013. Reproduction, translation, publication, use and disposal, in whole or in part by or for the United States government is permitted.

Axisymmetric Control in Alcator C–Mod

by

GERASIMOS TINIOS

B.S., Nuclear Engineering, Rensselaer Polytechnic Institute (1985)

Submitted to the Department of Nuclear Engineering
in partial fulfillment of the requirements for the degree of

Doctor of Philosophy

at the

MASSACHUSETTS INSTITUTE OF TECHNOLOGY

January 1995

Signature of Author .....
Department of Nuclear Engineering
January 18, 1995

Certified by .....
Ian H. Hutchinson
Professor, Department of Nuclear Engineering
Thesis Supervisor

Certified by .....
Jeffrey P. Freidberg
Professor, Department of Nuclear Engineering
Thesis Reader

Accepted by .....
Allan F. Henry
Chairman, Departmental Graduate Committee

Axisymmetric Control in Alcator C–Mod

by

GERASIMOS TINIOS

Submitted to the Department of Nuclear Engineering
on January 18, 1995, in partial fulfillment of the
requirements for the degree of
Doctor of Philosophy

ABSTRACT

This thesis investigates the degree to which linear axisymmetric modeling of the response of a tokamak plasma can reproduce observed experimental behavior. The emphasis is on the vertical instability. The motivation for this work lies in the fact that, once dependable models have been developed, modern control theory methods can be used to design feedback laws for more effective and efficient tokamak control. The models are tested against experimental data from the Alcator C–Mod tokamak. A linear model for each subsystem of the closed–loop system constituting an Alcator C–Mod discharge under feedback control has been constructed. A non–rigid, approximately flux–conserving, perturbed equilibrium plasma response model is used in the comparison to experiment. A detailed toroidally symmetric model of the vacuum vessel and the supporting superstructure is used. Modeling of the power supplies feeding the active coils has been included. Experiments have been conducted with vertically unstable plasmas where the feedback was turned off and the plasma response was observed in an open–loop configuration. The closed–loop behavior has been examined by injecting step perturbations into the desired vertical position of the plasma.

The agreement between theory and experiment in the open–loop configuration was very satisfactory, proving that the perturbed equilibrium plasma response model and a toroidally symmetric electromagnetic model of the vacuum vessel and the structure can be trusted for the purpose of calculations for control law design. When the power supplies and the feedback computer hardware are added to the system, however, as they are in the closed–loop configuration, they introduce nonlinearities that make it difficult to explain observed behavior with linear theory. Nonlinear simulation of the time evolution of the closed–loop experiments was able to account for the discrepancies between linear theory and experiment.

Thesis Supervisor: Ian H. Hutchinson
Title: Professor, Department of Nuclear Engineering

Thesis Reader: Jeffrey P. Freidberg
Title: Professor, Department of Nuclear Engineering

Acknowledgments

During my long years as a graduate student, I have always considered it my privilege to be working at the Plasma Fusion Center, not only for the access that it gave me to state–of–the–art science and engineering, but also for the open and "empowering" working environment that it is.

I would like, first, to express my admiration for my advisor, Prof. I. Hutchinson, and my reader Prof. J. Freidberg. They have been a constant inspiration for me.

I would like to thank Dr. S. Horne and Dr. S. Wolfe for generously offering me their time and advice.

I would like to thank my fellow students, who made my time at the Plasma Fusion Center more pleasant and, in particular, G. Svolos, K. Kupfer, T. Mogstad, R. Kirkwood, N. Gatsonis, D. Humphreys, C.Teixeira, D. Lo, P. O'Shea, J. Reardon, J. Miller.

Finally, and most of all, I wish to thank my parents. This would not have been possible without them.

Contents

List of Figures

List of Tables

Chapter 1

Introduction

1.1 General Background

The concept of magnetic plasma confinement relies on the fact that charged particles are constrained to gyrate around magnetic field lines making it difficult for them to move perpendicularly to the magnetic field. Since motion along the magnetic field is free, one wants to close the magnetic field lines onto themselves or have them lie on a closed surface within the confinement device, thereby preventing the particles from leaving it. In the tokamak, see Fig. 1-1, this is achieved by bending a tube of magnetic field lines into a torus. The magnetic field is mainly in the toroidal direction, but there is a smaller poloidal component created by the current flowing toroidally in the plasma. This current is necessary to complete the confinement configuration.

One can follow the equations of motion of single particles and arrive via ensemble averaging at a set of kinetic equations for the distribution function over space and velocity of each species in the plasma. These are known as the Boltzmann equations, which, together with Maxwell's equations, are a complete description, provided one knows the effect of collisions on the distribution function.

Ideal magnetohydrodynamics (MHD) is a fluid model to describe certain basic macroscopic equilibrium and stability phenomena in a plasma. It results after taking velocity moments of the Boltzmann-Maxwell equations and rests on the following three assumptions:

- we are dealing with plasmas with thermal velocities much smaller than the speed of light and phenomena with phase velocities much smaller than the speed of light, so that the displacement current in Ampere's equation can be neglected.
- electron inertia is negligible, so that electrons respond quickly enough to cancel any charge imbalance and the net charge in Poisson's equation is zero. This is known as the quasineutrality condition. This assumption also implies that we are dealing with slow phenomena.
- the plasma is so dominated by collisions that it can be described by a scalar, isotropic pressure.

The first two assumptions are well justified for fusion plasmas for most macroscopic phenomena of interest and lead to a set of single fluid equations. The third assumption is not always justified for fusion plasmas, but, it turns out that many macroscopic phenomena of interest are not dependent on the evolution of the pressure tensor. The ideal MHD equations can be summarized as:
The continuity equation:

$$\frac{d\rho}{dt} = -\rho\nabla\cdot\vec{v} \tag{1.1}$$

where ρ is the plasma density and $\vec{v}$ is the fluid velocity.
The momentum equation:

$$\rho\left(\frac{d\vec{v}}{dt}\right) = \vec{J}\times\vec{B} - \nabla p \tag{1.2}$$

where $\vec{J}$ is the plasma current density and $\vec{B}$ is the magnetic field.

The state equation:

$$\left(\frac{dp}{dt}\right) = \gamma p \nabla \cdot \vec{v} \tag{1.3}$$

where $\gamma = 5/3$.

Ohm's law:

$$\vec{E} + \vec{v} \times \vec{B} = \vec{0} \tag{1.4}$$

All the above quantities are functions of space and time, and $\frac{d}{dt} = \frac{\partial}{\partial t} + \vec{v} \cdot \nabla$ is the Lagrangean derivative.

In steady state, the momentum equation says that the Lorentz force is balanced everywhere by the pressure gradient. If we define the poloidal flux, $\psi(R, Z)$ as the total magnetic flux flowing through a horizontal circular loop of radius R centered at the tokamak axis at a distance Z from the midplane, the magnetic field can be written in terms of this flux and, using Ampere's law, the momentum balance equation can be rewritten as:

$$R^2 \nabla \cdot \left(\frac{\nabla \psi}{R^2}\right) = -\mu_0 R^2 \frac{dp}{d\psi} - F \frac{dF}{d\psi} \tag{1.5}$$

where $F \equiv RB_\phi$ and B_ϕ is the toroidal field. Eq. 1.5 is known as the Grad–Shafranov equation describing axisymmetric toroidal plasma equilibrium. Note that F and the pressure are functions of ψ alone, i.e., they are constant on contours of constant poloidal flux. Also note that the right hand side in Eq. 1.5 can be written as $-RJ_\phi(\psi)$ where J_ϕ is the toroidal plasma current. Given $p(\psi)$ and $F(\psi)$ profiles and a set of external currents, Eq. 1.5 determines the shape of the flux contours. For the plasma area, these are usually closed concentric contours. The innermost contour is known as the magnetic axis of the plasma.

Linearized MHD stability can be studied when we consider perturbations from an equilibrium with zero fluid velocity ($\vec{v} = 0$). All perturbed quantities can be described in terms of the plasma displacement, $\vec{\xi}$, which defines the perturbed fluid

velocity, $\vec{v}_1 \equiv \left(\frac{d\vec{\xi}}{dt}\right)$. When the equilibrium is toroidally symmetric, this can be expressed as a sum of normal modes by writing:

$$\vec{\xi}(\vec{x},t) = \vec{\xi}_0(r,\theta)\exp\left(in\phi + i\omega t\right) \tag{1.6}$$

where n is the toroidal number of the mode. Definitions of the spatial coordinates are given in Fig. 1-1. The plasma is stable if the imaginary part of the eigenvalue, ω, is non–negative for all modes of the system. Instability can arise from pressure gradients or from current flowing parallel to the field.

The advantages of the tokamak over other magnetic confinement schemes for controlled nuclear fusion have always been shadowed by the fact that the maximum β_t allowable for magnetohydrodynamic (MHD) stability is low. Being the ratio of plasma to magnetic pressure, β_t is a measure of performance over cost and is directly related to how suitable a confinement scheme is for efficient power generation. This limit arises from the so–called ballooning modes and external kink modes. Ballooning modes are high–n pressure–driven modes due to the unfavorable field curvature characteristic of a tokamak. Kink modes can be driven either by pressure gradients or by the current, and they dictate limits both on β_t and total plasma current. Overall field stability can be made favorable by shaping the plasma cross–section. It has been shown, both theoretically and experimentally in the past ten years [1, 2, 3, 4, 5], that, elongation and triangularity of the plasma cross–section, allows for a higher plasma current which improves MHD β_t–limits and confinement. For this reason, most tokamaks built in the 1980's and 1990's have shaped plasma cross–sections. Examples are: JET in the U.K., ASDEX–U in Germany, JT–60U in Japan, DIII–D, Alcator C–Mod, and PBX–M in the U.S.A., and TCV in Switzerland. Note that, except for JET, all other experiments are successors to or modifications of circular cross–section tokamaks that existed previously in the same research centers.

Axisymmetric plasma perturbations (toroidal mode number $n = 0$) deserve

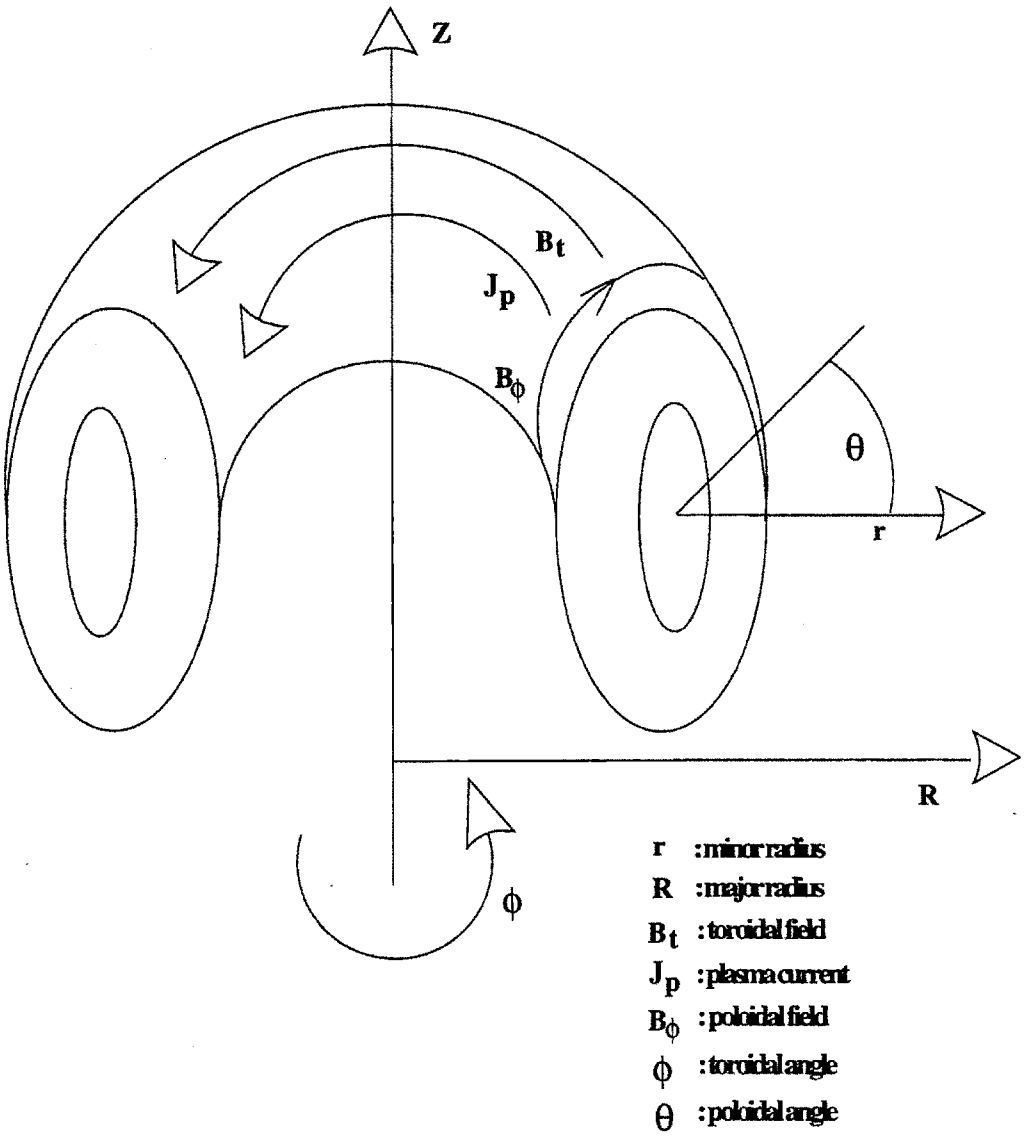

Figure 1-1: Tokamak geometry.

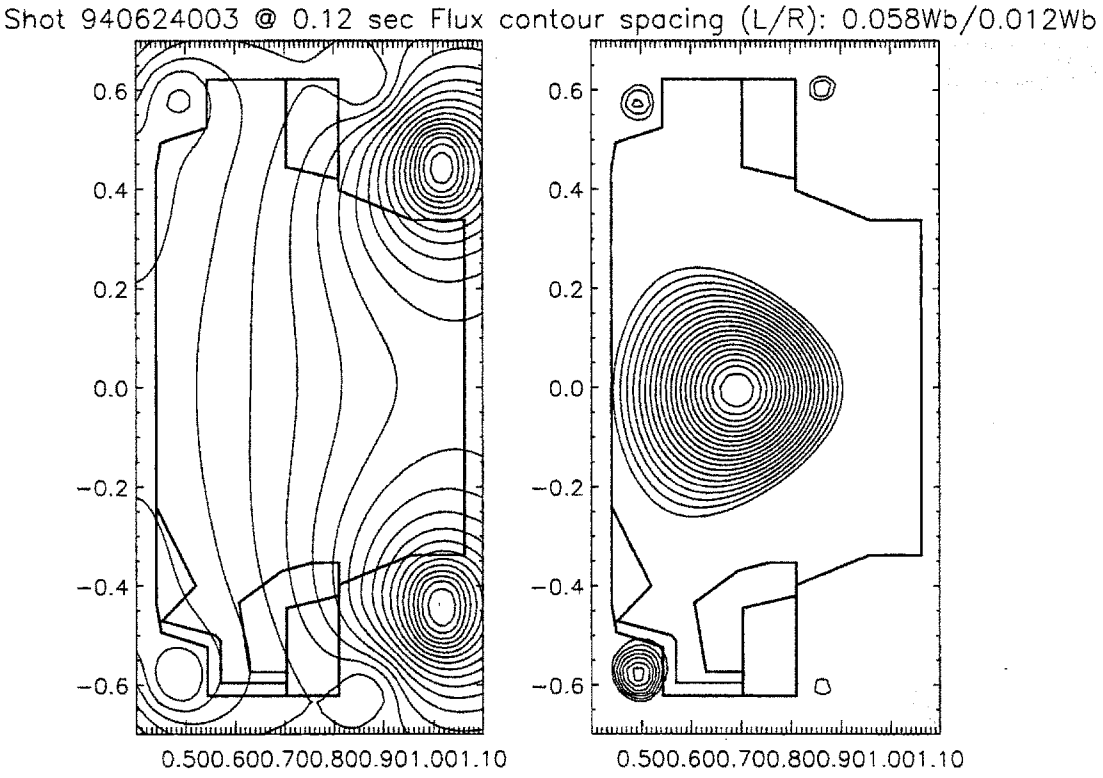

Figure 1-2: Poloidal flux contours without (left) and with (right) the plasma at a time early in the shot when the plasma is not strongly shaped yet. The right plot shows only flux surfaces inside the plasma.

special attention since they represent global motion of the plasma, usually toward the vacuum vessel wall. The most dangerous of these is the so–called vertical instability, which is an almost rigid vertical shift of the plasma and is always associated with strong shaping of the plasma. In order to create an elongated plasma, one has to use the poloidal field coils to pull the plasma from the top and bottom and push it from the sides. This is essentially a quadrapole field that has to be superimposed on the vertical field, which is necessary to balance the forces that push the plasma outwards in the radial direction [6]. These are: 1) the tire tube force due to the fact that the plasma pressure is constant on surfaces that have a smaller inboard area than outboard area and 2) the hoop force due to the fact that the force from both toroidal and poloidal magnetic pressure is larger on the inboard side. The externally applied poloidal field can then be concave towards the outboard side, whereas for a plasma of circular cross–section plasma it is approximately straight. This is shown in Figs. 1-2 and 1-3. Fig. 1-2 shows the magnetic field due to the coils and the structure alone at the beginning of a typical Alcator C–Mod discharge shot. This is the time right after breakdown and the plasma has not been shaped yet. It is still nearly circular and the vacuum field needed for equilibrium is purely vertical or concave towards the inboard side over a large region. Fig. 1-3 shows the magnetic field due to the coils and the structure alone at a time later in the shot, when the plasma has been given an elongated, triangular shape. Note how a larger part of the field lines are now convex towards the inboard side. Fig. 1-4 shows schematically how the vertical instability can arise. If the plasma current flows into the page, the equilibrium field has to be pointing downwards in order to create an inward force and balance the toroidal expansion forces. Imagine the plasma current being concentrated in one toroidal filament. At equilibrium, the filament sits on the midplane and sees no radial externally applied magnetic field. Now, if the field is convex towards the inboard side, and the filament moves off the midplane downwards, it sees an outward radial field, which creates a downward force, pulling the

filament even further away from equilibrium. In the absence of a conducting wall around the plasma, the timescale of this instability is of the order characteristic of most MHD phenomena, known as the Alfvén timescale. For a 1 keV ion temperature, and a 1 m length scale this timescale is in the μsec range. With a conducting wall around the plasma, the induced eddy currents provide damping and bring the instability timescale to the order of the skin penetration time of the conductor.

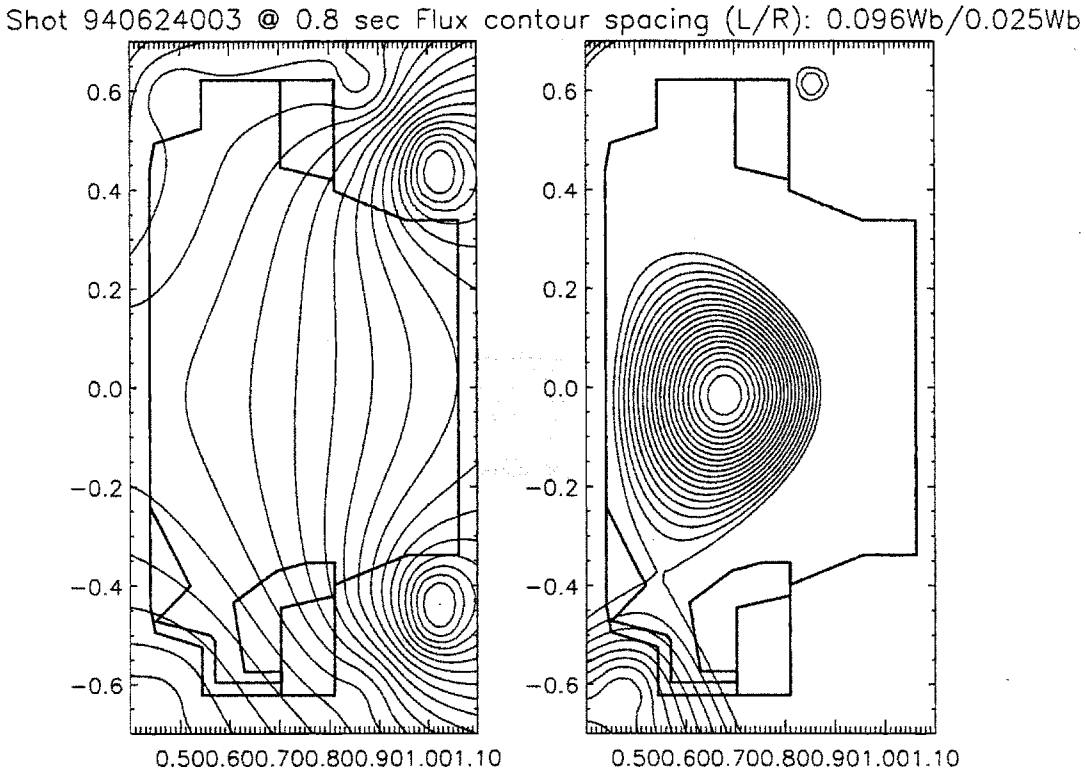

Figure 1-3: Poloidal flux contours without (left) and with (right) the plasma at a time later in the shot when the plasma is elongated. The right plot shows only flux surfaces inside the separatrix.

In the earlier tokamaks, where the duration of the plasma discharge was not considerably longer than the skin penetration time of the vacuum vessel, the vessel acted as a perfect conductor, stabilizing these modes, so that controlling them was not necessary. Modern tokamaks, though, have discharges with a duration tens or hundreds of times longer than the L/R time of the vacuum vessel. It is of utmost importance that the vertical instability is kept under control. When vertical control

is lost, the plasma moves up or down until it hits the vessel and is extinguished. This is known as a disruption. The eddy currents that are induced in the vessel during a disruption exert very large forces on the vessel, and for most high performance tokamaks these forces may threaten the mechanical integrity. In a reactor relevant tokamak like the proposed International Thermonuclear Experimental Reactor (ITER) [7], the plasma will have enough thermal energy to vaporize 40 kg of Beryllium, one of the plasma facing materials being considered. In case of such an accident, the reactor might have to be shut down for a long time to repair the first wall.

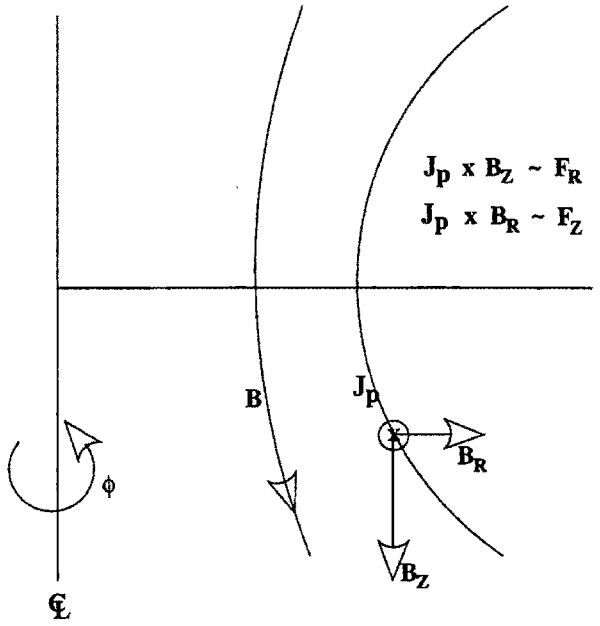

Figure 1-4: Interaction of a toroidal current with a curved equilibrium field.

1.2 Related Work

As mentioned earlier, there are several other tokamaks in operation in the world with shaped plasma cross–section and they all have to deal with the problem of the vertical instability. Consequently, a lot of work has been done so far in this field.

In the older configuration of JET, instability growth rates of 50–150 s^{-1} were observed [8]. A single–filament plasma representation was used together with two circuit equations, one for the vertical control coil pair and one for the vacuum vessel. By choosing appropriate values for the parameters of this model, the open loop growth rates were reproduced satisfactorily [9]. In voltage step tests, the oscillation frequencies and growth rates were predicted to within a factor of two [9, 10]. Nothing has been published yet on the new configuration. The modeling of the growth rates for the vertical instability is unresolved, in the sense that they do have large discrepancies between predicted and measured growth rates for divertor plasma configurations [11].

For DIII–D vertical stability analysis so far, the plasma has also been modeled as a single filament [12]. Its inductance is not allowed to vary with Z. The vacuum vessel is constrained to have one antisymmetric poloidal distribution of toroidal currents. Finite resistivity is allowed for the vacuum vessel and the control coil pair. The equation of motion for the massless single-filament plasma (which is equivalent to $B_R = 0$ at the filament location) together with the circuit equations for the vessel and the control coil pair give a third order system. From these equations, it becomes clear that, without feedback, the plasma becomes vertically unstable on an MHD timescale, when the decay index becomes smaller than a critical decay index defined by

$$n_c \equiv \frac{2R_0}{\mu_0 \Gamma L_v} \left(\frac{\partial M_{pv}}{\partial Z} \right)^2 \tag{1.7}$$

where M_{vp} is the mutual inductance between the plasma filament and the vacuum vessel, L_v is the self–inductance of the vessel, R_0 is the radial location of the plasma filament and

$$\Gamma \equiv \frac{L_{ext}}{\mu_0 R_0} + \frac{l_i}{2} + \beta_p + \frac{1}{2} \tag{1.8}$$

L_{ext} and l_i are the external inductance and internal inductivity of the plasma respectively. This model was used as guidance when exploring the stable operating space of feedback gains. In Ref. [13], this model was tested against experiments

where the plasma was moved up and down by means of steps in the voltage applied to the coil pair controlling the vertical position. The order of the response was confirmed, as was the maximum achievable decay index. The growth rates and oscillation frequencies of the modes of response, however, could only be predicted to within a factor of two of the observed ones, if one unjustifiably adjusted the vessel resistance by 50% and multiplied the actual feedback gains used by a factor of four. No experiments were conducted, in which feedback control was turned off, while the plasma was unstable. This experiment can result in a disruption, so that a large number of them can be damaging to the tokamak. This is why it is usually avoided. It is, however, the only direct way to compare open loop plasma behavior to theory. Perturbed equilibrium modeling of the plasma has also been done [14], but has not been experimentally validated yet.

ASDEX-U differs from other machines in the method used to interpret the magnetic measurements in order to infer the state of the plasma. A large number of MHD equilibria have been computed and the values of all the measurements used by the control system as well as the basic equilibrium parameters that are being fed back on have been stored in a database [16]. Using function parametrization [17], a quadratic relationship between equilibrium parameters and measurements was developed. A simple filament model of the plasma, together with 6 modes for the vacuum vessel were used to produce rough estimates for feedback gains. The Tokamak Simulation Code (TSC) [18] was then used in place of the tokamak to test the control loop in pseudo–real time [19, 20]. TSC calculates the time evolution of a free–boundary plasma equilibrium, which is consistent with a prescribed sequence of currents in the poloidal field coils and the passive conductors. A better set of feedback gains is developed this way, which is ultimately tested on the tokamak itself. Substantial work has been done on electromagnetic modeling of the passive conductors in ASDEX–U [21, 22]. For no–plasma runs, the passive stabilizer loop current was predicted via 2–D eddy current modeling to within a 30% accuracy,

while in plasma runs, 2–D eddy current modeling with a filament model of the plasma reproduced flux loop measurements to within a 20–50% accuracy.

As in ASDEX–U, in TCV control laws are being tested using TSC [23, 24]. The NOVA–W code [25] is also used to assess the effect of plasma deformability on closed loop axisymmetric response. NOVA–W is a linear MHD stability code which takes the effects of resistive conductors in the vacuum region into account. The passive eigenmode always rearranges itself under active feedback so that the flux measurements used in the feedback loop are minimized [26], thereby minimizing the effect of the feedback system. NOVA–W was used to determine which measurements and which actuators (PF coils) to weigh more heavily for more effective control. A similar approach is also used in PBX–M [27].

In JT60–U a rigid multifilament model of the plasma was used together with a vacuum vessel modeled as a set of 100 toroidal conductors [29]. In experiments where feedback was turned off during vertically stable discharges, the theory predicted the Z-evolution very well. In closed loop experiments where the plasma was perturbed by means of neutral beam injection, the growth rate was predicted accurately, and the oscillation frequency to within a factor of three.

A survey of related work performed so far shows that several sophisticated models exist for the axisymmetric motion of a plasma in the presence of resistive conductors. These models are used in a trial–and–error mode as an aid to finding good feedback laws. However, these models have not been used substantially in the context of linear control theory, to derive control laws, or predict experimental behavior. Only very simple models have actually been used for this purpose. Comparison of theory to experiment is rarely published.

1.3 Alcator C–Mod

Alcator C–Mod is the third in a series of compact, high–field tokamaks built at M.I.T. and aimed at achieving high performance at low cost. Unlike its predecessors, it has an elongated vacuum vessel, and the poloidal field (PF) coils are located inside of the toroidal field (TF) coils. In addition, it features ten independent power supplies feeding a set of 13 PF and ohmic heating (OH) coils. It has, therefore, the capability of producing a large variety of shaped plasmas, and divertor configurations. Fig. 1-5 shows a cross–sectional view of Alcator C–Mod. It can have a

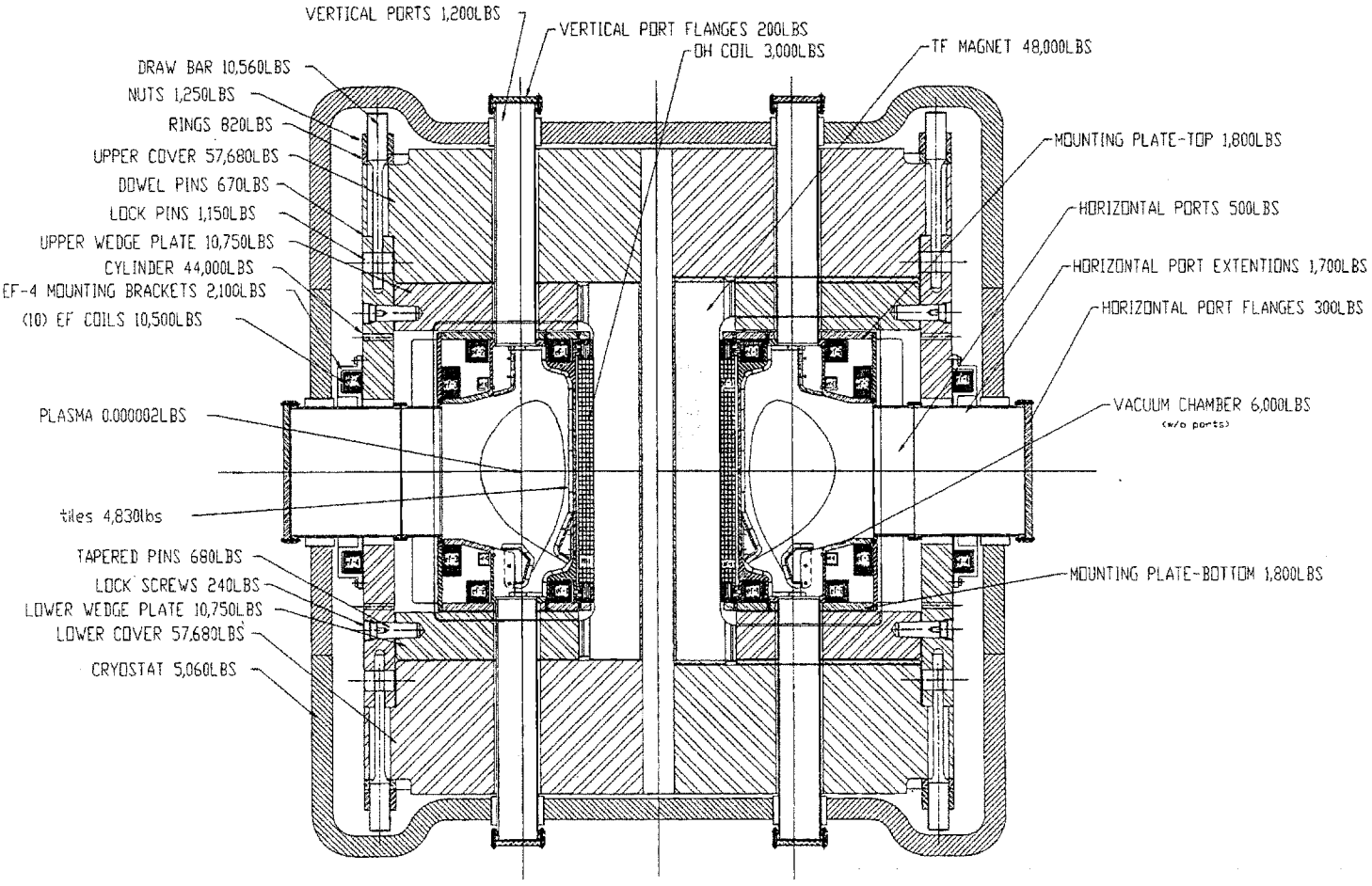

Figure 1-5: Cross–section of Alcator C–Mod

maximum toroidal field at the center of the vacuum vessel of 9 T and a maximum

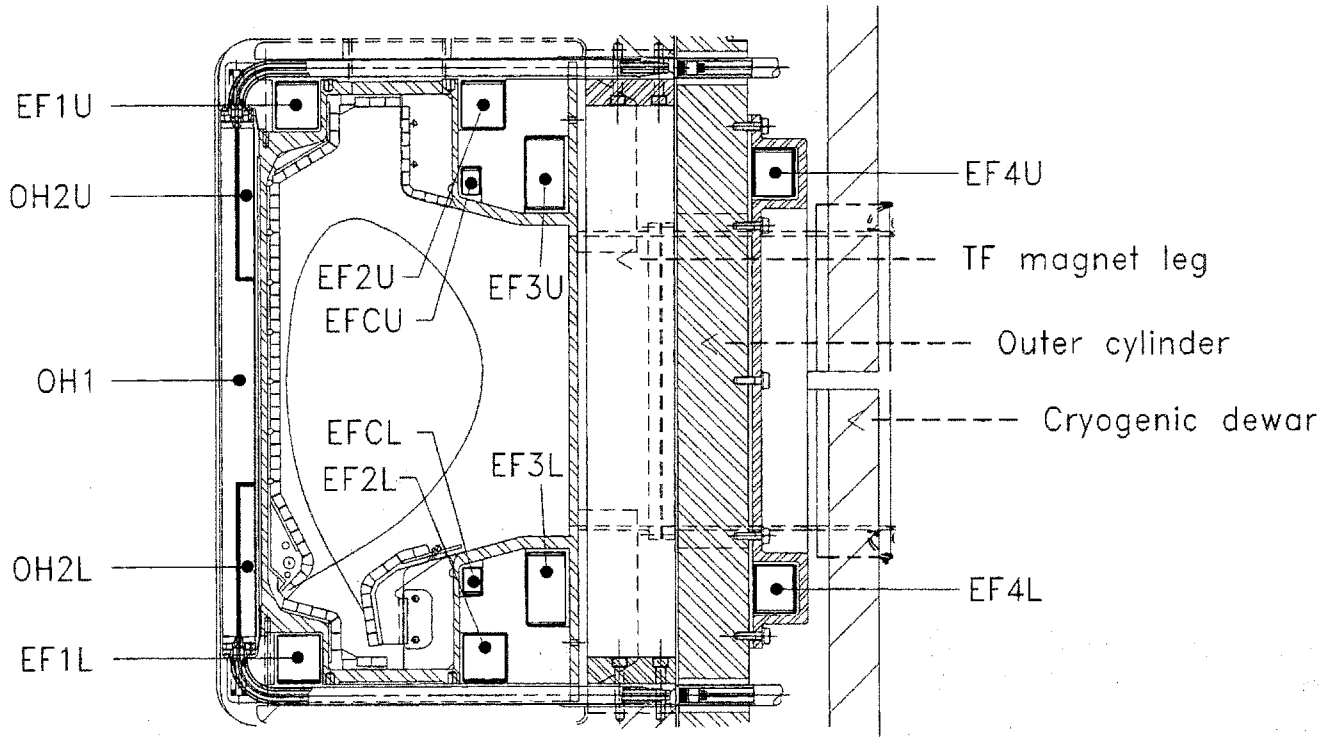

Figure 1-6: Cross–section of the vacuum vessel showing the OH and PF coils.

toroidal current of 3 MA. All magnets are made of copper and cooled with liquid nitrogen. Fig. 1-6 shows a closer view of the coils. Power is supplied by an alternator, connected to a flywheel capable of storing 2000 MJ of energy.

The main function of the OH1 coil is to control the toroidal loop voltage (and hence the total plasma current) by varying the time derivative of the poloidal flux. The difference between OH2U and OH2L currents controls the Z–position of the plasma on a slow timescale, while the EFC coils, which are connected in antiseries, control the Z–position on a faster timescale. The OH2 coils are fed by two powerful but slow power supplies, while the EFC coils are fed by a smaller but faster power supply. The R–position of the plasma is mainly controlled by the EF3 coils connected in series, which are fed by one power supply. Alcator C–Mod is mostly run in a so–called diverted, single–null configuration. This means that the last closed surface of constant poloidal flux (separatrix) does not touch the vacuum

vessel wall (see Fig. 1-3) and that the two points of zero poloidal field that form outside the last closed flux surface (x–points) are not symmetric; one of them is further away from the plasma than the other, so that most of the particles escaping the plasma by means of perpendicular (to the field lines) transport, end up through parallel transport at one end of the vacuum vessel. The Z–position of the x–points is mainly controlled by the EF1 coils. The EF2 coils control the x–point R–position. The sum of the OH2 coil currents together with the EF4 coils, which are connected in series, control the elongation and triangularity of the plasma by pushing on it from the outside and pulling on it from the inside.

The control of individual plasma shape and position parameters is actually much more coupled than this simplistic one-to-one identification of coil functions, however, and necessitates the use of a very flexible control system. Fig. 1-7 shows a block diagram of the hybrid digital/analog plasma control computer system used in Alcator C–Mod. It can take up to 96 signals as input. The interpretation of the state of the plasma is done by multiplying these signals by a predictor ($\mathbf{A}_p$–matrix) to form up to 16 different linear combinations representing the parameters to be controlled. These signals are then compared to their pre–programmed values and the error, its integral and derivative are then multiplied by some gains. The resulting 16 signals are then multiplied by the controller (**M**–matrix) which determines what coils are to be involved in controlling each parameter. The pre–programmed voltage demand signals determine the general scenario of the discharge. They are added to the output of the controller and the sum goes to the power supplies as voltage demand. All matrix multiplications are performed in an analog way, but the matrices are inserted digitally and can be changed during the discharge.

The inputs to the plasma control computer are mainly magnetic diagnostic measurements of two types: poloidal magnetic flux and poloidal magnetic field on the inside surface of the vacuum vessel. The poloidal flux is measured by the so–called flux loops. These are wires running toroidally along the vacuum vessel wall.

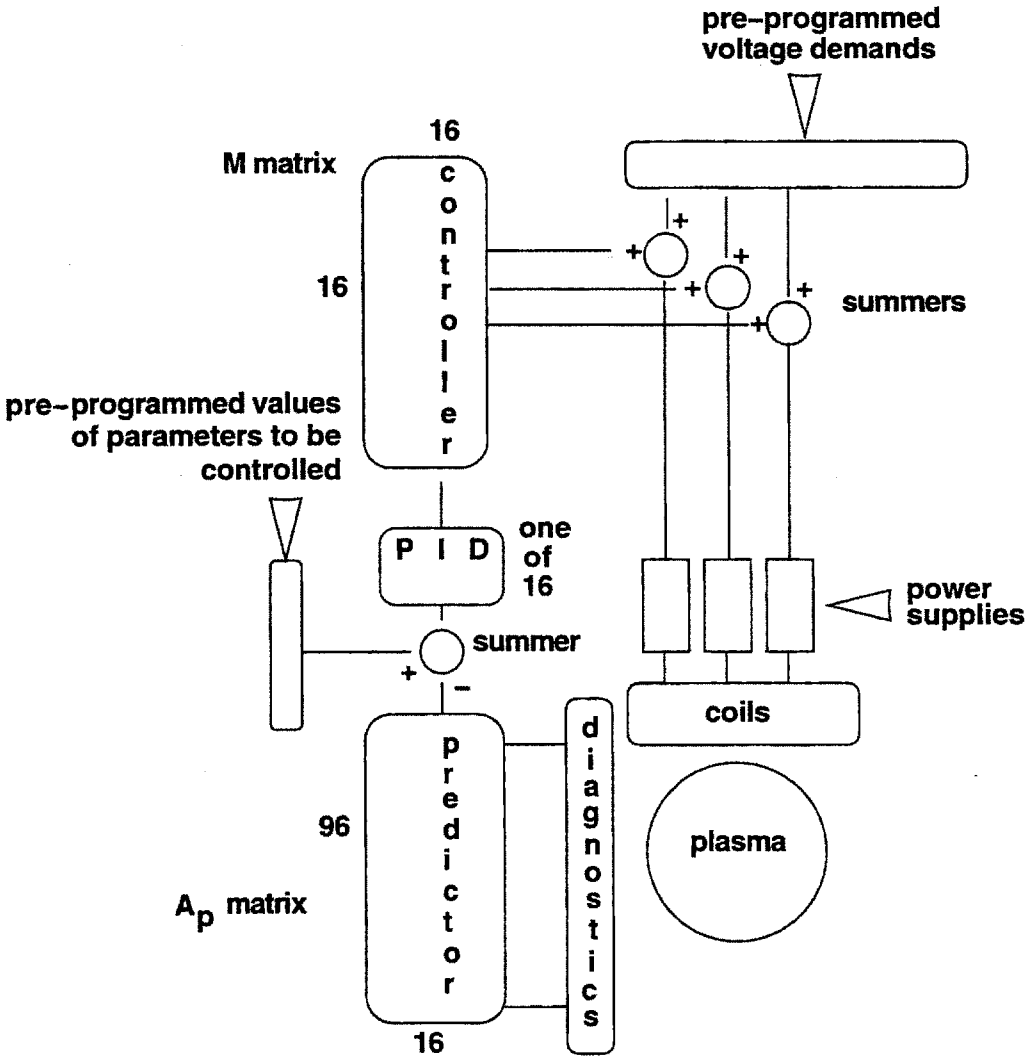

Figure 1-7: Block diagram of the hybrid feedback computer.

The principle of operation in demonstrated in Fig. 1-8. The area A is large and the

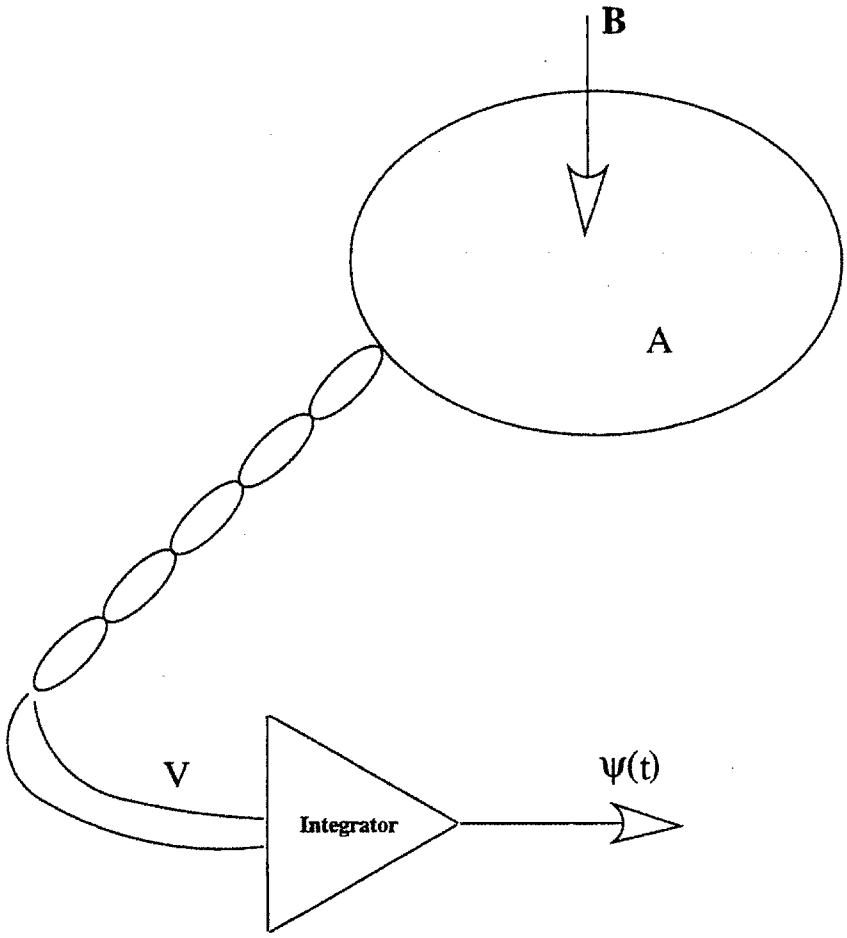

Figure 1-8: Illustration of the principle of operation of the flux loops.

magnetic field $\vec{B}$ going through it is in general toroidally nonuniform. The output V is then

$$V = -\frac{d\psi}{dt} = -\frac{d}{dt}\int_A \vec{B}\cdot d\vec{s} \tag{1.9}$$

This is a toroidally averaged measurement, except for some loops that do not go all the way around toroidally, but are located on the vacuum vessel wall between two ports (partial flux loops). The poloidal magnetic field is measured by the B_p–coils. These are small pick-up loops located at different poloidal locations, oriented so that no toroidal field flows through them. They operate on the same principle as the flux loop, the difference being that the area A is small enough that the magnetic field $\vec{B}$

going through it can be considered uniform. The output V then is proportional to $\frac{d\vec{B}}{dt}$. This is therefore a localized measurement. There are 21 full flux loops, 6 partial flux loops and four sets of 26 B_p–coils located at four different toroidal locations.

The vacuum vessel, which has some sections as thick as 2 cm, serves also as structural support for the PF coils and the first wall hardware. A large amount of stainless steel serves as structural support for the TF coils. Both the vacuum vessel and the structure are toroidally continuous for the most part and can carry large eddy currents; this is desirable for passive control, because it helps slow down any unstable axisymmetric plasma behavior. However, it also means that active control is slower, since any change in the coil currents (which are outside the vacuum vessel) creates eddy currents in the vacuum vessel and can only create a change in flux inside the vacuum vessel after the eddy currents have died away. The first wall consists of molybdenum tiles, and the bottom of the vacuum vessel is fitted with a closed, baffled divertor chamber.

Auxiliary plasma heating is provided by two transmitters supplying a total of 4 MW of ion cyclotron radio frequency waves. Because of its high particle–, power–, and current– densities, Alcator C–Mod is expected to have edge plasma conditions that resemble those expected in ITER, and is therefore going to offer valuable information for the design of the ITER–divertor.

1.4 Motivation and Outline

From the above it is clear that vertical position control is essential for shaped tokamaks. So far, tokamaks have been controlled by simple proportional, integral and derivative feedback control that assumes that control of different plasma parameters is completely uncoupled; in other words each coil set affects only one of the parameters to be controlled. The advantage of this approach is that no model is

needed for the response of the unstable system we are trying to control. Instead, the "optimal" feedback gains are determined by trial and error from shot to shot. If the no–coupling assumption is not true, however, the control of two different plasma parameters will often cause two coil sets to fight each other, resulting in a non–optimal use of resources (voltage sources for the coils). This is due to the fact that changing one parameter may result in an undesirable change in another parameter. Modern control theory has many interesting methods to offer for good control of many–input many–output (MIMO) systems. When the control system of the tokamak is frequency independent (as is the case in Alcator C–Mod), optimal control theory can be used to make the most efficient use of the resources for the smallest possible deviation of certain plasma parameters from their desired values. With a frequency dependent controller, more sophisticated methods can be used to reduce the effect of noise (H_∞–theory) and structured uncertainties in the form of modeling errors and perturbations (μ–synthesis theory). In both cases, however, a good linear model of system response is needed. During a typical shot the plasma goes through many different shapes and one cannot expect a single linear model to be valid for all cases. Control laws based on different models can be used during different phases of the plasma discharge. Most modern control systems (including the Alcator C–Mod control computer) have this capability which is known as "gain scheduling".

The purpose of this thesis is to examine the usefulness of linear axisymmetric plasma response models in predicting the behavior of Alcator C–Mod geometric shaping parameters and developing feedback laws to control them. In particular, it attempts to go one step beyond what has already been done in that it uses a more sophisticated plasma response model for this purpose than the single–filament or multifilament models that have been compared to experiment to a limited extent so far. The approach is to first create models for all the individual systems shown in Fig. 1-7, test them individually, then put them all together in a closed loop, and test

the closed–loop. Testing of individual systems in an open–loop configuration was very satisfactory, proving that the perturbed equilibrium plasma response model and a toroidally symmetric electromagnetic model of the vacuum vessel and the structure can be trusted for the purpose of calculations for control law design. Closing the loop introduced some serious nonlinearities making comparison of linear theory to experiment unsatisfactory. When these nonlinearities are added to the linear models, however, the experimentally observed behavior can be predicted by theory satisfactorily.

Chapter 2 will present two plasma response models. The first is the rigid multifilament model where the plasma is modeled as a set of toroidal filaments that do not move with respect to each other and whose current does not change. The second is the perturbed equilibrium model, namely a model that assumes that the plasma is always in a self consistent MHD equilibrium in the vicinity of some central equilibrium and that the time response is dictated by the L/R time of the conductors around it. Both of these models neglect plasma inertia. Chapter 3 presents an electromagnetic model of the vacuum vessel and the structure of Alcator C–Mod and how this model agrees with experimental measurements. This model is useful in plasma equilibrium reconstruction and was of some help in developing a repeatable plasma startup procedure. Models have also been developed for the power supplies that feed the equilibrium field coils and the results are also presented in Chapter 3. Chapter 4 develops a dependable way of reducing the order of the resulting models so they can be used for repeated time consuming control calculations. Chapter 5 presents a comparison of theory to experiment for elongated plasma discharges where the feedback control was turned off and the plasma moved exponentially towards the vessel wall. Chapter 6 presents a comparison of theory to experiment for elongated plasma discharges with the feedback loop closed. Finally, Chapter 7 presents a summary and conclusions that can be derived from the comparison of theory to experiment and suggestions for further work.

Chapter 2

Linear Plasma Response Models

2.1 General Assumptions

In order to exploit the many recent achievements of MIMO linear state space control theory, we have to have a linearized model for the response of the system consisting of the plasma and the conductors around it. To arrive at such a model several assumptions must be made. If the only tools we have to control the plasma are the OH and PF coils, we can only affect toroidally symmetric modes of the plasma, so we are justified in confining ourselves to considering axisymmetric behavior. If we suppose that the response of the plasma is governed by the ideal MHD momentum equation (Eq. 1.2), two timescales are of interest: the Alfvén timescale of the plasma and the L/R timescale of the conductors around it. If the first is much shorter than the second (and usually it is by about 3 orders of magnitude), we are justified in neglecting the inertia term in the momentum equation. The presence of the conductors slows down any instability from the Alfvén timescale to the L/R timescale. If the plasma were surrounded by a perfectly conducting vacuum vessel, it would be stable. We are also justified in neglecting plasma inertia effects for a practical reason: the fastest Alcator C–Mod power supply cannot react faster than a timescale of

approximately 1–msec, so that if the plasma were unstable on the Alfvén timescale, we would not be able to control it anyway. Then, the plasma is supposed to be in equilibrium at each time and the conductors determine how it moves from one equilibrium to the next. This is known as the quasistatic approximation.

A set of toroidal conductors is governed by circuit equations which describe the evolution of the poloidal flux at the locations of the conductors:

$$\mathbf{M}\dot{\vec{I}} + \mathbf{R}\vec{I} = \vec{V} \tag{2.1}$$

where $\mathbf{M}$ is the inductance matrix (including mutual and self inductances), $\mathbf{R}$ is the diagonal resistance matrix for the conductors, and $\vec{V}$ is the vector of voltages applied to the conductors; its only non–zero elements are the ones corresponding to the active conductors. The word "active" here refers to a conductor that is being fed by a voltage source (power supply) as are the coils. $\vec{I}$ is a vector containing the currents flowing in the conductors. We can choose the state of the plasma at each point in time to be described by the poloidal flux it creates at the conductor locations. Then, including a linearized plasma response would amount to adding to $\mathbf{M}$ some matrix $\mathbf{X}$ accounting for the coupling between conductors mediated by the plasma [32]:

$$\mathbf{M}\dot{\vec{I}} + \mathbf{X}\dot{\vec{I}} + \mathbf{R}\vec{I} = \vec{V} \tag{2.2}$$

Here, $\mathbf{X} \equiv \frac{d\vec{\psi}_p}{d\vec{I}}$, and $\vec{\psi}_p$ is the poloidal flux at the conductor locations due to plasma current alone. $\vec{I}$ is then the state vector of the plasma/conductor system.

Several linear models for the plasma have been devised, some of which will be discussed in the following sections. All these models amount to finding the matrix $\mathbf{X}$. The simplest one is to replace the plasma by a single toroidal filament [12]. The next step is to use several toroidal filaments for the plasma in order to simulate a distribution of toroidal current in the plasma [30]. One can also determine the linearized plasma response by perturbing the conductor currents that give a certain base equilibrium of interest and considering the plasma to be always

in an equilibrium which is a linear combination of the set of perturbed equilibria. This approach was introduced in Ref. [31] and was extended in Ref. [32] to include passive conductor response and approximate flux conservation. A more rigorous approach based on the energy principle (but still neglecting plasma inertia) is used in Ref. [33].

The aim of this thesis is not to evaluate these plasma models or to suggest a new one, but rather to make contact between these models and the observed behavior in the Alcator C–Mod tokamak. Only when we feel confident, that we can explain the experimental observations with some linear model, can we go ahead and make use of the wealth of existing modern control theory techniques.

2.2 The Rigid Filament Model

Representing the plasma as a single toroidal filament placed at the position of the plasma current centroid ([12, 34]) is the simplest approach to the problem of vertical stability. Fig. 2-1 shows a comparison of the poloidal flux at the locations of some magnetic diagnostics (flux loops) due to the plasma alone for an elongated Alcator C–Mod plasma and due to a filament carrying a current equal to the total plasma current and placed at the plasma current centroid location. The flux pattern at the vacuum vessel, where all the magnetic diagnostics are located, is similar in both cases. It has been argued ([12]), therefore, that the single filament model of the plasma is a satisfactory descriptor as far as the control problem is concerned. The distribution of the plasma current, has to have some effect on plasma response, however, for two reasons: first, when some of the plasma current is placed closer to the vacuum vessel, more eddy currents will be induced when the "plasma" moves than when all of the current is placed in the middle of the vacuum vessel; second, as some current is spread over areas of different external field curvature than that of the current centroid location, its stability characteristics have to change. If the

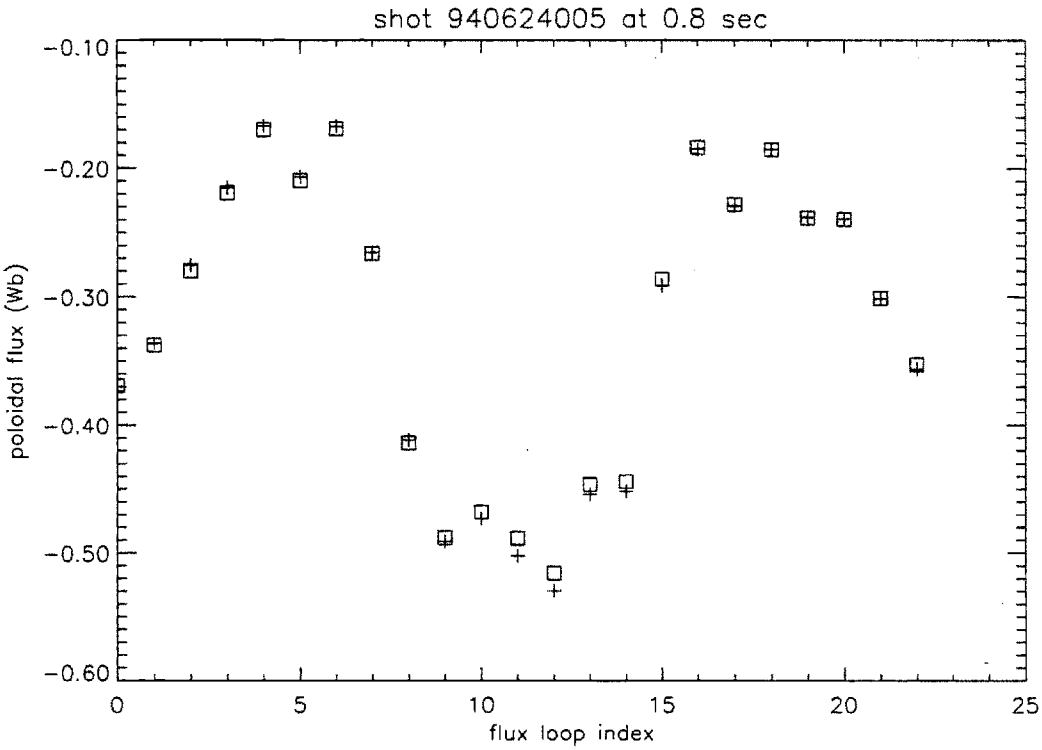

Figure 2-1: Flux at different flux loops due to the plasma alone (squares) and due to a filament carrying a current equal to the total plasma current and placed at the plasma current centroid location (crosses) for an elongated Alcator C–Mod shot.

plasma response is affected, the control problem will be affected as well.

If we know the plasma current distribution, the next logical step is to represent the plasma as a set of toroidal current carrying filaments with a current distribution resembling that of the plasma. We can assume that the filaments do not move with respect to each other and restrict motion to the vertical direction only. This is done in Ref. [30]. These are of course nonphysical restrictions, since there can be other non–rigid and not exactly vertical modes which require less energy and are, therefore, more unstable. It is not clear how one should go about specifying these modes without going into a full MHD analysis, however. The rigid vertical motion is a good approximation at least for the qualitative analysis of elongated plasma response. The circuit equations for the conductors around the filaments become:

$$\mathbf{M}\dot{\vec{I}} + \mathbf{R}\vec{I} + \sum_{i}^{N} I_{pi}\frac{\partial \vec{M}_{pi}}{\partial z}\dot{z} + \sum_{i}^{N} \dot{I}_{pi}\vec{M}_{pi} = \vec{V} \tag{2.3}$$

where:

$\vec{M}_{pi}$ is a vector containing the mutual inductances from the ith plasma filament to all the conductors,

I_{pi} is the current in the ith plasma filament,

z is the change in vertical position of the plasma filaments and

N is the number of plasma filaments.

One has to specify how the plasma filament currents change. One possible assumption is that the I_{pi}'s change so as to conserve the poloidal flux. This is a valid assumption for an ideal (non–resistive) plasma. Another possible assumption is to assume that the plasma filament currents do not change, conserving plasma current density. This second assumption is of course easier to implement, since the $\dot{I}_{pi}$–term vanishes in Eq. 2.3. Furthermore, it has been shown [35], that a rigid constant current shift is never more stable or further from the exact energy minimizing MHD eigenmode than a rigid constant toroidal flux shift. It makes

sense, therefore, to use the constant plasma current assumption.

To determine z, we need the equation of motion of the plasma. There are two forces acting on the plasma:

• The force due to the eddy currents induced in the conductors around the plasma:

$$F_z^{eddy} = -\frac{dE_{mag}}{dz} \tag{2.4}$$

where E_{mag} is the magnetic energy stored in the conductor and filament system and $\hat{e}_z$ is the unit vector in the vertical direction:

$$E_{mag} \equiv \sum_j^M \frac{1}{2} \mathrm{M}_{jj} I_j^2 + \sum_j^M \sum_i^N I_{pi} M_{pij} I_j \tag{2.5}$$

where M_{pij} is the j'th element of vector $\vec{M}_{pi}$ from Eq. 2.3.

$$F_z^{eddy} = \sum_j^M \sum_i^N I_{pi} \frac{\partial M_{pij}}{\partial z} I_j \equiv \sum_j^M S_j I_j = \vec{S}^T \vec{I} \tag{2.6}$$

where M is the number of conductors around the plasma and the superscript T stands for transpose.

• The Lorentz force due to the interaction of the plasma filament currents with the radial magnetic field encountered as the plasma moves a distance z from its equilibrium position:

$$F_z^{Lorentz} = -\sum_i^N 2\pi I_{pi} \frac{\partial B_{Ri}}{\partial z} z \equiv S_L z \tag{2.7}$$

B_{Ri} is the radial field at the location of filament i.

We have then:

$$m\frac{d^2 z}{dt^2} = F_z^{eddy} + F_z^{Lorentz} \tag{2.8}$$

where m is the plasma mass. In the quasistatic approximation, the left hand side of Eq. 2.8 is negligible and one can simply solve for z and substitute into Eq. 2.3. z is the position where the Lorentz force balances the force due to the eddy currents.

Then, in the sense of Eq. 2.2, the mutual inductance matrix of the conductors due to their coupling to the plasma is:

$$\mathbf{X} = -\frac{1}{S_L}\left(\sum_i^N I_{pi}\frac{\partial \vec{M}_{pi}}{\partial z}\right)\vec{S}^T \tag{2.9}$$

Eqs. 2.2 and 2.9 describe the response of a massless filament plasma in the presence of passive conductors and active coils. Performing eigenmode analysis on Eq. 2.2 usually gives one unstable mode for elongated plasmas, which is the vertical mode.

The plasma current distribution may be obtained either from an MHD equilibrium code, if we are interested in the response of a theoretical plasma equilibrium, or can be reconstructed from data from a real plasma discharge at a particular time. In the second case, an MHD equilibrium code has to be run anyway in order to look at other equilibrium quantities for other purposes. In either case, the spatial grid used by the equilibrium code can be used as locations of the plasma filaments. All results presented in Chapter 5 are calculated using a set of 65×65 filaments coinciding with the grid of an equilibrium code. This is purely a choice of convenience. The computational cost of using so many filaments was small, and any operation attempting to lump plasma current on that grid into a smaller number of filaments would probably have had some computational cost as well. Of course, such a large number of filaments is not necessary to reproduce current distribution effects. A study was done in Ref. [30] to determine how the number of filaments affects the growth rate of the vertical mode. It was found that the growth rate varied considerably with fewer than ten filaments, but converged to some value when ten or more filaments were used.

2.3 The Perturbed Equilibrium Model

The perturbed equilibrium model is described in Ref. [32]. In this section, an overview of the model is given. First we look at the current conserving perturbed

equilibrium model of the plasma response in the presence of the OH and PF coils alone neglecting the vacuum vessel and passive structure. Then we look at how we can incorporate our electromagnetic model of the vacuum vessel and passive structure, without introducing any additional computational work. Lastly, a method is described for allowing the plasma current to vary so that magnetic flux is approximately conserved.

2.3.1 General Formulation

In order to write down a linear response model, one first has to define an equilibrium condition or operating point. This requires specifying certain parameters (inputs). Once the operating point has been defined, some other quantities we may be interested in are also defined (outputs). The linear model then is supposed to predict how the outputs vary when the inputs are perturbed slightly.

In a linear plasma response model one has to define a plasma equilibrium as the "operating point" which involves solving the Grad–Shafranov equation. The Grad–Shafranov equation (Eq. 1.5) is a second-order, nonlinear partial differential equation. In order to solve it, two things are needed: a) $p(\psi)$ and $F(\psi)$ have to be specified in the inhomogeneous part (the right hand side) and b) boundary conditions have to be specified. There are two approaches commonly used to indirectly define boundary conditions in computer codes that solve the Grad–Shafranov equation. In the free-boundary approach all toroidal currents flowing outside the plasma are specified. The shape of the plasma is then an output of the code. In the fixed–boundary approach, some plasma shape parameters are specified. The currents in the coils are then an output of the code.

When one of the inputs of the equilibrium code is perturbed, the outputs are perturbed as well. We can run the equilibrium code with each of the inputs perturbed one at a time to obtain a matrix, $\left(\frac{\partial \mathbf{outputs}}{\partial \mathbf{inputs}}\right)$, which describes how the

outputs change with the inputs in a static sense. For timescales that are slow compared to the timescales of the momentum equation (Eq. 1.2), this is a good description of plasma evolution. In other words, if we assume that:
– the only unstable (vertical) eigenmode will have a growth rate comparable to the L/R time of the conductors around the plasma, which is determined primarily by the damping effect of these conductors, and that
– Eq. 1.2 has no other unstable eigenmodes,
then static transition from one equilibrium to another as described by $\left(\frac{\partial \mathbf{outputs}}{\partial \mathbf{inputs}}\right)$ is valid. The time evolution from one equilibrium to the other will be determined by its coupling to the conductors as described in Eq. 2.2. If we use the currents in the conductors, $\vec{I}$, as the inputs and the poloidal flux due to the plasma current alone at the conductor locations, $\vec{\psi}_p$, as the outputs of the plasma equilibrium code, the coupling of the conductors due to the plasma becomes:

$$\mathbf{X} = \left.\frac{d\vec{\psi}_p}{d\vec{I}}\right|_{J(\psi)} \tag{2.10}$$

where the subscript $J(\psi)$ denotes that the plasma current distribution remains constant. This assumption of current conserving plasma response is not correct physically. It contradicts the ideal MHD assumption that the plasma has no electrical resistivity. An approach for approximate flux conservation instead is discussed in Section 2.3.3.

The free–boundary equilibrium code ASEQ (ASymmetric EQuilibrium) [40] was used to implement the above perturbational equilibrium method in this work. This is an up–down asymmetric variation of the plasma equilibrium solver of the PEST (Princeton Equilibrium, Stability, and Transport) code [39]. As a free–boundary solver, it takes as inputs the coil currents and some parametrization of the pressure and F profiles. The so–called Strickler profile shape function is used in this study. Defining the normalized flux, $\tilde{\psi}$ as:

$$\tilde{\psi} \equiv \frac{\psi - \psi_{axis}}{\psi_{edge} - \psi_{axis}}, \tag{2.11}$$

the profiles are parametrized as:

$$\frac{dp}{d\psi} \propto \frac{e^{-\alpha_p \tilde{\psi}} - e^{-\alpha_p}}{e^{-\alpha_p} - 1} \tag{2.12}$$

and

$$F\frac{dF}{d\psi} \propto \frac{e^{-\alpha_f \tilde{\psi}} - e^{-\alpha_f}}{e^{-\alpha_f} - 1} \tag{2.13}$$

The proportionality constant in Eq. 2.12 involves the total plasma current I_p. The parameters α_p and α_f control the peakedness of the profiles.

One technical point should be made here: elongated plasmas are inherently unstable, so that the equilibrium code has problems converging, unless one of the coil currents is allowed to float so that some other condition is satisfied. In this study the vertical (Z) location of the magnetic axis was specified as input while the EFC coil currents were allowed to vary. When each of the OH and PF coil currents is perturbed, one has to also keep track of the change in the EFC coil currents which is an output of the equilibrium solver. In this way we obtain a set of perturbed equilibria with the same Z–position of the magnetic axis. The degrees of freedom associated with moving the plasma up and down are then accounted for by running two more perturbed equilibria in which the requested Z–position is perturbed (up and down) and the EFC coil currents are allowed to float, while all other OH and PF coil currents are fixed at the values they have in the base equilibrium.

The free–boundary equilibrium solver has the disadvantage that one does not know in advance what the plasma is going to look like, or even if there exists a solution to the Grad–Shafranov equation with the prescribed inputs. If the inputs for the perturbed equilibrium are not very different from the inputs to the base equilibrium, however, there should be a solution. The advantage of the free–boundary approach is that it deals in coil currents; this not only makes simpler to use with the circuit equation, but it also is a good representation of the degrees of freedom of the system we are trying to control, since the coil currents are the only thing we can change for control. The fixed–boundary approach offers the advantage that

the plasma shape is known in advance, but the coil current combination giving the requested plasma shape is not unique, so that some further assumption has to be made concerning coil currents. Furthermore, the choice of shape parameters that are used as inputs, may not describe all the degrees of freedom adequately, so that special care must taken in the selection of the inputs.

2.3.2 Incorporating the Passive Conductors

In the previous section no account is taken in $\vec{I}$ (Eqs. 2.1 and 2.2) of the passive conductors (vacuum vessel and structure). This procedure had already been described in Ref. [31]. One of the things that Ref. [32] added is the effect of the passive conductors. Theoretically, one could add the currents in the passive conductors as inputs to the equilibrium solver and then perturb their currents one by one to create a full set of perturbed equilibria including the passive conductor currents. This would increase the computational cost of the perturbed equilibrium procedure dramatically, however.

As mentioned in Chapter 1, there are 13 active coils in Alcator C–Mod. The vacuum vessel and passive structure have a complicated shape and have been modeled (as we shall in Chapter 3) by a set of 190 toroidal conductors. Admittedly, the passive conductor system cannot have 190 modes all of which are distinctly different and affect the plasma and magnetic diagnostics equally. We shall see in Chapter 4 that one cannot reduce the passive conductor system to a size of less than 30 without losing some modes important for control. As a result, the number of times one would have to run the equilibrium solver increases from 13 to at least 43.

Ref. [32] proposed a way to avoid having to include the passive conductors in the inputs of the equilibrium solver. It rests on the assumption that the number of modes of plasma motion that affect the conductors around it is smaller than the

number of active coils. It is hard to imagine that the plasma can move in such a way as to excite modes of complicated structure in the passive conductors, i.e., modes where adjacent elements have currents of opposite signs. To see this, one has to look at the matrix $\mathbf{\Delta}\psi_{\mathbf{g(p)}}$, the change in flux due to the plasma at the passive conductor locations for the set of perturbed equilibria. For the 190–element conductor model and a set of 13 perturbed equilibria this 190 $\times$ 13 matrix is a mapping of plasma modes to modes of the conductor system. If this matrix is of rank less than 13, then the number of passive conductor modes that can be excited by plasma motion is equal to the rank, i.e., the spectrum of excitable modes is covered by the information contained in the 13 perturbed equilibria. Fig. 2-2 shows the normalized singular

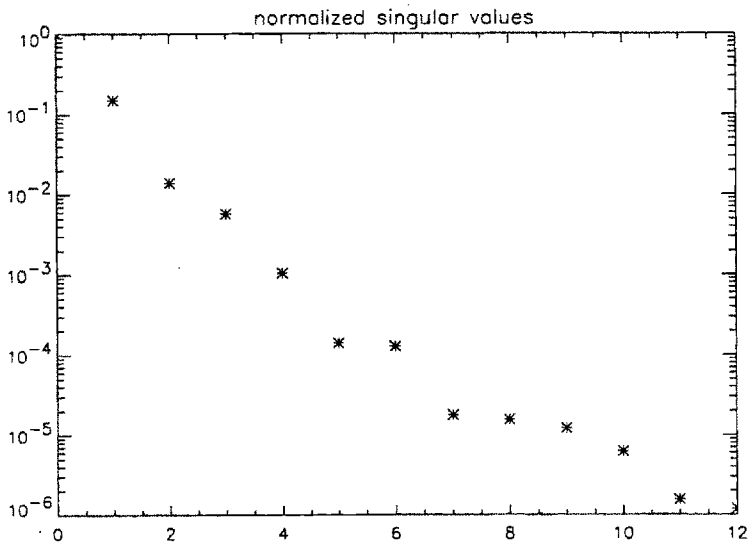

Figure 2-2: Singular values of the matrix $\mathbf{\Delta}\psi_{\mathbf{g(p)}}$ normalized to the maximum one for an elongated Alcator C–Mod shot. Indices go from 0 to 12.

values of $\mathbf{\Delta}\psi_{\mathbf{g(p)}}$ for an elongated plasma equilibrium from one of the Alcator C–Mod discharges used in Chapter 6. We see that the eighth largest singular value is smaller than the largest singular value by five orders of magnitude. Therefore, approximately seven modes should be enough to describe the effect of the plasma on the passive conductors.

One can then represent a set of passive conductor currents by an equivalent set of coil currents that produce the same flux at some set of reference points inside the vacuum vessel. If the mutual inductance between these points and the coils is $\mathbf{M}_{\epsilon c}$, and the mutual inductance between these points and the passive conductors is $\mathbf{M}_{\epsilon g}$, then the flux at the reference points due to a set of coil currents $\vec{I}_c$ is given by:

$$\vec{\psi}_{\epsilon(c)} = \mathbf{M}_{\epsilon c}\vec{I}_c \tag{2.14}$$

and the flux at the reference points due to a set of passive conductor currents $\vec{I}_g$ is given by:

$$\vec{\psi}_{\epsilon(g)} = \mathbf{M}_{\epsilon g}\vec{I}_g \tag{2.15}$$

If we equate the right hand sides of Eqs. 2.14 and 2.15, then the set of coil currents that produce the same flux at the locus of points ϵ is given by:

$$\vec{I}_c = \mathbf{M}_{\epsilon c}^{\dagger}\mathbf{M}_{\epsilon g}\vec{I}_g \tag{2.16}$$

where $\mathbf{D}_{cg} \equiv \mathbf{M}_{\epsilon c}^{\dagger}\mathbf{M}_{\epsilon g}$ is the current mapping matrix. Since $\mathbf{M}_{\epsilon c}$ is not necessarily square or of full rank, the inverse operation in Eq. 2.16 denoted by $\dagger$ is the so–called pseudoinversion based on the singular value decomposition (SVD) of the matrix being inverted [36].

In this study, the locus of points chosen for the mapping is the set of the 190 points on the spatial grid of the equilibrium solver where the poloidal flux is closest to the the value of the poloidal flux on the plasma edge. The locus for a typical shot is shown in Fig. 2-3. The error in the mapping is minimized in this way in the area where the plasma is.

We now return to the circuit equation. We write the circuit equation for the coils as:

$$\mathbf{M}_{cc}\dot{\vec{I}}_c + \mathbf{X}_{cc}\vec{I}_c + \mathbf{M}_{cg}\dot{\vec{I}}_g + \mathbf{X}_{cg}\vec{I}_g + \mathbf{R}_c\vec{I}_c = \vec{V}_c \tag{2.17}$$

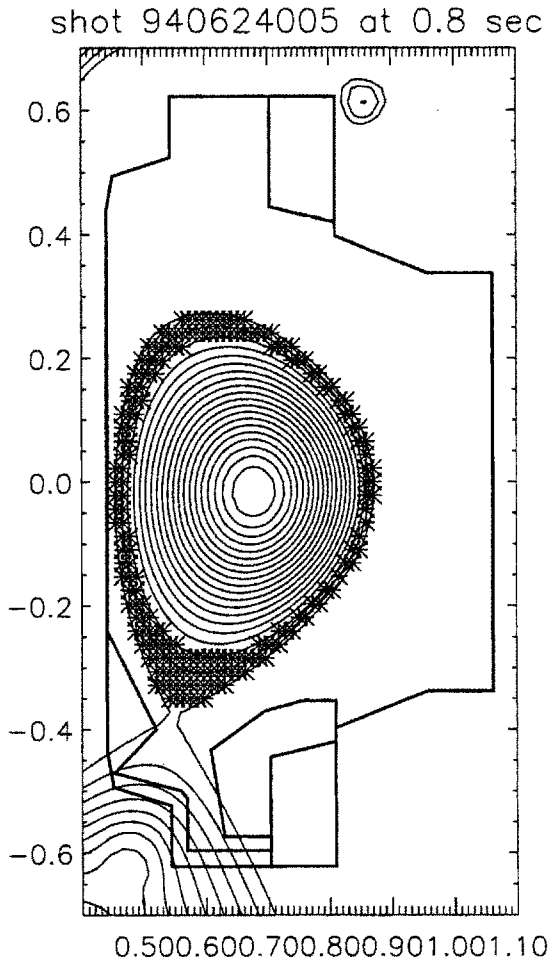

Figure 2-3: Flux contours for a typical equilibrium and locus ϵ used for coil–to–vessel mapping (stars).

where the subscripts "g" and "c" refer to passive conductors and coils respectively.

$$\mathbf{X}_{cc} = \left.\frac{d\vec{\psi}_{c(p)}}{d\vec{I}_c}\right|_{J(\psi)} \tag{2.18}$$

and

$$\mathbf{X}_{cg} = \mathbf{X}_{cc}\mathbf{D}_{cg} \tag{2.19}$$

$\vec{\psi}_{c(p)}$ is the poloidal flux due to the plasma alone at the locations of the coils for the set of perturbed equilibria. $\vec{I}_c$ are the perturbed coil currents used as inputs in the set of perturbed equilibria. The circuit equation for the passive conductors becomes then:

$$\mathbf{M}_{gg}\dot{\vec{I}}_g + \mathbf{X}_{gg}\vec{I}_g + \mathbf{M}_{gc}\dot{\vec{I}}_c + \mathbf{X}_{gc}\vec{I}_c + \mathbf{R}_g\vec{I}_g = \vec{0} \tag{2.20}$$

where

$$\mathbf{X}_{gc} = \left.\frac{d\vec{\psi}_{g(p)}}{d\vec{I}_c}\right|_{J(\psi)} \tag{2.21}$$

and

$$\mathbf{X}_{gg} = \mathbf{X}_{gc}\mathbf{D}_{cg} \tag{2.22}$$

$\vec{\psi}_{g(p)}$ is the poloidal flux due to the plasma alone at the locations of the passive conductors for the set of perturbed equilibria.

Eqs. 2.17 and 2.20 are a complete description of the system consisting of the coils, vacuum vessel, structure and plasma assuming the current profile of the plasma remains unchanged. We were able to incorporate the effect of the passive conductors without having to do any additional work as far as the perturbational equilibrium procedure is concerned.

2.3.3 Approximate Flux Conservation

As mentioned before, the assumption that the current profile of the plasma remains a constant function of ψ is incorrect. It is reasonable to assume that the plasma is a perfect conductor, however, as long as the timescale of interest is shorter than

the resistive decay timescale of the plasma, which is satisfied for typical Alcator C–Mod discharges. The plasma will move then in such a way as to conserve the magnetic flux contained in it. Ref. [32] presented an approximate way to include flux conservation in the perturbed equilibrium approach for the plasma response.

A useful quantity related to flux in the tokamak configuration is the safety factor, q, which is defined as the ratio of toroidal to poloidal angle traversed as one moves along a magnetic field line:

$$q \equiv \frac{\Delta\phi}{\Delta\theta} \tag{2.23}$$

If we define the toroidal flux through a magnetic surface of poloidal flux ψ as ψ_t, then the safety factor can be written as ([6]):

$$q(\psi) = \frac{d\psi_t(\psi)}{d\psi} \tag{2.24}$$

According to this equation, in order for both poloidal and toroidal flux to be conserved, the $q(\psi)$ profile must remain constant.

The equilibrium solver used in this study, ASEQ, does not give the user the ability to specify the $q(\psi)$ profile as an input. It is conceivable to have an equilibrium code that lets some of the coil currents float so that the required $q(\psi)$ profile ensues. Such a code would have similar disadvantages as those mentioned earlier for fixed boundary equilibrium solvers. Allowing more than one coil current to vary at once confuses the issue of trying to span the space defined by the available degrees of freedom. Using ASEQ in an iterating process that would create a set of perturbed equilibria with $q(\psi)$ profile equal to that of the base equilibrium would be too time consuming.

It is, however, possible to have approximate flux conservation if we run two additional perturbed equilibria with the same coil currents as the base equilibrium – except for the EFC coil variation necessary for numerical stability – where we

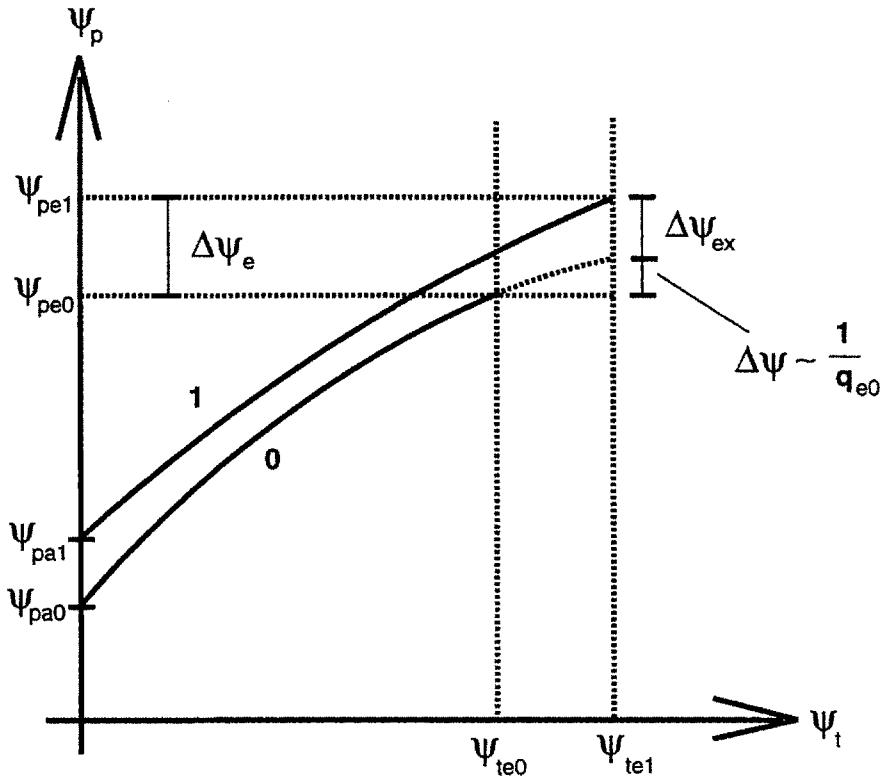

Figure 2-4: Quantities involved in the approximate edge flux conservation.

perturb the two parameters associated with the $F(\psi)$ profile. These quantities are: I_p, the total plasma current, and α_f, the profile parameter in Eq. 2.13. We can use this variation then to satisfy two constraints pertaining to flux conservation.

Fig. 2-4 shows a sketch of poloidal flux as a function of toroidal flux for the base equilibrium (subscript "0") and a perturbed equilibrium (subscript "1"). Since the magnetic axis is a magnetic surface of zero cross-sectional area, the toroidal flux on axis is always zero. One obvious quantity to be conserved, therefore, is the poloidal flux on the magnetic axis, ψ_{pa}. The second constraint should then have something to do with the plasma edge. Both the poloidal and toroidal flux change at the edge. We would like points (ψ_{te0},ψ_{pe0}) and (ψ_{te1},ψ_{pe1}) to coincide in Fig. 2-4. We can linearly extrapolate the base equilibrium curve until it meets the $\psi_t = \psi_{te1}$ line. Using Eq. 2.24

$$\frac{\Delta\psi_{pe}}{\Delta\psi_{te}} = \frac{1}{q_{e0}} \tag{2.25}$$

where q_{e0} is the safety factor at the edge for the base equilibrium. We can see then that a reasonable quantity to conserve is:

$$\psi_{ex} \equiv \psi_{pe} - \frac{\psi_{te}}{q_e} \tag{2.26}$$

In order to avoid any singularities associated with the separatrix in diverted plasmas, the edge has been defined in this study as the flux surface where the poloidal flux is equal to 95% of the separatrix value.

Defining the vector of parameters to be perturbed as:

$$\vec{p} \equiv \begin{bmatrix} I_p \\ \alpha_f \end{bmatrix}, \tag{2.27}$$

and the quantities to be conserved as:

$$\vec{\psi}_x \equiv \begin{bmatrix} \psi_{ex} \\ \psi_{pa} \end{bmatrix}, \tag{2.28}$$

the constraints become:

$$\Delta\vec{\psi}_x = \frac{\partial\vec{\psi}_x}{\partial\vec{I}_c}\Delta\vec{I}_c + \frac{\partial\vec{\psi}_x}{\partial\vec{p}}\Delta\vec{p} = \vec{0} \tag{2.29}$$

One can append the $\vec{p}$ variation to the circuit equation and then use these constraints to eliminate $\vec{p}$. The circuit equation for the coils now becomes:

$$\mathbf{M}_{cc}\dot{\vec{I}}_c + \left.\frac{\partial\vec{\psi}_{c(p)}}{\partial\vec{I}_c}\right|_{\vec{p}}\dot{\vec{I}}_c + \mathbf{M}_{cg}\dot{\vec{I}}_g + \left.\frac{\partial\vec{\psi}_{c(p)}}{\partial\vec{I}_c}\right|_{\vec{p}}\mathbf{D}_{cg}\dot{\vec{I}}_g + \left.\frac{\partial\vec{\psi}_{c(p)}}{\partial\vec{p}}\right|_{\vec{I}_c}\dot{\vec{p}} + \mathbf{R}_c\vec{I}_c = \vec{V}_c \tag{2.30}$$

The matrices involved with the variation of the coil currents while the $F(\psi)$ profile parameters remain constant are the same as in the previous section:

$$\mathbf{X}_{cc} = \left.\frac{\partial\vec{\psi}_{c(p)}}{\partial\vec{I}_c}\right|_{\vec{p}}, \qquad \mathbf{X}_{cg} = \left.\frac{\partial\vec{\psi}_{c(p)}}{\partial\vec{I}_c}\right|_{\vec{p}}\mathbf{D}_{cg} \tag{2.31}$$

We can write:

$$\dot{\vec{p}} = \frac{\partial\vec{p}}{\partial\vec{I}_c}\dot{\vec{I}}_c \tag{2.32}$$

and extract $\frac{\partial\vec{p}}{\partial\vec{I}_c}$ from Eq. 2.29:

$$\frac{\partial\vec{p}}{\partial\vec{I}_c} = -\left(\frac{\partial\vec{\psi}_x}{\partial\vec{p}}\right)^{-1}\left(\frac{\partial\vec{\psi}_x}{\partial\vec{I}_c}\right) \tag{2.33}$$

Defining:

$$\mathbf{Y}_{cc} \equiv \left.\frac{\partial\vec{\psi}_{c(p)}}{\partial\vec{p}}\right|_{\vec{I}_c}\frac{\partial\vec{p}}{\partial\vec{I}_c}, \tag{2.34}$$

and

$$\mathbf{Y}_{cg} \equiv \mathbf{Y}_{cc}\mathbf{D}_{cg}, \tag{2.35}$$

we can rewrite the circuit equation for the coils as:

$$\left(\mathbf{M}_{cc} + \mathbf{X}_{cc} + \mathbf{Y}_{cc}\right)\dot{\vec{I}}_c + \left(\mathbf{M}_{cg} + \mathbf{X}_{cg} + \mathbf{Y}_{cg}\right)\dot{\vec{I}}_g + \mathbf{R}_c\vec{I}_c = \vec{V}_c \tag{2.36}$$

The circuit equation for the passive conductors then becomes:

$$(\mathbf{M}_{gg} + \mathbf{X}_{gg} + \mathbf{Y}_{gg})\,\dot{\vec{I}}_g + (\mathbf{M}_{gc} + \mathbf{X}_{gc} + \mathbf{Y}_{gc})\,\dot{\vec{I}}_c + \mathbf{R}_g \vec{I}_g = \vec{0} \tag{2.37}$$

where

$$\mathbf{Y}_{gc} = \left.\frac{\partial \vec{\psi}_{g(p)}}{\partial \vec{p}}\right|_{\vec{I}_c} \frac{\partial \vec{p}}{\partial \vec{I}_c} \tag{2.38}$$

and

$$\mathbf{Y}_{gg} = \mathbf{Y}_{gc}\mathbf{D}_{cg} \tag{2.39}$$

Eqs. 2.36 and 2.37 can be combined then into one matrix equation:

$$(\mathbf{M} + \mathbf{X} + \mathbf{Y})\,\dot{\vec{I}} + \mathbf{R}\vec{I} = \vec{V} \tag{2.40}$$

where $\vec{I} = \begin{bmatrix} \vec{I}_g \\ \vec{I}_c \end{bmatrix}$, $\vec{V} = \begin{bmatrix} \vec{0} \\ \vec{V}_c \end{bmatrix}$, and the matrices have been put together from the submatrices appearing in Eqs. 2.36 and 2.37.

Eq. 2.40 is a linear, non–rigid, approximately flux–conserving model for the response of the system consisting of the plasma, the coils, the vacuum vessel and the structure. It will be used in Chapters 5 and 6 where it will be compared to experimentally observed plasma response with and without feedback.

One has to be careful with the amount by which one perturbs the currents and the plasma current density equilibrium parameters. If the perturbation is too large, linear theory is invalid. If the perturbation is too small, machine accuracy problems may arise. In both cases, the growth rate of a vertically unstable plasma as calculated by the perturbed equilibrium model will change as the size of the perturbation changes. This is illustrated in Fig. 2-5. There is a band of perturbation sizes in the middle, however, where the growth rate does not change as the size of the perturbation changes. This is the convergence region.

A VAX machine with a 32–bit single precision representation of a number in FORTRAN single precision has a machine accuracy ϵ_m of around 1 x 10^{-7}. Because of the finite machine accuracy, every arithmetic operation introduces a roundoff

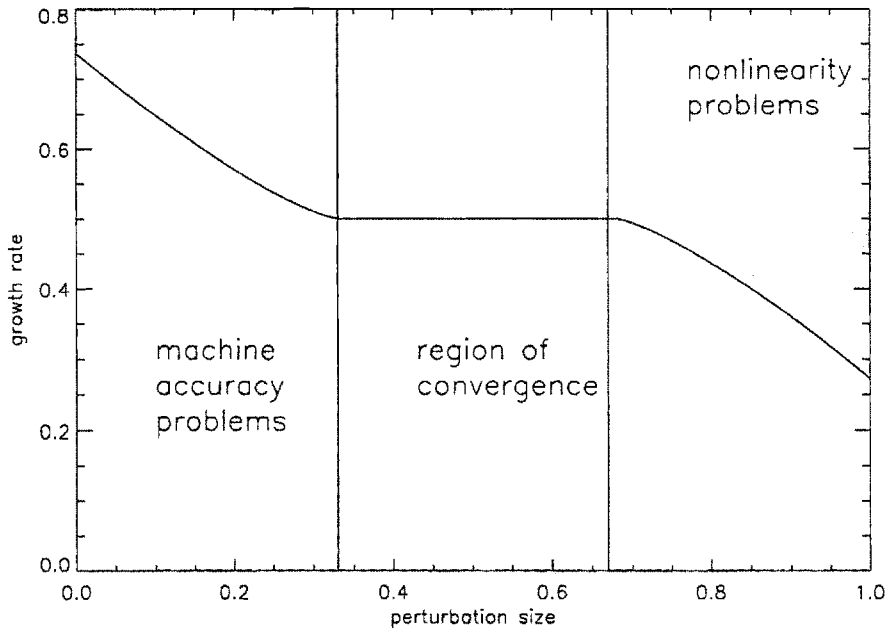

Figure 2-5: Illustration of the convergence band of perturbation sizes.

fractional error of at least ϵ_m. If N operations are performed, the total roundoff error will be, in the best case when errors add up randomly, $\sqrt{N}\epsilon_m$ [37]. For an equilibrium code which solves a second order partial differential equation on a 65 x 65 grid, N could be taken as the number of grid points and the roundoff error is of the order of 1 x 10^{-5}. Running the same code in double precision, however, one has ϵ_m of around 1 x 10^{-14} and a roundoff error of the order of 1 x 10^{-12}. This provides additional freedom, when a convergence study is performed, ie, when the amounts of perturbation are varied, until a range of values is reached where the results do not vary considerably. With increased machine accuracy this convergence band is wider.

2.4 State Space Representation

A dynamic system can be viewed as a box with a set of inputs and a set of outputs. Inputs are the quantities that can be varied from the outside world in order to control the system, while outputs are the quantities that can be measured in the outside world in order to observe the state of the system. The state of the dynamic system is described by a set of physical quantities, the state variables, that are necessary to describe its time evolution. The state may or may not be directly controllable by the inputs and it may or may not be completely observable by the outputs. The state variables may not be unique, i.e., there may be several equivalent state space representations of the same system. The time evolution of these state variables can be described by a set of ordinary differential equations. The variables that appear when this set of equations has been written as a set of first–order equations are the state variables. Suppose we have n state variables, $x_1, x_2, ..., x_n$ and m inputs, $u_1, u_2, ..., u_m$, and we have found the first–order differential equation for the time evolution of the state:

$$\dot{x}_1 = \frac{dx_1}{dt} = f_1(x_1, x_2, ..., x_n, u_1, u_2, ..., u_m, t)$$

$$\dot{x}_2 = \frac{dx_2}{dt} = f_2(x_1, x_2, ..., x_n, u_1, u_2, ..., u_m, t)$$

$$.....$$

$$\dot{x}_n = \frac{dx_n}{dt} = f_n(x_1, x_2, ..., x_n, u_1, u_2, ..., u_m, t)$$

Defining the state vector and the input vector:

$$\vec{x} \equiv \begin{bmatrix} x_1 \\ . \\ x_n \end{bmatrix} \qquad \vec{u} \equiv \begin{bmatrix} u_1 \\ . \\ u_m \end{bmatrix}$$

the state equations can be put in vector form:

$$\dot{\vec{x}} = \frac{d\vec{x}}{dt} = \vec{f}(\vec{x}, \vec{u}, t)$$

To linearize these equations, suppose that we are operating in the vicinity of $\vec{x} = \vec{x}_0$ and $\vec{u} = \vec{u}_0$. Then $\vec{x}(t) = \vec{x}_0 + \Delta\vec{x}(t)$ and $\vec{u}(t) = \vec{u}_0 + \Delta\vec{u}(t)$. The linearized state equation then becomes:

$$\Delta\dot{\vec{x}} = \mathbf{A}(t)\Delta\vec{x}(t) + \mathbf{B}(t)\Delta\vec{u}(t)$$

where

$$\mathbf{A} \equiv \frac{\partial\vec{f}}{\partial\vec{x}}$$

$$\mathbf{B} \equiv \frac{\partial\vec{f}}{\partial\vec{u}}$$

Dropping the "Δ", with the understanding that we are dealing in perturbed quantities only and assuming that $\mathbf{A}$ and $\mathbf{B}$ do not vary with time, we get the following equation for a linear time–invariant system:

$$\dot{\vec{x}} = \mathbf{A}\vec{x} + \mathbf{B}\vec{u} \tag{2.41}$$

$\mathbf{A}$ is known as the response matrix of the system.

Since we usually do not have access to the state vector of a physical system, we need some equation to relate the state vector to the quantities we can measure, the outputs. In a linear system, the outputs will be linear combinations of the inputs and the state variables. If we have l outputs, $y_1, y_2, ..., y_l$, the output vector

$$\vec{y} \equiv \begin{bmatrix} y_1 \\ . \\ y_m \end{bmatrix}$$

is given by:

$$\vec{y} = \mathbf{C}\vec{x} + \mathbf{D}\vec{u} \tag{2.42}$$

This is known as the output equation. Eqs. 2.41 and 2.42 are a complete description of the relationship between the inputs and the outputs in the time domain.

The dynamics of the system we are interested in are described by Eq. 2.2 or Eq. 2.40. The state vector consists of all the currents in the conductors, or $\vec{x} = \vec{I}$.

The input vector consists of the voltages applied to the conductors, or $\vec{u} = \vec{V}$. These dynamics can be cast into the standard state equation form by writing:

$$\mathbf{A} = -(\mathbf{M} + \mathbf{X} + \mathbf{Y})^{-1}\mathbf{R}$$

$$\mathbf{B} = (\mathbf{M} + \mathbf{X} + \mathbf{Y})^{-1}$$

The output vector in our case consists of the magnetic diagnostic signals (poloidal flux loop signals, $\vec{\psi}$, and poloidal field coil signals, $\vec{B}_p$). These are given by:

$$\begin{bmatrix} \vec{\psi} \\ \vec{B}_p \end{bmatrix} = \begin{bmatrix} \mathbf{N} \\ \mathbf{G} \end{bmatrix} \vec{I} \tag{2.43}$$

where $\mathbf{N}$ is the mutual inductance matrix between the toroidal flux loops and the conductors and $\mathbf{G}$ is the matrix of Green's functions between conductors and poloidal field coil locations integrated over the cross sectional area of the conductors (assuming a uniform current density is flowing through the conductors). Eq. 2.43 can be cast into the standard output equation terminology by writing:

$$\vec{y} = \begin{bmatrix} \vec{\psi} \\ \vec{B}_p \end{bmatrix}$$

$$\mathbf{C} = \begin{bmatrix} \mathbf{N} \\ \mathbf{G} \end{bmatrix}$$

$$\mathbf{D} = \mathbf{0}$$

By means of Laplace transforms, one can derive from the state and output equations a relationship between the input and the output for the frequency domain:

$$\vec{y}(s) = \left[\mathbf{C}\,(s\mathbf{1} + \mathbf{A})^{-1}\,\mathbf{B} + \mathbf{D}\right]\vec{u}(s) \equiv \mathbf{G}(s)\vec{u}(s) \tag{2.44}$$

where $\mathbf{1}$ is the unit matrix and $\mathbf{G}(s)$ is known as the transfer function. In a single–input, single–output (SISO) system, this relationship is scalar and the frequency domain representation may be more convenient. For MIMO systems however, the

state space formulation in the time domain can be more useful, since the transfer function is a matrix of functions which is harder to visualize. This formulation will be referred to often in the following chapters.

In the following chapters, linear models will be developed for the subsystems of the Alcator C–Mod tokamak. These will be put together into one closed–loop system in Chapter 6. It is necessary to know how to append two linear systems in series for this purpose. Suppose that we have two systems in series and that the output of the first is the input of the second. The state and output equations of the first system are:

$$\dot{\vec{x}}_1 = \mathbf{A}_1\vec{x}_1 + \mathbf{B}_1\vec{u}_1$$

$$\vec{u}_2 = \mathbf{C}_1\vec{x}_1 + \mathbf{D}_1\vec{u}_1$$

Those of the second system are:

$$\dot{\vec{x}}_2 = \mathbf{A}_2\vec{x}_2 + \mathbf{B}_2\vec{u}_2$$

$$\vec{y}_2 = \mathbf{C}_2\vec{x}_2 + \mathbf{D}_2\vec{u}_2$$

The combined system then has

$$\vec{x} = \begin{bmatrix} \vec{x}_1 \\ \vec{x}_2 \end{bmatrix}$$

as its state vector, $\vec{u} = \vec{u}_1$ as its input vector and $\vec{y} = \vec{y}_2$ as its output vector. The matrices associated with the state equation of the combined system can easily be shown to be:

$$\mathbf{A} = \begin{bmatrix} \mathbf{A}_1 & \mathbf{0} \\ \mathbf{B}_2\mathbf{C}_1 & \mathbf{A}_2 \end{bmatrix} \tag{2.45}$$

$$\mathbf{B} = \begin{bmatrix} \mathbf{B}_1 \\ \mathbf{B}_2\mathbf{D}_1 \end{bmatrix} \tag{2.46}$$

$$\mathbf{C} = \begin{bmatrix} \mathbf{D}_2\mathbf{C}_1 & \mathbf{C}_2 \end{bmatrix} \tag{2.47}$$

$$\mathbf{D} = [\mathbf{D}_2\mathbf{D}_1] \tag{2.48}$$

We have thus a compact formulation of the models of the conductors, the plasma, the diagnostics and the power supplies, which lends itself to computations for control purposes.

Chapter 3

Modeling of the Structure and the Power Supplies

3.1 Vacuum Vessel and Structure Modeling

It is obvious that the values for the resistances and inductances one uses in matrices **M** and **R** (eq. 2.1) determine to a large extent the response of the conductor/plasma system. The vacuum vessel containing the plasma, which carries a large toroidal current has to be able to withstand the mechanical stresses due to the large eddy currents which can arise when the plasma moves or the currents in the PF and OH coils change. It is clear then that the vacuum vessel has to be thick in order to sustain these stresses. Insulating breaks would weaken it and were ruled out in the design. The thick vacuum vessel is good from a passive stabilization point of view, but slows down the active control. A thin vessel, on the other hand, would allow much faster active control, since the fields generated by the coils can diffuse through it more quickly, but it is not as good for passive stabilization by means of eddy currents.

Since, in an experimental tokamak like Alcator C–Mod, one would like to

examine a wide variety of plasma shapes, a further complication is introduced by a vacuum vessel that is not conformal to the plasma, i.e., its distance from the plasma edge varies significantly with poloidal angle. In addition, vacuum vessels with corners are easier to machine than smooth conformal ones, and this was an issue with Alcator C–Mod. In order for the TF magnets to withstand the mechanical stresses associated with producing a large magnetic field, they have to rest against large pieces of structural material. This is the reason for the massive domes and cylinder surrounding the TF coils (see Fig. 1-5). These components are so thick that the total resistance of a dome, for example, is comparable to the PF coil resistances. Accurate modeling of the electromagnetic coupling of this structure and the vacuum vessel to the coils, the plasma and the magnetic diagnostic measurements is essential for the analysis of dynamic control of the position and shape of the plasma.

3.1.1 The Electromagnetic Model

An initial attempt to divide the coil/vessel/structure system into elements and experimentally measure their resistances and inductances was soon aborted, since the vessel and structure are the majority of the elements and they do not have input/output "terminals", i.e. no voltage can be applied externally to these elements and no measurement can be made of the current they carry, since the flux loops and the B_p–coils are located inside the vacuum vessel. Measurement of the eddy currents in the vacuum vessel would only be possible if there were B_p–coils located both inside and outside the vacuum vessel. Only a lumped resistance and inductive coupling to the coils of the entire vessel/structure system could be measured. In an attempt to get an accurate model of the conductor set around the plasma, the SOLDESIGN code of Pillsbury [38] was used. The vacuum vessel and the structure were divided into 190 toroidally symmetric elements of finite cross section that were assumed to be carrying a uniform current density. Then, geometry and materials

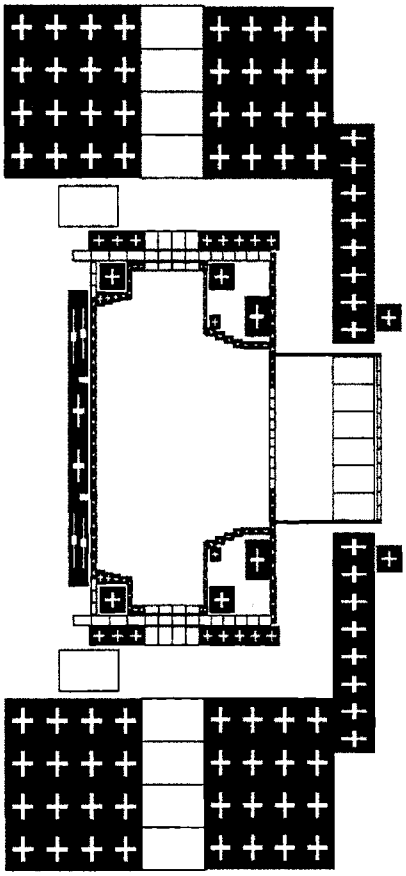

Figure 3-1: Model of Alcator C–Mod. The boxes with a "+" sign represent toroidally continuous elements. The empty boxes represent toroidally discontinuous elements that were left out of the model.

properties were used together with the Biot–Savart law for magnetic induction to estimate the resistances and inductances of the conductors. Fig. 3-1 shows how the machine was broken into elements. The 203 boxes containing a "+" sign are the elements that are included in the model while the empty boxes are elements that were left out because they have toroidal discontinuities.

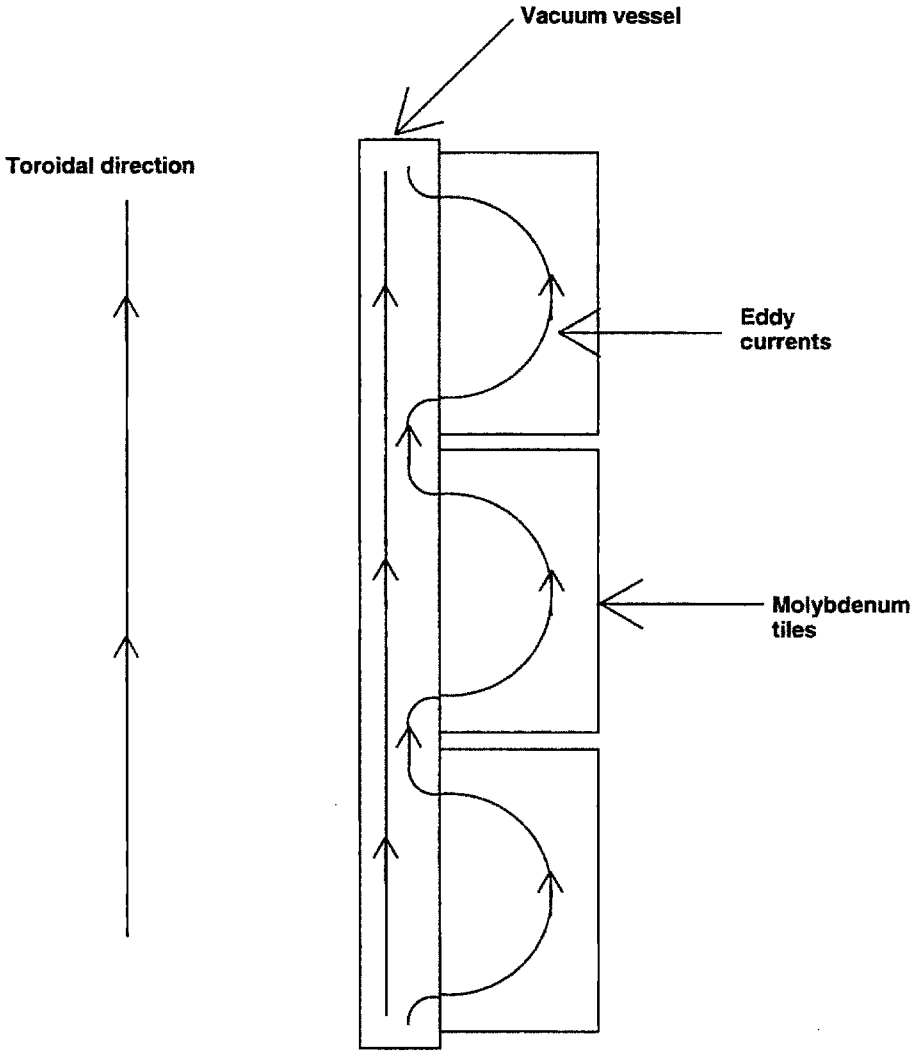

Figure 3-2: Illustration of effective toroidal current path due to the molybdenum tiles.

One detail concerning the inboard side of the vacuum vessel and the divertor region should be mentioned here. As shown in Fig. 1-6, these regions are covered with 2.5–cm thick molybdenum tiles. Molybdenum is a refractory metal and has a

higher melting point than stainless steel, the material of which the vacuum vessel is made. The reason for this is that these areas receive higher heat loads than the rest of the vacuum vessel, since ions and electrons fall onto these areas by moving parallel to the last closed flux surface, i.e., even if we assume that there is no motion of these particles perpendicular to the magnetic flux surfaces. When the plasma is diverted, the separatrix is the last closed flux surface and particles can travel directly along it and hit the divertor region. When the plasma is limited – i.e., not diverted – the last closed flux surface is essentially defined by where the plasma touches the inboard wall. In this configuration, many particles from the last closed flux surface hit the inboard wall directly. These tiles do not provide a continuous toroidal conducting path. They are, however, in contact with the vacuum vessel, and current can flow from the vacuum vessel into the tiles and back from the tiles into the vacuum vessel as shown in Fig. 3-2. This changes the effective location of any toroidal currents flowing in the inboard side of the vacuum vessel, which means that the inductive current of these elements to the other conductors and the plasma changes. The effective resistance of these elements changes as well. No attempt has been made to rigorously model these effects. Besides the fact that this is a toroidally asymmetric problem, there is no information available as to what the contact resistance between the vacuum vessel and the tiles is. The molybdenum tiles are slightly thicker than the vacuum vessel and molybdenum is more conducting that stainless steel. The effect of the tiles was thus simulated arbitrarily by calculating the mutual inductances between the inboard vacuum vessel elements and the remaining conductors and plasma by assuming that these elements are located at a radial position larger than their real radial position by a distance equal to the vacuum vessel thickness. This modification to the electromagnetic model was adopted because it seems to give consistently better agreement between theory and the experimental results presented in this chapter and in Chapter 5.

The weak point of this model is that it is toroidally symmetric and cannot

deal with toroidal asymmetries as they occur in the ports, mounting plate etc. The number of elements is alarming from a computational point of view and leads one to ask whether some order reduction is possible. This issue is pursued in Chapter 4.

3.1.2 Model Verification

A good way to evaluate the model is by putting currents through the active coils and comparing the magnetic diagnostic measurements (when there is no plasma) with an estimate of what these measurements should be, based on the model. Defining $\mathbf{N}_g$, the flux loop to vessel/structure mutual inductance matrix, $\mathbf{N}_c$, the flux loop to driven coils mutual inductance matrix, $\mathbf{G}_g$, the influence (Green's function) of the vessel/structure on the B_p–coils, and $\mathbf{G}_c$, the influence of the driven coils on the B_p–coils, the circuit equation for the vacuum vessel/structure currents can be written as

$$\mathbf{M}_{gg}\dot{\vec{I}}_g + \mathbf{M}_{vc}\dot{\vec{I}}_c + \mathbf{R}_{gg}\vec{I}_g = \vec{0} \tag{3.1}$$

where the subscript "c" refers to the active coils and the subscript "g" refers to the vacuum vessel and the structure. Since $\vec{I}_c(t)$ is measured, one can solve Eq. 3.1 for $\vec{I}_g(t)$ starting at times when there were no currents flowing in any of the coils, with $\vec{I}_g(t=0) = \vec{0}$ and insert into the equations for the flux loops

$$\vec{\psi} = \mathbf{N}_g\vec{I}_g + \mathbf{N}_c\vec{I}_c \tag{3.2}$$

and for the B_p–coils

$$\vec{B}_p = \mathbf{G}_g\vec{I}_g + \mathbf{G}_c\vec{I}_c \tag{3.3}$$

As the current flows from one leg of the TF coil to the next, it has to flow in the toroidal direction and it has to be taken into account. This TF current contribution

has been modeled as the two large white blocks shown on the inboard side in Fig. 3-1. The current flowing in these elements has been included in the source term, $\dot{\vec{I}}_c$, in eq. 3.1 and in eqs 3.2 and 3.3 as an additional pair of coils. Since, however, these elements are connected to the TF coil, which has a self–inductance much larger than the mutual inductance between them and the coils, vessel or structure, it is safe to assume that no eddy currents are induced in these toroidal elements simulating the toroidal extent of the TF coil, so that no additional circuit equation is needed for these elements in eq. 2.1.

A most useful test of the model would be to put oscillating currents into the coils and compare estimated and measured values of the magnetic diagnostics. Differences in phase and magnitude between them could give quantitative insight as to where potential errors in the model lie. This was done in ASDEX–U [21, 22], by exciting the pair of control coils at different frequencies. These coils are located inside the vacuum vessel as are the magnetic diagnostics. In Alcator C–Mod, all coils are located outside a thick toroidally continuous vacuum vessel, while all the magnetic diagnostics are located inside. This means that even high amplitude current oscillations in the coils will not be seen in the diagnostics unless they are of very low frequency. This filtering effect was observed in the power supply characterization runs (see Section 3.2) where 20–Hz oscillations in the power supply voltage with amplitude of the same order of magnitude as the power supply operating limit were hardly visible in the magnetic signals.

Instead of oscillations, shots with steps in the coil currents were used to test the electromagnetic model. Fig. 3-3 shows a comparison between predicted and actual values of some of the flux loop signals for a no–plasma case with nine driven coils. Fig. 3-4 shows a comparison between predicted and actual values of some of the B_p–coil signals for the same shot. This case is from the 1994 run period of Alcator C–Mod and it was meant to be plasma shot, but a failure in the OH1 power supply made breakdown impossible. We see that the error is less than 10%. It is

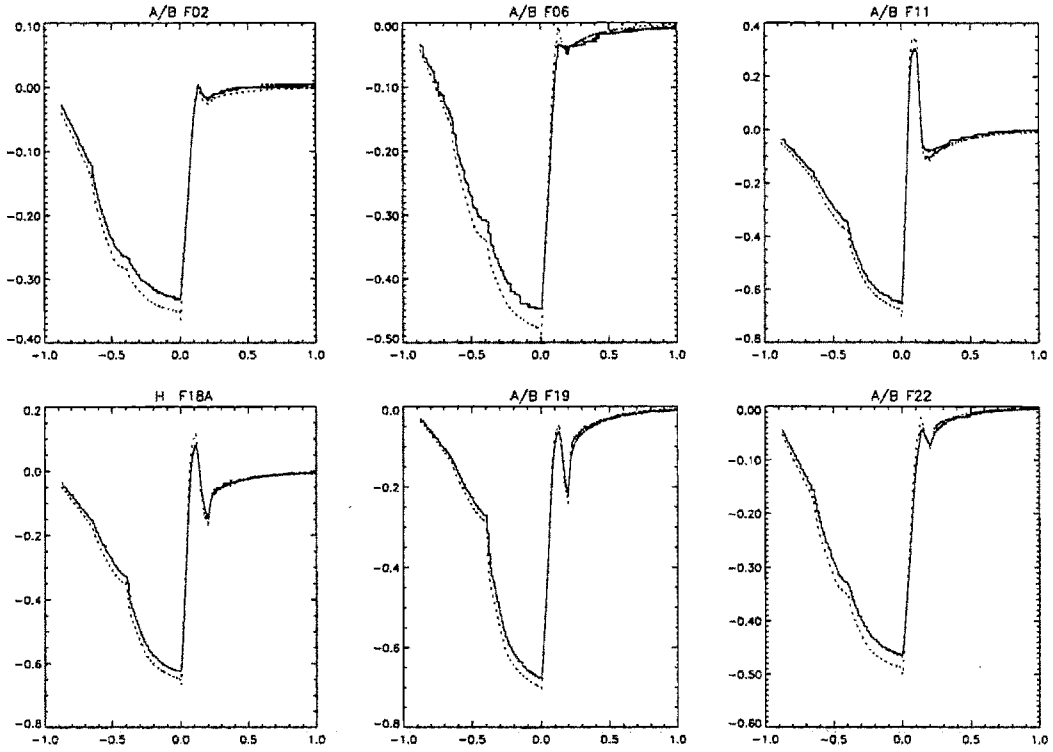

Figure 3-3: Comparison between flux loop signals (solid line) and their values as estimated from the measurements of the currents flowing in the coils using the 190–element model of the vessel and structure (dotted line).

noteworthy, that the estimated signals are qualitatively identical to the actual signals, namely they are neither slower nor faster in their response to current changes, even though their values may be slightly different. One source of such discrepancy could be some faulty calibration of the coil current or magnetic diagnostic signals. Another source could be errors in the influences from the coils, vessel, and structure to the magnetic diagnostics, since they are only used in eqs 3.2 and 3.3 which have no time dependence. Any error in the mutual inductances or the resistances of the coils, vessel, and structure would cause a time dependent discrepancy between measured and estimated signals. The only case where the discrepancy is alarming

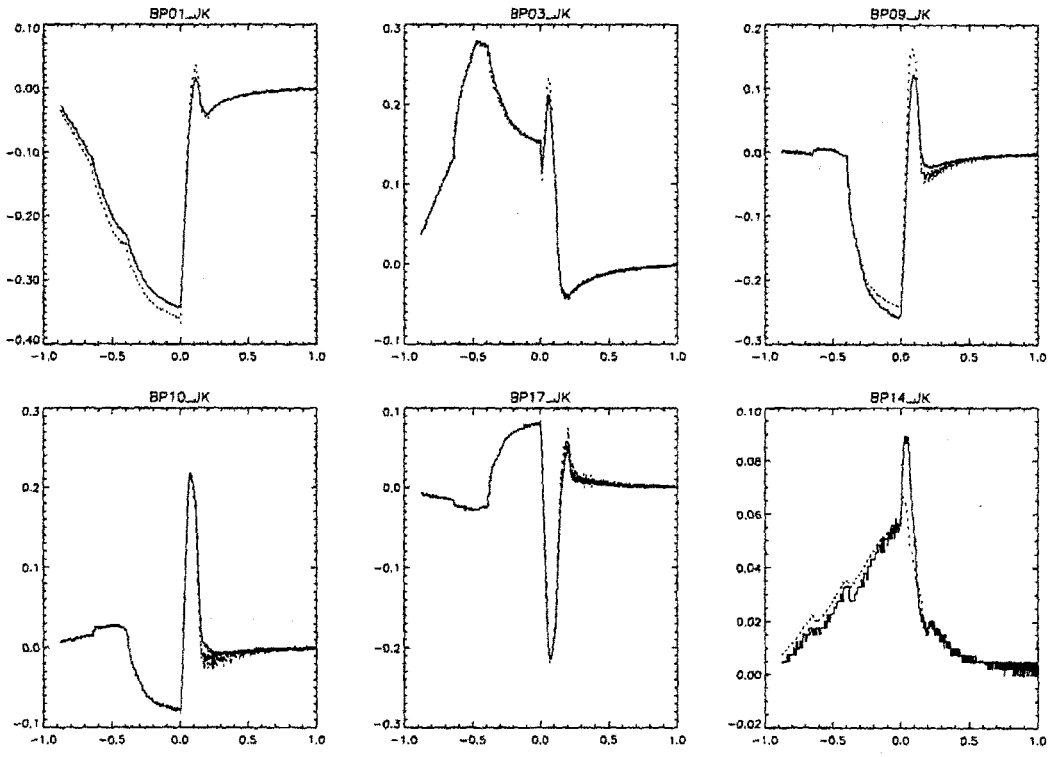

Figure 3-4: Comparison between B_p–coil signals (solid line) and their values as estimated from the measurements of the currents flowing in the coils using the 190-element structure/vessel model (dotted line).

is the lower right signal in Fig. 3-4 which is from a B_p–coil located between two horizontal ports. This was expected since the toroidal asymmetry of the ports cannot be modeled exactly by this toroidally symmetric model.

3.1.3 A Secondary Application

As we shall see in Chapters 5 and 6, the primary use of the electromagnetic model of the coils, vacuum vessel, and structure is in plasma equilibrium reconstruction and in determining the axisymmetric plasma response. In addition to that, however, it turned out to be of some use in arriving at a repeatable breakdown scenario during the beginning of the 1993 Alcator C–Mod campaign.

At the moment of breakdown, a toroidal loop voltage between 10 and 20 V is applied inductively causing some of the atoms in the gas filling the vacuum chamber to be ionized. The resulting electrons and ions follow a spiral trajectory along the magnetic field lines until they either reach the vacuum vessel wall or collide with a neutral atom and ionize it. It is desirable that these first electrons and ions stay inside the vacuum vessel as long as possible so as to ionize several neutral atoms. Any poloidal field in the vacuum vessel region will send them in the direction of the wall. This is due to the fact that, in the absence of plasma, there are no toroidal current sources inside the vacuum vessel and, according to Ampere's law, there can be no closed poloidal field lines inside the vessel wall. Electrons and ions born in an area where there is no poloidal field will follow the toroidal field lines until they collide. Therefore their chance to cause a second ionization will be much larger. For this reason, it is important to have as large a region of zero poloidal field as possible inside the vacuum vessel during breakdown.

This is difficult to achieve mainly because large amounts of eddy currents are created in the vacuum vessel wall by the toroidal loop voltage needed for breakdown. These currents create a large amount of poloidal field inside the vacuum vessel, and the PF coils must be used to cancel this field. Fig. 3-5 shows the poloidal flux for a shot that had plasma, at a time shortly after breakdown. One can see that the poloidal field due to the measured coil currents is considerable, as is the poloidal field due to passive currents estimated using eq. 3.1. Their sum however gives a

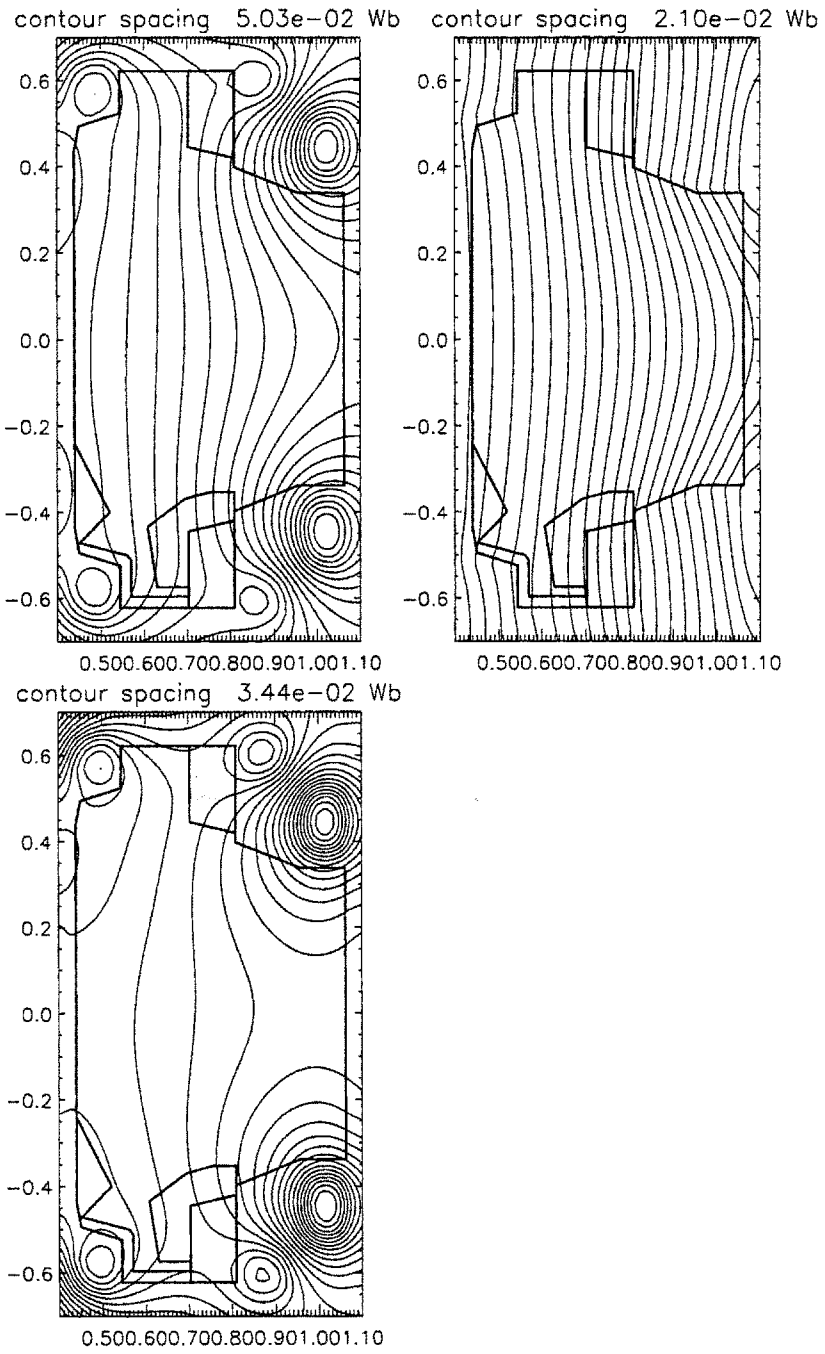

Figure 3-5: Poloidal flux due to the active coil currents (top left), passive currents (top right), and both (bottom) 50 msec after breakdown.

much lower poloidal flux density in the central part of the vacuum vessel. In theory, one could do the time integration implied by eq. 3.1 in real time and use it for feedback control. This would imply reducing the model of eq. 3.1 to a size of less than 16, the number of feedback channels of the plasma control computer. We shall see in Chapter 4 that this is not feasible. In practice, the voltages applied to the OH and PF coils must be preprogrammed so as to create a large zero–field region at the right time. The conductor model could be used in prescribing these voltages, but this would not give the millitesla accuracy that is needed for this purpose. The next best thing is to use the model in a trial–and–error process. The voltages are prescribed ignoring any passive conductors, and the shot is run. Subsequently, eq. 3.1 is used to estimate the vessel and structure currents. Then the mapping process of eq.2.16 is used to find a combination of coil currents that will create the same poloidal flux on a surface inside the vacuum vessel as the passive currents. Then enough voltage to sustain the negative of this combination of coil currents is added to the previously prescribed voltages and the shot is repeated. This time the flux density should be smaller inside the surface used for the mapping. The mapping procedure can be used again, but one eventually runs into accuracy problems, so that one has to continue with tedious fine tuning to achieve a good null-field area.

3.2 Power Supply Modeling

As we saw in Chapter 1, the OH2 and the EFC coils are vital in controlling the vertical position. Given enough elongation, the vertical instability can always cause the plasma to move more quickly than the power supply response time, so that it is important to study the dynamics of the power supplies feeding these coils and know their limitations.

3.2.1 The OH2 Power Supplies

Each of the OH2 coils is fed by a four–quadrant, 12–pulse thyristor power supply, which converts the 13.8 kV AC voltage from the alternator into a specified DC voltage. Thyristors, also known as Silicon Controlled Rectifiers (SCR's), are high power diodes with a semiconductor control mechanism (gate), which interrupts current flow in the allowed direction, unless it receives an input signal greater than some threshold. The phasing of an array of thyristors allows the output voltage to vary. These supplies are rated at ± 100 V and ± 50 kA. Following traditional power supply design, they have their own internal feedback control system. Fig. 3-6 shows a block diagram of the power supply and how it fits in the plasma control loop. The master control board adjusts the phasing of the thyristor array gates to give

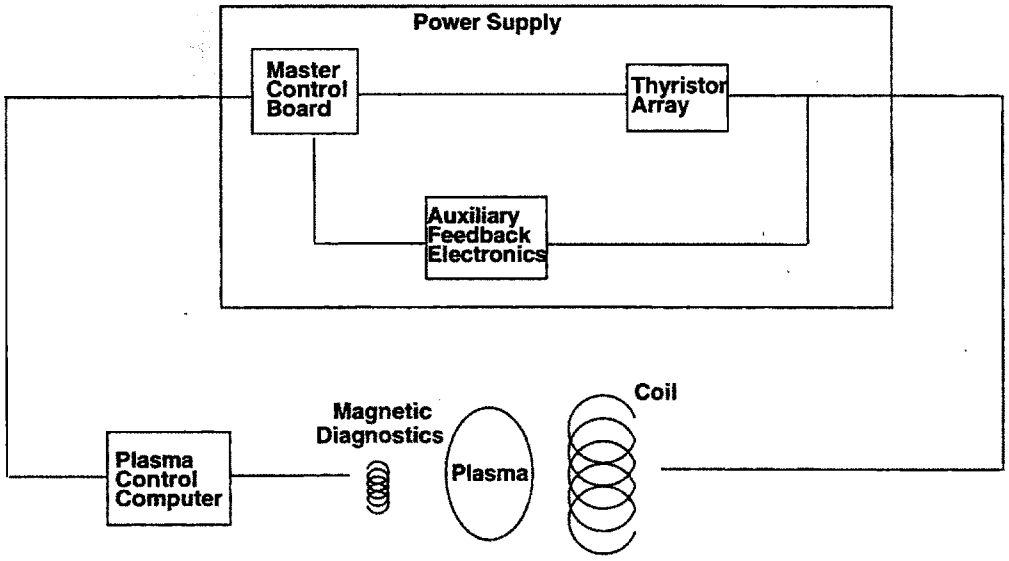

Figure 3-6: Block diagram of the power supply and its position in the plasma control loop.

the requested voltage at the output. Integral and proportional feedback are used for this purpose. The electronics of this internal control loop have a considerably more limited bandwidth than that of the plasma control computer (PCC); furthermore, the internal control loop does not have the flexibility of the PCC, since the control

scheme it offers is hardwired. It would, therefore, make more sense to do away with it and hand control of the gate phasing to the PCC directly. Little time has been devoted to this idea so far. Some shots that were run in this mode displayed a hysteresis phenomenon which made breakdown difficult. The problem was that when a zero demand was sent to the power supply, the output was not zero, but equal to –IR, where I is the current in the coil and R is the power supply impedance. This can be seen in Fig. 3-7 where the points corresponding to nearly zero demand are not near the zero output line for the shot with broken internal control loop. One could devise a scheme to compensate for this effect using the PCC, but it would involve giving up a few of the 16 feedback channels of the PCC, so they can be used for power supply voltage control. Therefore, it was decided to continue using the old configuration with the internal control loop.

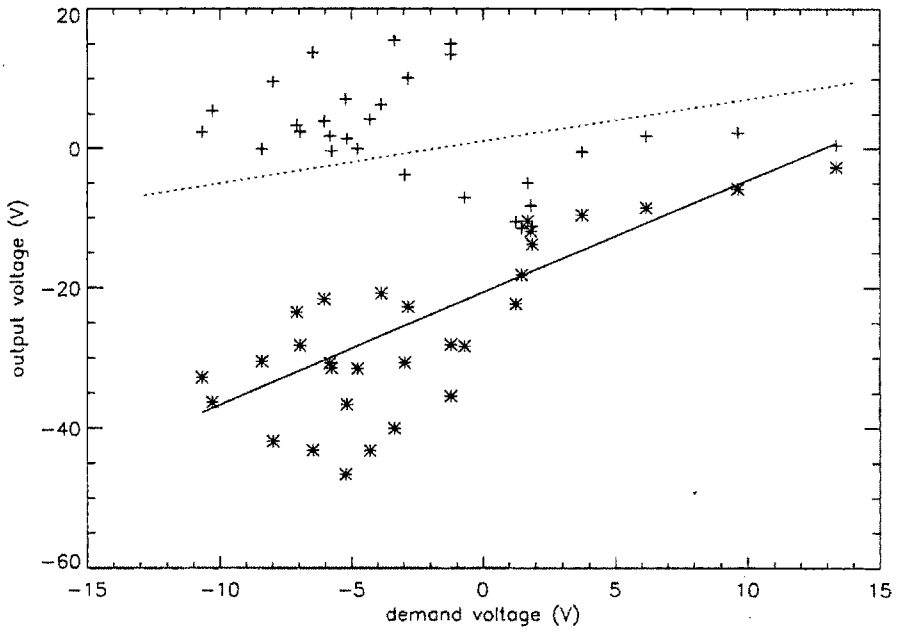

Figure 3-7: Demand versus output voltage for the OH2U power supply at a time interval of near–zero demand for a shot where the internal control loop was broken (*, solid line fit) and for a similar shot where the internal control loop was closed (+, dotted line fit).

Furthermore, it was observed that using mainly proportional gain in the internal control loop had a violent oscillation in the output voltage as a result. Fig. 3-8 shows the output of the OH2L power supply during an interval before breakdown for a shot with only proportional gain used in the power supply feedback loop. This oscillation subsided only when integral gain was applied and the proportional gain was reduced to a value much smaller than that of the integral gain. As a

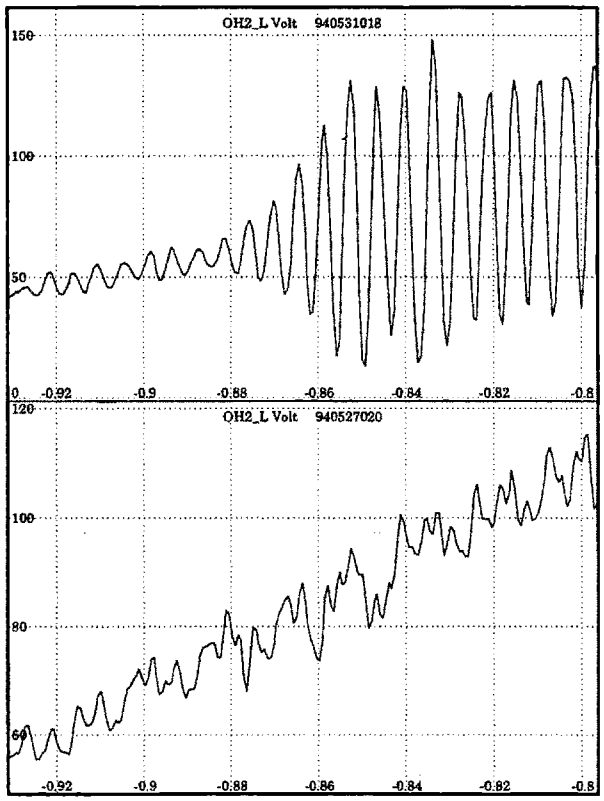

Figure 3-8: OH2L power supply output voltage before breakdown as a function of time for a shot with proportional gain in the internal feedback loop (top) compared to a typical shot with integral gain in the internal feedback loop (bottom).

result, these power supplies have so far been controlled by an internal loop based on integral gain alone. This compromises their performance somewhat.

To measure the response of the OH2 supplies experimentally the following experiment was conducted: Using the PCC for feedback, the coil currents were slowly brought up to values characteristic of the flattop of a typical shot. Then

the feedback was turned off and voltage demands, equal to the resistive voltage drop of the coils were fed to the power supplies. In addition, oscillations of various frequencies between 20 and 500 Hz were superimposed on the demand of the power supply under investigation. The amplitude of the oscillations was such as not to cause any of the power supplies to exceed its operational voltage limit. In most cases the amplitude was close to the half of the operational voltage limit, however, so the modulation was substantial. The objective was to observe the response of the power supply in the open–loop mode, i.e., when the power supply is not part of the plasma control loop. Fig. 3-9 shows an example of such a shot: the OH2L demand is being modulated at three different frequencies while OH2U demand is constant. The ratio of amplitudes and phase differences between the input and output signals were fitted (in a least squares sense) to a rational transfer function with four zeroes and five poles. The resulting transfer functions are shown in Fig. 3-10. The main message conveyed by these plots is that the power supplies cannot follow any input varying at a rate of 100 Hz or faster. Fig. 3-11 shows the output of the OH2L fitted transfer function given the measured demand signal as input. This is compared to the measured power supply voltage for that shot. The agreement is satisfactory. During these shots, measurements of the inputs and outputs of the SCR array were also available so that a transfer function of the SCR array alone could also be inferred. The transfer functions of the master control board and the auxiliary feedback electronics were measured independently. If the above three transfer functions are arranged in a closed loop as in Fig.3-6, the resulting transfer function is, as expected, close to the transfer function between the input and output of the power supply (see Fig. 3-12). If the SCR array is left out of this composite transfer function, the behavior of the composite transfer function is significantly more benign (see Fig. 3-12) leading to the conclusion that the SCR array is mainly responsible for the power supply behavior. Developing a linear model for this array from first principles, however, is beyond the scope of this work.

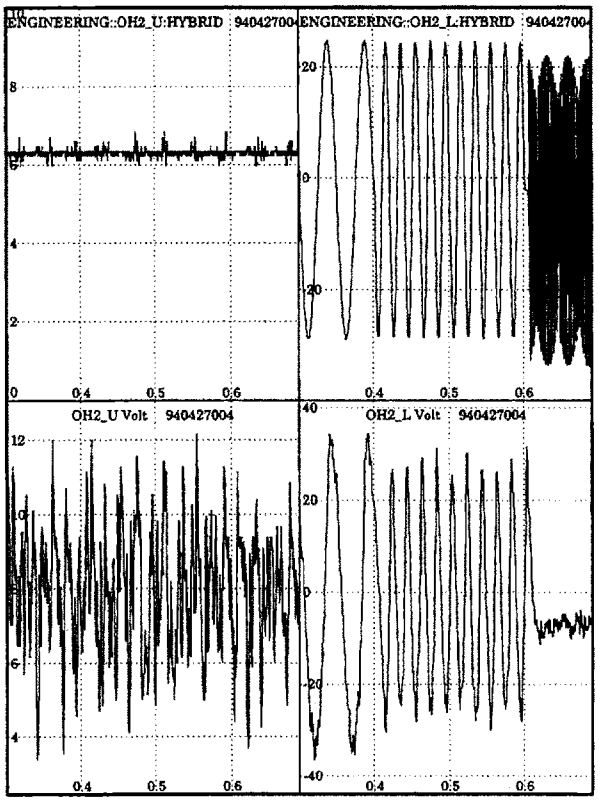

Figure 3-9: OH2U (left) and OH2L (right) power supply demand (top) and output voltage (bottom) for one of the power supply characterization shots. The fast modulation (500 Hz) demand signal is aliased.

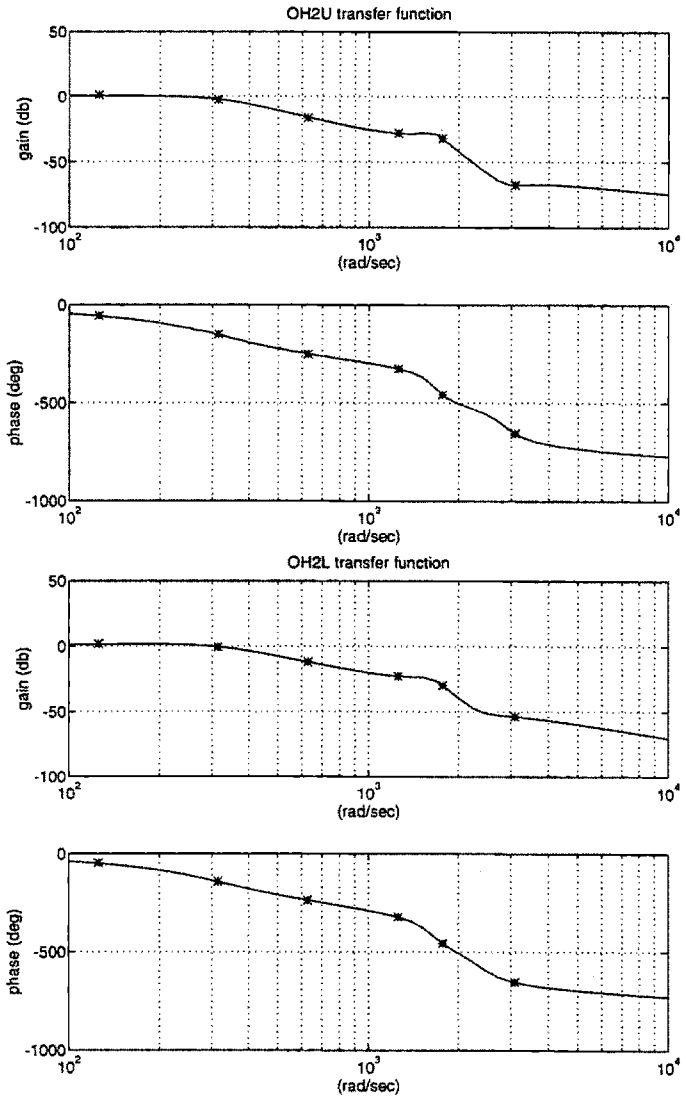

Figure 3-10: Bode plots for OH2U (top) and OH2L (bottom) power supply fitted transfer functions. The measured points are shown as stars.

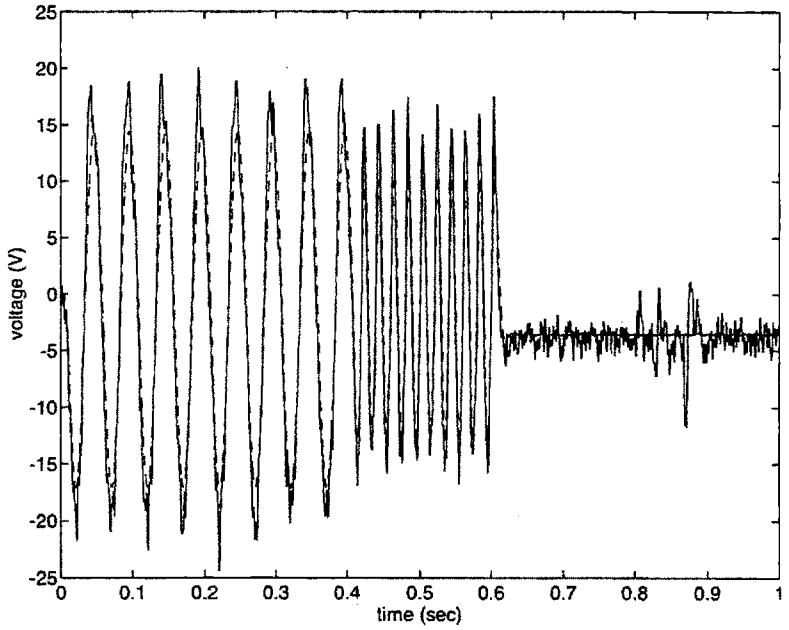

Figure 3-11: OH2L supply output voltage (solid) and simulated output voltage (dotted) for one of the power supply characterization shots. The simulated output was calculated using the fitted transfer function.

The conditions of this experiment were not exactly realistic, since no elongated plasma was present, but doing such an open–loop test with a plasma is not feasible. Closed–loop experiments of this type with a plasma, although feasible, are risky because of the fear of vertical disruptions. In many of the early highly elongated plasma shots, a persistent oscillation in the Z–position is observed at frequencies between 50 and 120 Hz, and this is the only realistic single–frequency power supply data available at this point. As an example, Fig. 3-13 shows oscillations of frequency 110 Hz. Table 3.1 shows gain and phase data for some shots and how they compare with predictions from the transfer functions of Fig. 3-10. The above experiments, which resulted in the transfer functions of Fig. 3-10, were conducted on April 27, 1994. It was the first day of the Alcator C–Mod 1994 campaign. Looking at Table 3.1, it became apparent that the measured transfer function agrees with data from 1993, but disagrees with data from the 1994 campaign. Unfortunately, the master control board was modified on the day when experiments were conducted to

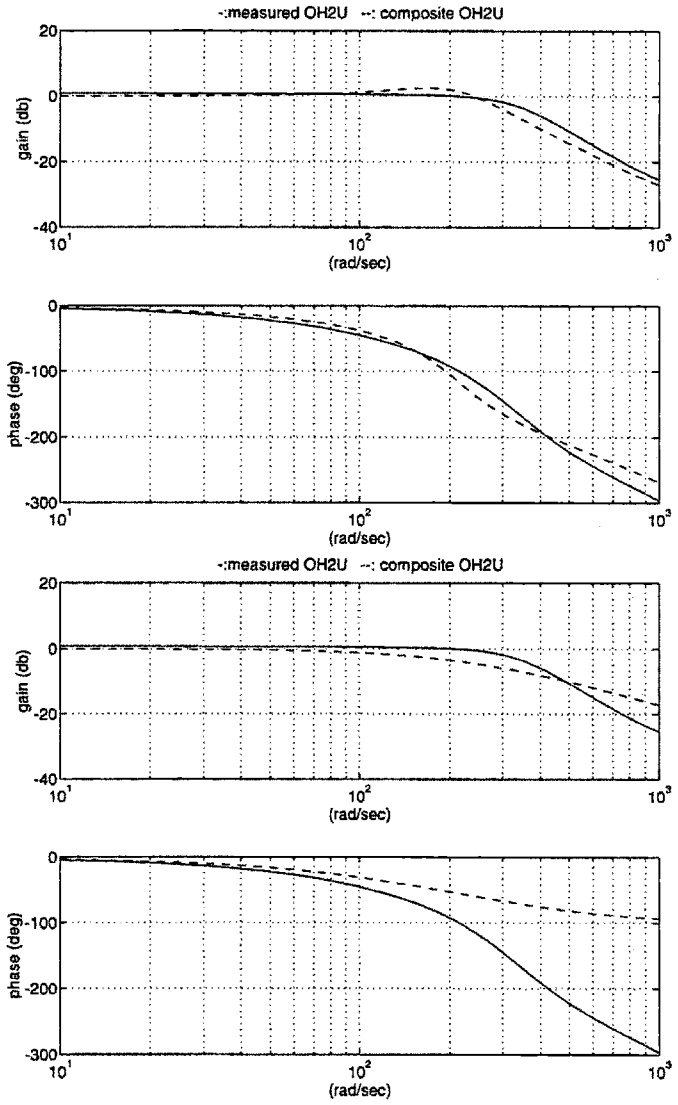

Figure 3-12: Comparison of the measured OH2U transfer function to the composite closed-loop transfer function consisting of individually measured transfer functions of the master control board, the SCR array (top only), and the auxiliary feedback electronics.

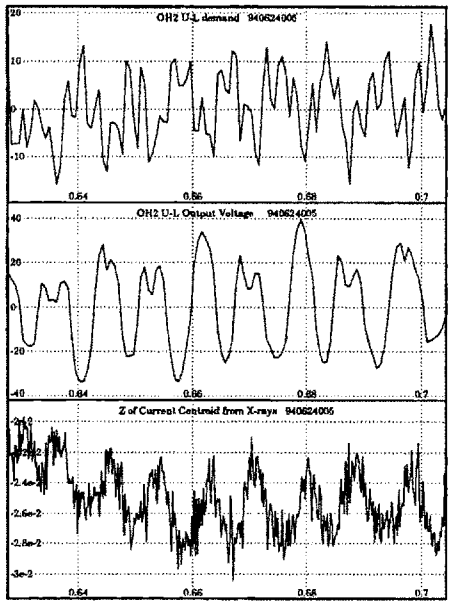

Figure 3-13: Traces characteristic of the vertical oscillation. The top two traces show the difference in demand and output between upper and lower OH2 power supplies The bottom trace is the position of the plasma current centroid as calculated from soft X–ray tomography measurements.

Shot number	plasma	frequency (Hz)	gain (measured/predicted)	phase (measured/predicted)
940624001	no	60	1.1/0.74	-116.7/-170.1
940624001	yes	60	1.1/0.74	-95.9/-170.1
940624002	yes	60	1.0/0.74	-102.1/-170.1
940624005	no	60	1.14/0.74	-116.0/-170.1
940624005	yes	110	0.56/0.21	-151.0/-247.2
930923019	yes	110	0.28/0.21	-233.0/-247.2
930923020	yes	90	0.38/0.32	-204.3/-224.1
930924005	yes	110	0.22/0.21	-218.7/-247.2

Table 3.1: OH2L gain and phase data for some shots with oscillations.

investigate the usefulness of proportional gain in the internal control loop or absence of the internal control loop (which was after April 27, 1994), and it was not brought to its original state. However, combining the data collected on April 27, 1994 with a model of the master control board derived from the schematic diagrams and the measured response of the auxiliary electronics, a composite transfer function was derived which does agree with the data on Table 3.1. This transfer function for OH2U is shown in Fig. 3-14 where it is compared to the response measured on

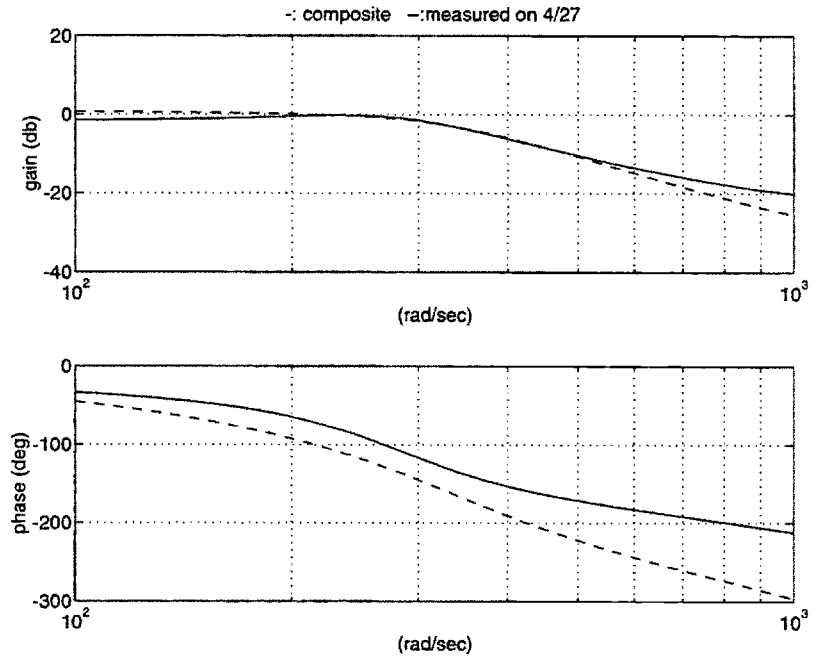

Figure 3-14: OH2U supply transfer function taking into account the proportional gain in the internal control loop.

April 27. The main difference between the two responses is the small amount of proportional gain in the master control board which results in a smaller phase lag. A small amount of proportional gain was, therefore, beneficial, whereas, we saw earlier (Fig. 3-8), that a proportional gain dominated internal feedback loop caused very large oscillations.

3.2.2 The EFC Power Supplies

The EFC coils are the closest to the plasma outboard coils and their only function is to control Z–position on a fast timescale. A chopper system is used to apply voltage to them. The chopper is a pulse–width modulated voltage source converter; it switches the load (EFC coils) between a fixed voltage source (on–intervals) and a nonlinear resistor (off–intervals), thereby applying a reverse voltage to the coils. The length and spacing of these intervals are determined by a demand input signal coming from the PCC. When the demand is zero, the on– and off–pulses are of the same length and the switching happens at the highest frequency (3 kHz). When the demand is nonzero, either the on– or the off–pulse becomes longer, depending on the sign of the demand. The fixed voltage source is a 12–pulse thyristor DC power supply. The nominal rating of the chopper is ± 1000 V and 0 to 3000 A. Since the chopper can only carry current in one direction, the EFC coils normally carry a bias current of 1500 A. This is an inherently nonlinear system and no attempts at modeling it as a linear system were undertaken; instead, experiments similar to the ones conducted to determine the OH2 power supply dynamics were performed for these supplies as well. Frequencies between 20 and 1000 Hz were used. The measured response and a 3–zero/4–pole fitted transfer function are shown in Fig. 3-15. A comparison between Fig. 3-14 and Fig. 3-15 shows that the EFC power supply has a much flatter response than the OH2 power supplies. Its current output is much smaller, so that it cannot be used to correct large perturbations from or change the equilibrium Z–position. This is taken care of mainly by the OH2 coils.

3.2.3 The Other Power Supplies

As discussed in Chapter 1 all coils except the EFC have mainly a shaping function, i.e., they control plasma shape quantities on a timescale which is slow compared

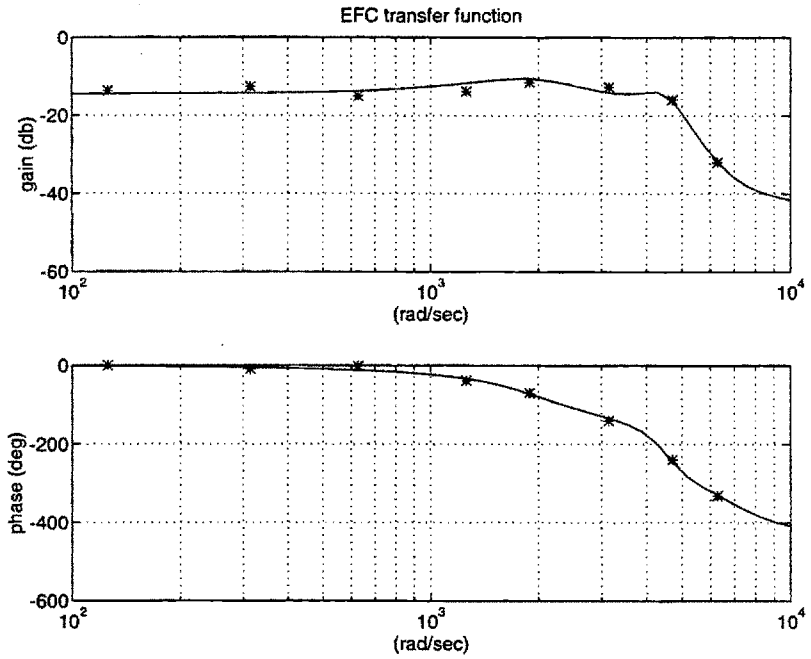

Figure 3-15: Bode plots for the EFC power supply fitted transfer function. The measured points are shown as stars.

to the vertical instability timescale. Special attention was given to the OH2 power supplies above, because they are involved in Z–position control which is linked to the vertical instability; however, they are not really much faster than those of the other shaping coils.

The EF1 coils provide elongation by pulling on the x–points. Since they are independent, the difference in their currents has an influence on the vertical position of the plasma. In fact, they can produce more radial magnetic field at the nominal vacuum vessel center (R = 0.665 m, Z = 0.0 m) per unit current than the OH2 coils. They are fed by two independent 12–pulse thyristor power supplies nominally rated at $\pm$200 V and $\pm$15 kA. Their measured response and a 3–zero/4–pole fitted transfer function are shown in Fig. 3-16. The response is similar to the OH2 power supplies. It would seem that the EF1 coils could qualify to be the primary slow Z–control coils, since, in a static sense, they can produce more radial magnetic field than the OH2 coils and their power supplies have a similar response. The reason

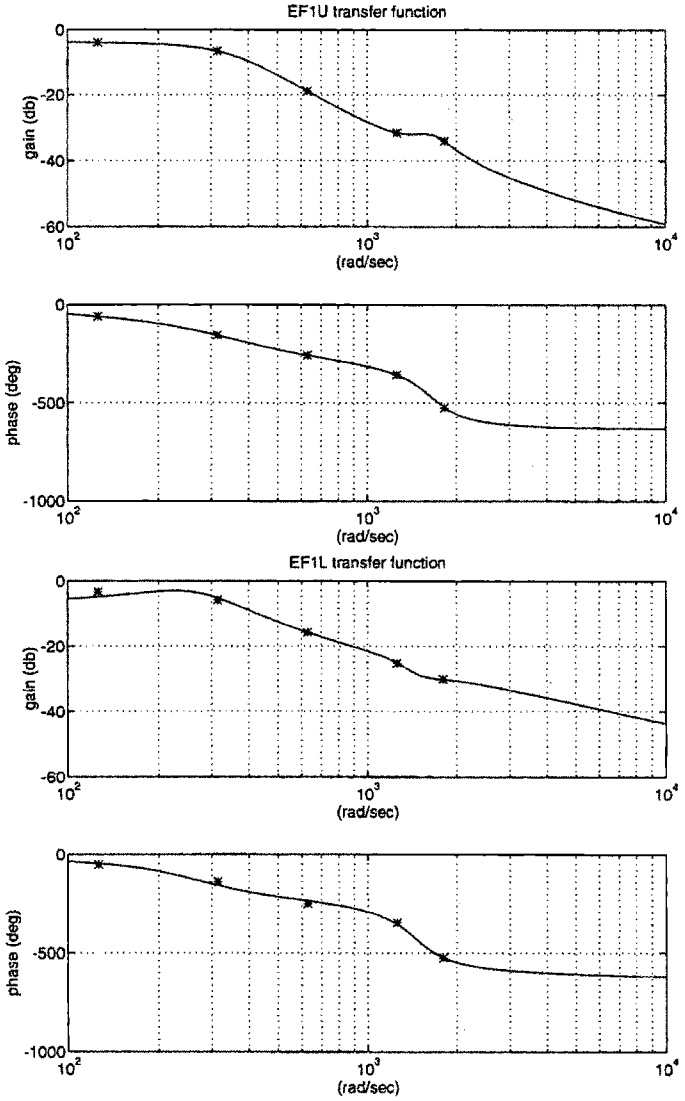

Figure 3-16: Bode plots for EF1U (top) and EF1L (bottom) power supply fitted transfer functions. The measured points are shown as stars.

why this is not the case is that the EF1 coils have more turns than the OH2 coils, so that they have a much larger self–inductance (by approximately a factor of 20) than the OH2 coils. As a result the same voltage applied to the OH2 coils produces a larger dB_R/dt than when applied to the EF1 coils.

The EF2 coils control the horizontal position of the x–points. They are fed by two independent 12–pulse thyristor power supplies nominally rated at 560 V and 0 to 4 kA. Since they are independent, the difference in their currents has an influence on the vertical position of the plasma on a slow timescale. Their measured response and a 3–zero/4–pole (4–zero/5–pole for EF2L) fitted transfer function are shown in Fig. 3-16. The response is slower than that of the OH2 power supplies.

The remaining coils provide perfectly up–down symmetric magnetic field, so that they are not involved in vertical position control. On the day when the power supply characterization tests were conducted, they were given low priority, and there was not time left for them by the end of that run. The OH1 coil controls the plasma current, the EF3 coils are connected in series and provide radial position control, and the EF4 coils, which are also connected in series influence the elongation and triangularity of the plasma. It is assumed that all of these quantities are changed on a timescale which is slow in comparison to the power supply response time, so that neglecting the power supply dynamics is a good approximation.

In this section we have dealt strictly with the frequency domain or transfer function representation of the power supply dynamics. It possible to obtain a state space representation of a system given a transfer function. Since the transfer function formulation does not make any mention of the state, there are several equivalent ways to do this transformation depending on how one defines the state. These methods are described in Ref. [41]. Using these methods, the SISO transfer functions developed in this section were converted into a state space form so they could be used with the other system models.

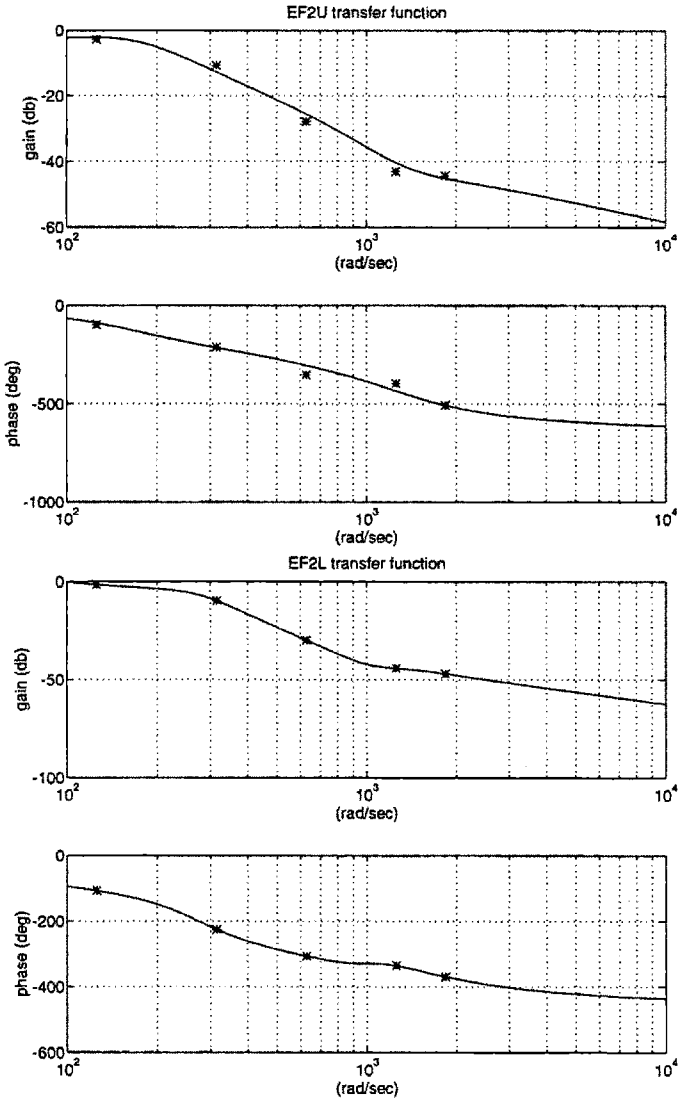

Figure 3-17: Bode plots for EF2U (top) and EF2L (bottom) power supply fitted transfer functions. The measured points are shown as stars.

It should be emphasized that the linear models of power supply dynamics presented in this chapter are in no way a generally valid description of the power supply response. The modulation measurements were performed at one amplitude only. Both the thyristor power supplies and the EFC chopper are very nonlinear devices and, as of yet, we do not have linear models for their response at different amplitudes.

Chapter 4

Model Reduction for Axisymmetric Control

The linear models developed in the previous two chapters have order 200. This means we have to routinely do multiple matrix operations like multiplications and inversions with matrices of this size. This can be very time consuming and may prevent us from doing these calculations repeatedly as needed for design and analysis. In this chapter, we deal with the problem of reducing a complicated electromagnetic passive structure model coupled to a linear plasma response model to a size that allows rapid calculations for the purposes of plasma position and shape control. We find that model reduction through eigenmode decomposition does not reproduce the input-to-output relationship of the system, unless one has a good idea a priori of which eigenmodes are important. Hankel singular mode decomposition, on the other hand, provides an orthogonal basis for the system response, where the modes are ordered by their importance to the input-to-output relationship. The perturbed equilibrium plasma response model is used together with an electromagnetic model of the Alcator C-Mod passive structure to assess the performance of different model reduction schemes. We find that between 10 and 20 modes are required to give an

adequate representation of the passive system. Emphasis is placed on keeping the reduction process independent of the parameters of the plasma we are trying to control.

In past work in the field of tokamak control, the trend has been either to over-simplify or not to simplify at all. In the ISX-B tokamak [42], where the vacuum vessel had two toroidal breaks, the vessel was successfully modeled as a single circuit carrying toroidal current with an m=1 poloidal distribution. In the DIII-D tokamak, it was found both theoretically [12] and experimentally [13] that only one eigenmode of the vacuum vessel response was enough to calculate gains that control the vertical instability. However, this degree of simplification may not be generally attainable and almost certainly will not yield quantitatively accurate predictions of the dynamic behavior. In ASDEX-Upgrade [43], the passive coils inside the vacuum vessel are the main sources of passive stabilization. The vacuum vessel is modeled as a set of 60 toroidal filaments. This model is subjected to eigenmode analysis and only a small number of modes with small numbers of current reversals is kept. By contrast, Hofmann et al., in Refs. [24] and [44], tried to keep their control calculations independent of plasma parameters, and they used the large MHD transport code TSC [18] to simulate plasma time evolution and optimize feedback gains. In TSC, the vacuum vessel is modeled as a set of filaments. No attempt is made to reduce the model.

In this chapter we attempt to reduce a large linear model of a tokamak plasma with a set of axisymmetric conductors around it while minimizing the error in the transfer function and making sure the vertically unstable mode is faithfully reproduced. No attempt is made, however, to deal with the problem of how the effects of noise, disturbances and model errors in the original model are amplified with model reduction.

4.1 Methods of Model Reduction

We employ two methods for the reduction of the standard control problem consisting of the state equation (Eq. 2.41) and the output equation (Eq. 2.42), where the state vector is of size n_x, the output vector is of size n_y and the input vector is of size n_u: eigenmode decomposition and Hankel singular mode (HSM) decomposition. In each of these methods, two transformation matrices, $\mathbf{T}_l$ and $\mathbf{T}_r$ are calculated so that the model reduction can be represented as the transformation:

$$\begin{bmatrix} \mathbf{A} & \mathbf{B} \\ \mathbf{C} & \mathbf{D} \end{bmatrix} \rightarrow \begin{bmatrix} \mathbf{T}_l\mathbf{A}\mathbf{T}_r & \mathbf{T}_l\mathbf{B} \\ \mathbf{C}\mathbf{T}_r & \mathbf{D} \end{bmatrix} \tag{4.1}$$

The transformed model in Eq. 4.1 has the same number of inputs and outputs as the original system but a smaller number of internal states.

The simplest approach to model reduction is via eigenmode decomposition. The left and right eigenvectors of $\mathbf{A}$, $\vec{w}_i$ and $\vec{v}_i$, and its eigenvalues λ_i for $i = 1, ..., n_x$ satisfy the equation

$$\mathbf{A} = \mathbf{V}\mathbf{\Lambda}\mathbf{W} \tag{4.2}$$

where $\mathbf{V}$ is a matrix with $\vec{v}_i$'s as its columns, $\mathbf{W}$ is a matrix with $\vec{w}_i^H$'s (superscript H stands for Hermitian conjugate) as its rows, $\mathbf{\Lambda} = diag(\lambda_1, \lambda_2, ..., \lambda_{n_x})$, and $\mathbf{W} = \mathbf{V}^{-1}$. If we consider certain modes to be more important than others (one could favor unstable and slowly damped modes over fast damped modes for example), $\mathbf{T}_l$ would have as rows the $\vec{w}_i^H$'s corresponding to the important modes, and $\mathbf{T}_r$ would have as columns their $\vec{v}_i$'s.

The concept of singular values of a matrix has been used very successfully in all areas of control theory lately, and one might expect it to appear here as well. Note, however, that, for a real symmetric matrix, the singular values are equal to the eigenvalues. $\mathbf{M}$ is a symmetric matrix and the plasma response is usually only a perturbation from this symmetry. Discarding small singular value modes is, therefore, equivalent to discarding the slow eigenmodes.

As opposed to the above method, which is concerned with the properties of the response matrix $\mathbf{A}$ alone, model reduction in terms of Hankel singular values focuses on the input-to-output behavior of the complete system described by Eqs. 2.41 and 2.42. The solution to these equations is:

$$\vec{y}(t) = \mathbf{C}\exp\left[\mathbf{A}(t-t_0)\right]\vec{x}(t=t_0) + \int_{t_0}^{t} \mathbf{C}\exp\left[\mathbf{A}(t-\tau)\right]\mathbf{B}\vec{u}(\tau)d\tau + \mathbf{D}\vec{u}(t) \quad (4.3)$$

We define the controllability grammian as:

$$\mathbf{P} \equiv \int_0^{\Delta t} \exp(\mathbf{A}t)\mathbf{B}\mathbf{B}^H \exp(\mathbf{A}^H t)dt \quad (4.4)$$

and the observability grammian as:

$$\mathbf{Q} \equiv \int_0^{\Delta t} \exp(\mathbf{A}^H t)\mathbf{C}^H\mathbf{C}\exp(\mathbf{A}t)dt \quad (4.5)$$

From the formulation of the formal solution in Eq. 4.3 one can show [41], that, when $\mathbf{P}$ is non-singular, it is possible to go from any initial state to any final state in a finite time interval Δt using the inputs $\vec{u}$. Also, when $\mathbf{Q}$ is non-singular, it is possible to determine $\vec{x}(t)$ by using the measurements $\vec{y}$ over a finite interval Δt after t. As $\Delta t \to \infty$, $\mathbf{P}$ and $\mathbf{Q}$ satisfy the Lyapunov equations [41]:

$$\mathbf{A}\mathbf{P} + \mathbf{P}\mathbf{A}^H + \mathbf{B}\mathbf{B}^H = \mathbf{0} \quad (4.6)$$

$$\mathbf{A}^H\mathbf{Q} + \mathbf{Q}\mathbf{A} + \mathbf{C}^H\mathbf{C} = \mathbf{0} \quad (4.7)$$

The Hankel singular values (HSV's) of the system $[\mathbf{A},\mathbf{B},\mathbf{C},\mathbf{D}]$ are defined as:

$$\sigma_{Hi}([\mathbf{A},\mathbf{B},\mathbf{C},\mathbf{D}]) \equiv \sqrt{\lambda_i(\mathbf{P}\mathbf{Q})} \quad (4.8)$$

where $\lambda_i(\mathbf{P}\mathbf{Q})$ is the i'th eigenvalue of $\mathbf{P}\mathbf{Q}$. The HSV's are the singular values of the mapping from past inputs to future outputs (see appendix).

It is worthwhile to note that HSV's, as well as eigenvalues, are invariant under state space transformation, which is a necessary property for an input-to-output

figure of merit. If we define a new state space $\vec{z} \equiv \mathbf{T}\vec{x}$, where $\mathbf{T}$ is non-singular, the new state equation is

$$\dot{\vec{z}} = \mathbf{TAT}^{-1}\vec{z} + \mathbf{TB}\vec{u}$$

and the output equation becomes

$$\vec{y} = \mathbf{CT}^{-1}\vec{z} + \mathbf{D}\vec{u}$$

while the controllability and observability grammians, $\mathbf{P}$ and $\mathbf{Q}$, become $\hat{\mathbf{P}} = \mathbf{TPT}^H$ and $\hat{\mathbf{Q}} = (\mathbf{T}^H)^{-1}\mathbf{QT}^{-1}$ respectively and their product becomes $\mathbf{TPQT}^{-1}$, thereby yielding the same eigenvalues and HSV's as $\mathbf{PQ}$.

Furthermore, $\mathbf{P}$ and $\mathbf{Q}$ are both real symmetric matrices, so that there exists a real matrix $\mathbf{R}$ such that $\mathbf{Q} = \mathbf{R}^H\mathbf{R}$ and $\mathbf{RPR}^H = \mathbf{U}^H\mathbf{\Sigma}^2\mathbf{U}$ where $\mathbf{U}$ is a unitary matrix and $\mathbf{\Sigma} = diag(\sigma_{H1}, \sigma_{H2}, ..., \sigma_{Hn_x})$. If we choose $\mathbf{T} \equiv \mathbf{T}_{BAL} = -\mathbf{\Sigma}^{-1/2}\mathbf{U}^H\mathbf{R}$, we get $\hat{\mathbf{P}} = \hat{\mathbf{Q}} = \mathbf{\Sigma}$. This is known as a balancing transformation. If we partition the transformed matrices,

$$\begin{bmatrix} \hat{\mathbf{A}} & \hat{\mathbf{B}} \\ \hat{\mathbf{C}} & \hat{\mathbf{D}} \end{bmatrix} \equiv \begin{bmatrix} \mathbf{T}_{BAL}\mathbf{A}\mathbf{T}_{BAL}^{-1} & \mathbf{T}_{BAL}\mathbf{B} \\ \mathbf{C}\mathbf{T}_{BAL}^{-1} & \mathbf{D} \end{bmatrix} = \begin{bmatrix} \mathbf{A}_{11} & \mathbf{A}_{12} & \mathbf{B}_1 \\ \mathbf{A}_{21} & \mathbf{A}_{22} & \mathbf{B}_2 \\ \mathbf{C}_1 & \mathbf{C}_2 & \mathbf{D} \end{bmatrix}$$

where the subscript 1 refers to the largest k HSV's and the subscript 2 refers to the smallest $n_x - k$ HSV's, we get a reduced system $[\mathbf{A}_{11}, \mathbf{B}_1, \mathbf{C}_1, \mathbf{D}]$. This method of model reduction was proposed by Moore [46]. Glover [45] showed that the frequency domain transfer function matrix of this reduced system , $\hat{\mathbf{G}}(i\omega) \equiv \hat{\mathbf{C}}(i\omega\mathbf{I} - \hat{\mathbf{A}})^{-1}\hat{\mathbf{B}} + \hat{\mathbf{D}}$, differs from the transfer function matrix of the full system, $\mathbf{G}(i\omega) \equiv \mathbf{C}(i\omega\mathbf{I} - \mathbf{A})^{-1}\mathbf{B} + \mathbf{D}$, by the following maximum error:

$$\|(\mathbf{G}(i\omega) - \hat{\mathbf{G}}(i\omega)\|_\infty \leq 2 \sum_{i=k+1}^{n_x} \sigma_{Hi} \tag{4.9}$$

where the infinity norm signifies the largest singular value of a matrix.

$\mathbf{T}_{BAL}$ is not necessarily an orthogonal matrix, and the above balancing transformation can be badly conditioned when the system is nearly unobservable or

uncontrollable, i.e., $\mathbf{P}$ or $\mathbf{Q}$ are close to singular. Safonov and Chiang [47] proposed the following set of transformation matrices that yield exactly the same $\hat{\mathbf{G}}(i\omega)$ as the truncation of the above balanced realization of the full model: For every real matrix with real eigenvalues, such as $\mathbf{PQ}$, there is a real orthogonal matrix $\mathbf{V}$ such that $\mathbf{V}^T\mathbf{PQV}$ is an upper triangular matrix with the diagonal consisting of the eigenvalues of $\mathbf{PQ}$ — see Golub and van Loan [36] — which is known as the Schur form of $\mathbf{PQ}$. Two Schur forms of $\mathbf{PQ}$ in which its eigenvalues appear on the diagonal in ascending or descending order can be realized using orthogonal, real transformations $\mathbf{V}_A = [\mathbf{V}_{A2} \mid \mathbf{V}_{A1}]$ and $\mathbf{V}_D = [\mathbf{V}_{D1} \mid \mathbf{V}_{D2}]$ respectively, where, again, the subscript 1 refers to the largest k HSV's and the subscript 2 refers to the smallest $n_x - k$ HSV's. Note, that $\mathbf{V}_A$ and $\mathbf{V}_D$ are orthogonal eigenspaces of $\mathbf{PQ}$. Next, a new matrix, $\mathbf{E}$, is formed and decomposed according to its singular values:

$$\mathbf{E} \equiv \mathbf{V}_{A1}^T\mathbf{V}_{D1} \equiv \mathbf{U}_E\mathbf{\Sigma}_E\mathbf{V}_E^T$$

It can be shown [47] that the transformation matrices

$$\mathbf{T}_l = \mathbf{\Sigma}_E^{-1/2}\mathbf{U}_E^T\mathbf{V}_{A1}^T$$

$$\mathbf{T}_r = \mathbf{V}_{D1}\mathbf{V}_E\mathbf{\Sigma}_E^{-1/2}$$

produce the same reduced-model transfer function matrix as Moore's [46] balance-and-truncate approach. What has been gained by opting for these not so intuitive $\mathbf{T}_l$ and $\mathbf{T}_r$ is an algorithm which works even if the full system is close to unobservable or uncontrollable. This is the technique we use here, in the form of a MATLAB application [48].

4.2 Partitioning the Model

As we saw in Section 2.4, one can transform Eqs. 2.2 and 2.43 into state and output equations as in Eqs. 2.41 and 2.42. One can then use the model reduction methods

mentioned above. We have to go through the computationally tedious process of model reduction, however, for each equilibrium we wish to investigate, because the plasma response matrix, $\mathbf{X}$, depends on the equilibrium. We should like to have a reduced model of the vacuum vessel/structure without a plasma so that model reduction would only have to be carried out once. We want to keep the active coils complete in our reduced model but reduce the total size to manageable proportions.

In general, the passive system consists of approximately nested sets of conductors. The set closest to the plasma is generally a representation of the vacuum vessel. Further out, will be the mechanical structure. As we shall show, it can be advantageous to partition the model and treat the "vacuum vessel" and "structure" separately. This partitioning can be done intuitively for the examples we discuss. In what follows, we use the subscript "v" to refer to the vacuum vessel, "s" to refer to the steel structure around the vacuum vessel, "c" to refer to the active coils,"g" to refer to either vacuum vessel or structure elements for unpartitioned ("composite") models, and"r" to refer to the reduced space.

If we consider a composite model, keeping the vacuum vessel and the structure together, we can write the circuit equation for the vacuum vessel/structure without a plasma as in Eq. 3.1, and rewrite this in state equation form as

$$\dot{\vec{I}}_g = -\mathbf{M}_{gg}^{-1}\mathbf{R}_{gg}\vec{I}_g - \mathbf{M}_{gg}^{-1}\mathbf{M}_{gc}\dot{\vec{I}}_c$$

which, together with an appropriate output equation, lends itself to any of the order reduction schemes mentioned earlier, resulting in the two transformation matrices, $\mathbf{T}_l$ and $\mathbf{T}_r$. This reduction can then be applied to the full model including the plasma response. Then, an approximate reduced model is:

$$\begin{bmatrix} \mathbf{T}_l(\mathbf{M}_{gg}+\mathbf{X}_{gg})\mathbf{T}_r & \mathbf{T}_l(\mathbf{M}_{gc}+\mathbf{X}_{gc}) \\ (\mathbf{M}_{cg}+\mathbf{X}_{cg})\mathbf{T}_r & (\mathbf{M}_{cc}+\mathbf{X}_{cc}) \end{bmatrix} \begin{bmatrix} \dot{\vec{I}}_{gr} \\ \dot{\vec{I}}_c \end{bmatrix} + \\ + \begin{bmatrix} \mathbf{T}_l\mathbf{R}_g\mathbf{T}_r & \mathbf{0} \\ \mathbf{0} & \mathbf{R}_{cc} \end{bmatrix} \begin{bmatrix} \vec{I}_{gr} \\ \vec{I}_c \end{bmatrix} = \begin{bmatrix} \vec{0} \\ \vec{V}_c \end{bmatrix} \tag{4.10}$$

When we use a composite model of the vacuum vessel and the structure, it is possible that the order reduction process will keep some irrelevant modes of one and neglect important modes of the other, thereby forcing us to keep more modes than necessary to get a good reduced model. This is the case, for example, when one tries to reduce the model of the vacuum vessel and the structure for Alcator C–Mod by eigenmode decomposition. The structure elements are thick pieces of conductor and give rise to a large number of slowly damped modes (large L/R time) so that, if we choose to keep only the slow modes, we almost end up neglecting the vacuum vessel altogether. A better approach is to reduce the vacuum vessel and the structure models separately and then add the coil and plasma response. We can write one circuit equation for the vacuum vessel without plasma,

$$\mathbf{M}_{vv}\dot{\vec{I}}_v + \mathbf{M}_{vs}\dot{\vec{I}}_s + \mathbf{M}_{vc}\dot{\vec{I}}_c + \mathbf{R}_{vv}\vec{I}_v = \mathbf{0}, \tag{4.11}$$

and one for the structure,

$$\mathbf{M}_{ss}\dot{\vec{I}}_s + \mathbf{M}_{sv}\dot{\vec{I}}_v + \mathbf{M}_{sc}\dot{\vec{I}}_c + \mathbf{R}_{ss}\vec{I}_s = \mathbf{0}, \tag{4.12}$$

and then we can reduce the order of each one of these as we did above for Eq. 3.1 to obtain transformation matrices $\mathbf{T}_{vl}$ and $\mathbf{T}_{vr}$ for the vacuum vessel and $\mathbf{T}_{sl}$ and $\mathbf{T}_{sr}$ for the structure. Adding the plasma response, we get the following approximate reduced system:

$$\begin{bmatrix} \mathbf{M}_{11} & \mathbf{M}_{12} & \mathbf{M}_{13} \\ \mathbf{M}_{21} & \mathbf{M}_{22} & \mathbf{M}_{23} \\ \mathbf{M}_{31} & \mathbf{M}_{32} & \mathbf{M}_{33} \end{bmatrix} \begin{bmatrix} \dot{\vec{I}}_{vr} \\ \dot{\vec{I}}_{sr} \\ \dot{\vec{I}}_c \end{bmatrix} + \begin{bmatrix} \mathbf{R}_{11} & \mathbf{0} & \mathbf{0} \\ \mathbf{0} & \mathbf{R}_{22} & \mathbf{0} \\ \mathbf{0} & \mathbf{0} & \mathbf{R}_{33} \end{bmatrix} \begin{bmatrix} \vec{I}_{vr} \\ \vec{I}_{sr} \\ \vec{I}_c \end{bmatrix} = \begin{bmatrix} \vec{0} \\ \vec{0} \\ \vec{V}_c \end{bmatrix} \tag{4.13}$$

where

$$\mathbf{M}_{11} \equiv \mathbf{T}_{vl}(\mathbf{M}_{vv} + \mathbf{X}_{vv})\mathbf{T}_{vr}$$

$$\mathbf{M}_{12} \equiv \mathbf{T}_{vl}(\mathbf{M}_{vs} + \mathbf{X}_{vs})\mathbf{T}_{sr}$$

$$\mathbf{M}_{13} \equiv \mathbf{T}_{vl}(\mathbf{M}_{vc} + \mathbf{X}_{vc})$$

$$\mathbf{M}_{21} \equiv \mathbf{T}_{sl}(\mathbf{M}_{sv} + \mathbf{X}_{sv})\mathbf{T}_{vr}$$

$$\mathbf{M}_{22} \equiv \mathbf{T}_{sl}(\mathbf{M}_{ss} + \mathbf{X}_{ss})\mathbf{T}_{sr}$$

$$\mathbf{M}_{23} \equiv \mathbf{T}_{sl}(\mathbf{M}_{sc} + \mathbf{X}_{sc})$$

$$\mathbf{M}_{31} \equiv (\mathbf{M}_{cv} + \mathbf{X}_{cv})\mathbf{T}_{vr}$$

$$\mathbf{M}_{32} \equiv (\mathbf{M}_{cs} + \mathbf{X}_{cs})\mathbf{T}_{sr}$$

$$\mathbf{M}_{33} \equiv (\mathbf{M}_{cc} + \mathbf{X}_{cc})$$

$$\mathbf{R}_{11} \equiv \mathbf{T}_{vl}\mathbf{R}_{vv}\mathbf{T}_{vr}$$

$$\mathbf{R}_{22} \equiv \mathbf{T}_{sl}\mathbf{R}_{ss}\mathbf{T}_{sr}$$

$$\mathbf{R}_{33} \equiv \mathbf{R}_{cc}$$

These reduction schemes are not expected to work as well as the reduction of the combined plasma/coils/vessel/structure system. One thing we can do to improve their performance in capturing some of the plasma behavior is to include the response of a generic plasma in the reduction of the composite or the separate vessel/structure system. This would amount to adding to all M-matrices in Eqs. 3.1, 4.11, and 4.12 the corresponding **X**-matrices for the generic plasma.

4.3 Results

We represent the Alcator C–Mod vacuum vessel by 94 elements and the structure by 96 elements as shown in Fig. 3-1.

As an example to test the techniques described in the previous section we choose a typical expected high performance Alcator C–Mod plasma. A different slightly more elongated equilibrium was chosen as the generic plasma. Parameters describing these equilibria are shown in Table 4.1.

Quantity	example	generic	units
plasma current	3.01	3.01	MA
radial magnetic axis location	67.5	67.9	cm
vertical magnetic axis location	0.00	2.00	cm
minor radius	21.1	21.3	cm
elongation of 95% flux surface	1.58	1.70	
elongation of separatrix	1.69	1.85	
triangularity of 95% flux surface	.271	.379	
safety factor on axis	1.01	.973	
safety factor on 95% flux surface	2.08	2.53	
internal inductance	.680	.705	
β_p	.197	.101	

Table 4.1: Essential characteristics of the example and generic equilibria used in this section.

Two figures of merit were chosen for the performance of the different model reduction techniques:

- How well the vertical instability mode eigenvalue of the full model is reproduced.
- The relative maximum error in the transfer function matrix as a function of frequency defined by:

$$\epsilon_r(\omega) \equiv \frac{\|\mathbf{G}(i\omega) - \hat{\mathbf{G}}(i\omega)\|_\infty}{\|\mathbf{G}(i\omega)\|_\infty}$$

Fig. 4-1 shows $\epsilon_r(\omega)$ for a reduction of the combined plasma/coils/vessel/structure model by eigenmode and HSM decomposition. The full model is of length 200 (190 vessel/structure elements and 10 coils) and includes the response of a typical Alcator C–Mod plasma. The model reduced by eigenmode decomposition is of length 40. The two models reduced by Hankel singular mode decomposition are of length 10 and 40. Note how badly eigenmode reduction keeping the unstable and the 39 slowest modes reproduces the input-to-output relationship. Reduction to the same number of modes by HSM gives errors that are smaller by several orders of mag-

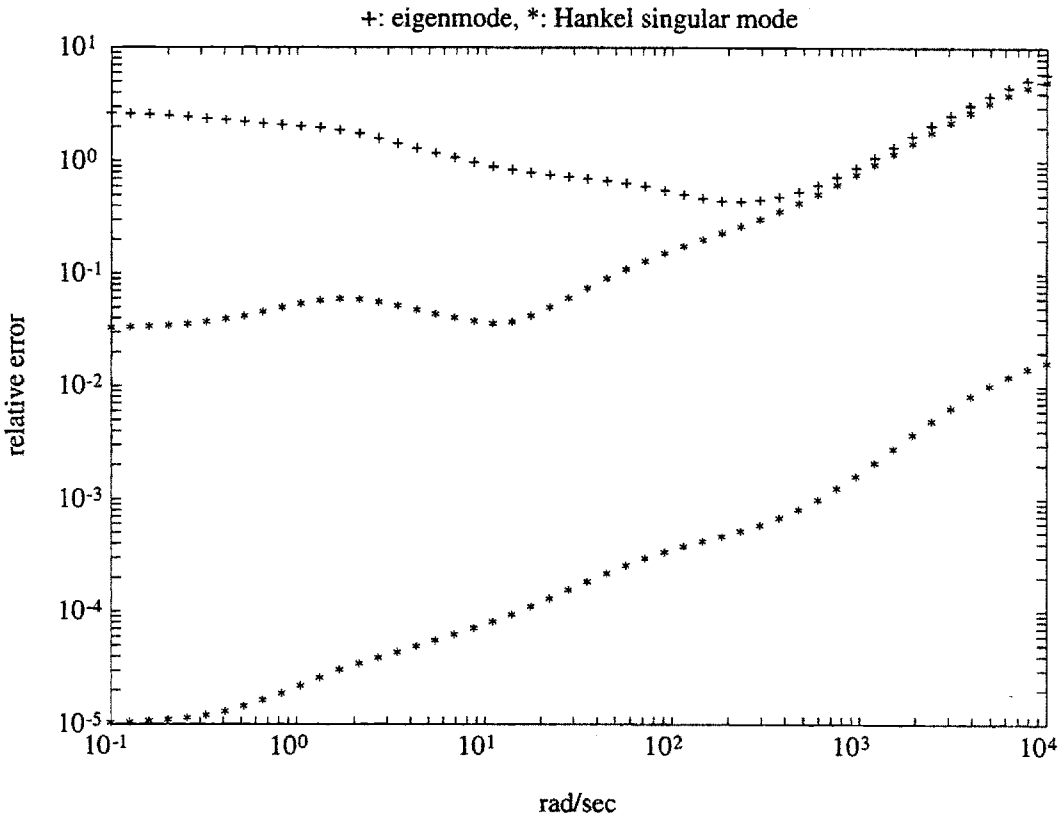

Figure 4-1: $\epsilon_r(\omega)$ for two different model reduction methods. The two models reduced by Hankel singular mode decomposition are of length 10 (upper) and 40 (lower). The unstable mode eigenvalue is reproduced exactly in all cases.

nitude. With eigenmode decomposition, we have no guidance as to which modes influence the outputs. It is obviously not just the slowest modes in this case.

The range of ω's used in these figures represents the range of eigenvalues of the full system. It should be noted, however, that modes with decay rates higher than $10^3 sec^{-1}$ are unimportant and result in very small absolute values of $\|\mathbf{G}(i\omega)\|_\infty$. In other words, any such fast excitation of the coils will not be observed at the magnetic diagnostics, since it will not have a chance to soak through the vacuum vessel. Because of the definition of the relative error, high values of $\epsilon_r(\omega)$ in this ω-range does not necessarily mean poor performance of the model reduction scheme. Also, from a control point of view, anything that exceeds the bandwidth of the magnetic diagnostics and the response time of the power supplies feeding the coils is unimportant. In Alcator C–Mod, we do not hope to control anything changing at a rate faster than $10^3 sec^{-1}$ due to power supply limitations.

Fig. 4-2 shows $\epsilon_r(\omega)$ for eigenmode reduction where the plasma and coil response were reduced by acting on them with the transformation matrices calculated when reducing the composite (upper plot) or the separate (lower plot) vessel/structure model as described in section 4.2. In the first plot, the 190-element vessel/structure model was reduced to seven different sizes ranging from 5 to 60. In the second plot, the 94-element vacuum vessel model was reduced to six different sizes ranging from 5 to 50 and the 96-element structure model was reduced to size 10. The coil and plasma response were added afterwards. Note how using more modes in the first case does not noticeably decrease the error. We observe that in this case, no unstable mode appears. This is because the (slow) modes we have kept are due to the structure, and the vacuum vessel has effectively been ignored. Consequently, the plasma becomes vertically unstable on the ideal MHD timescale. Our massless plasma assumption cannot handle such instabilities with growth rates of the order of the Alfvén frequency. As the plasma becomes more and more unstable, the unstable mode growth rate increases and, somewhere in the $10^4 sec^{-1}$

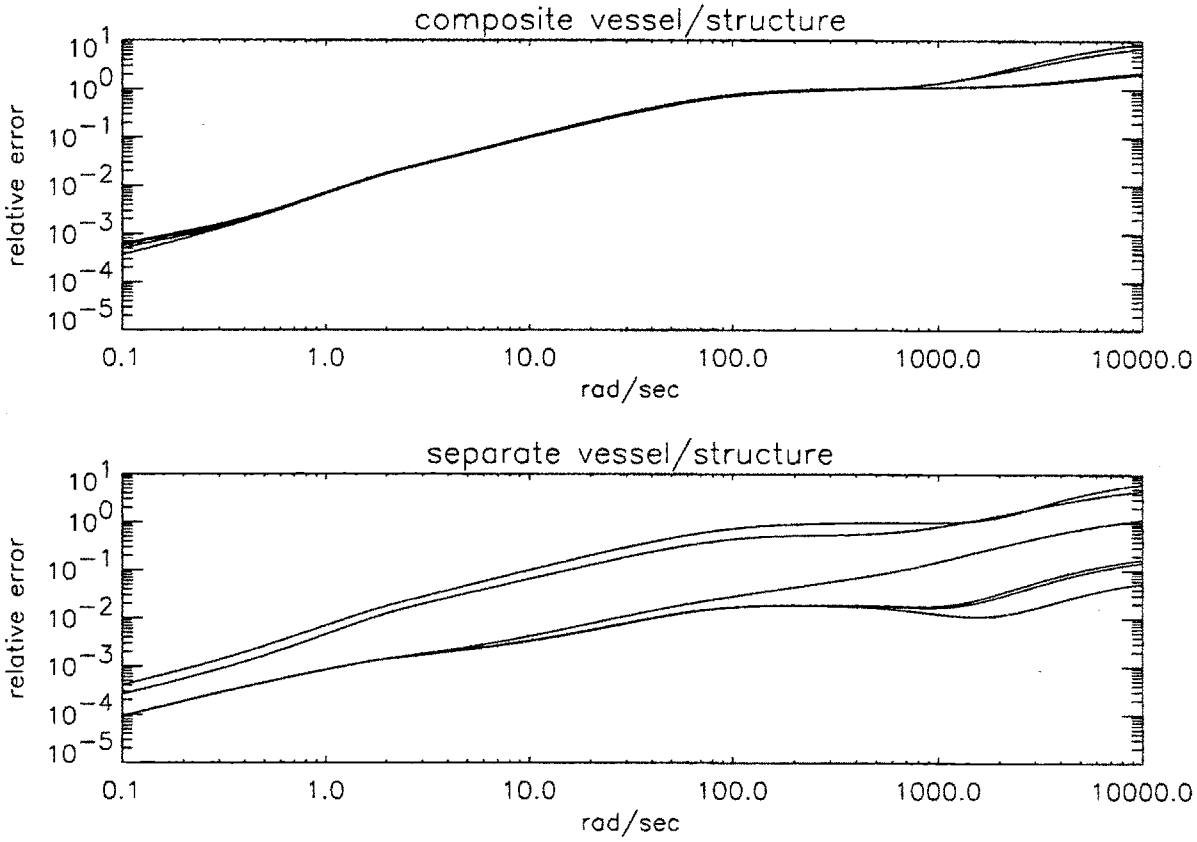

Figure 4-2: $\epsilon_r(\omega)$ for eigenmode decomposition.

area, disappears since the massless plasma model cannot describe modes with such growth rates. If the number of modes kept increases significantly, sufficient vessel modes will be kept, that the vertical instability will return and errors will start going down, approaching zero as the number of passive modes kept approaches 190. It is remarkable, though, that this does not happen before we reach 50 modes. When we split the vessel from the structure, thereby making sure that some modes due to the vessel are included, we are able both, to reduce the error by keeping more vessel modes, and to reproduce the unstable mode.

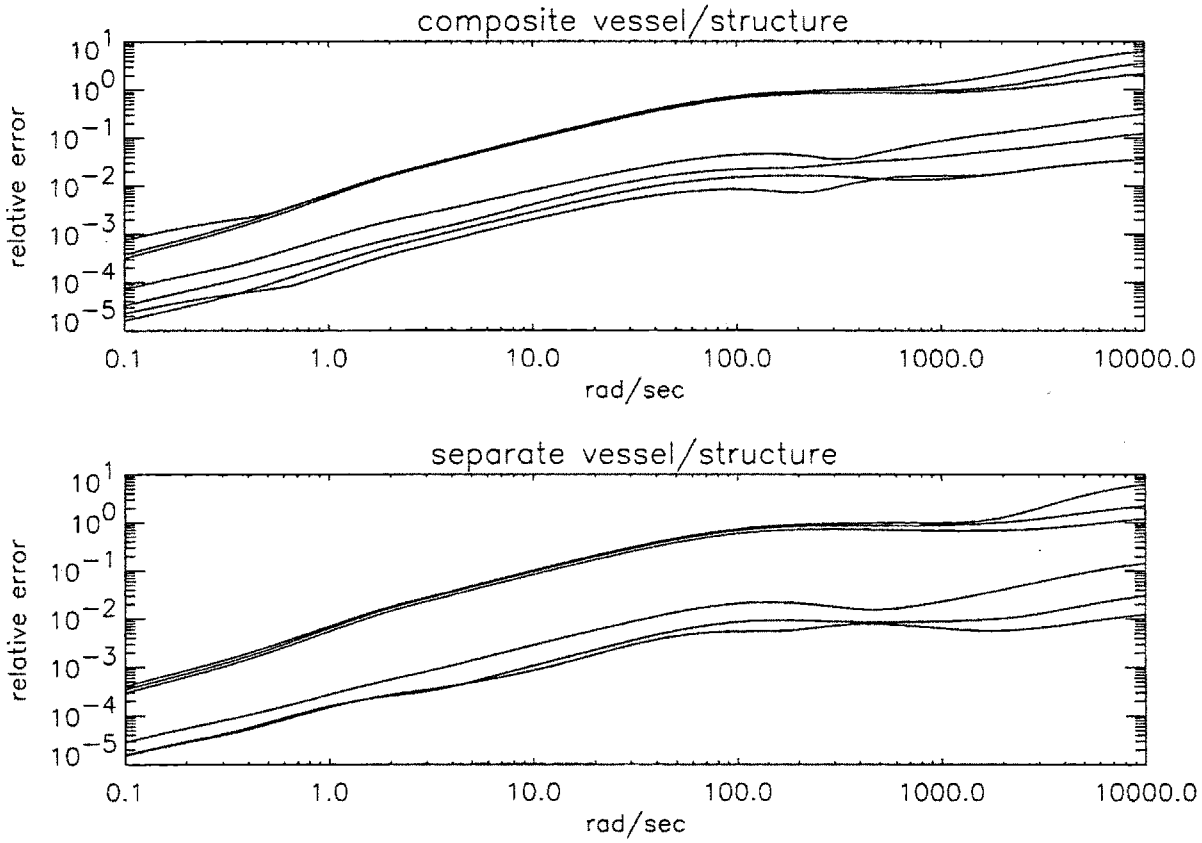

Figure 4-3: $\epsilon_r(\omega)$ for Hankel singular mode decomposition.

Fig. 4-3 shows the same for HSM reduction. In the first plot, the 190-element vessel/structure model was reduced to seven different sizes ranging from 5 to 60. In the second plot, the 96-element vacuum vessel model was reduced to six different

sizes ranging from 5 to 50 and the 94-element structure model were reduced to size 10. The coil and plasma response were added afterwards. Together with Eq. 3.1 and Eqns. 4.11 and 4.12, the parts of Eq. 2.43 relating the currents in the respective passive elements to the magnetic diagnostic signals were used as output equations. This proved to give better results than using an identity as output equation, i.e., using the state vector as output vector. Note how the error is reduced in the composite vessel/structure case (upper plot) when the number of modes kept is increased. An unstable eigenmode is reproduced, provided we keep at least 20 vessel/structure modes.

We see that $\epsilon_r(\omega)$ curves for different number of modes kept do not intersect, so we abbreviate the presentation of results hereafter by considering only one frequency.

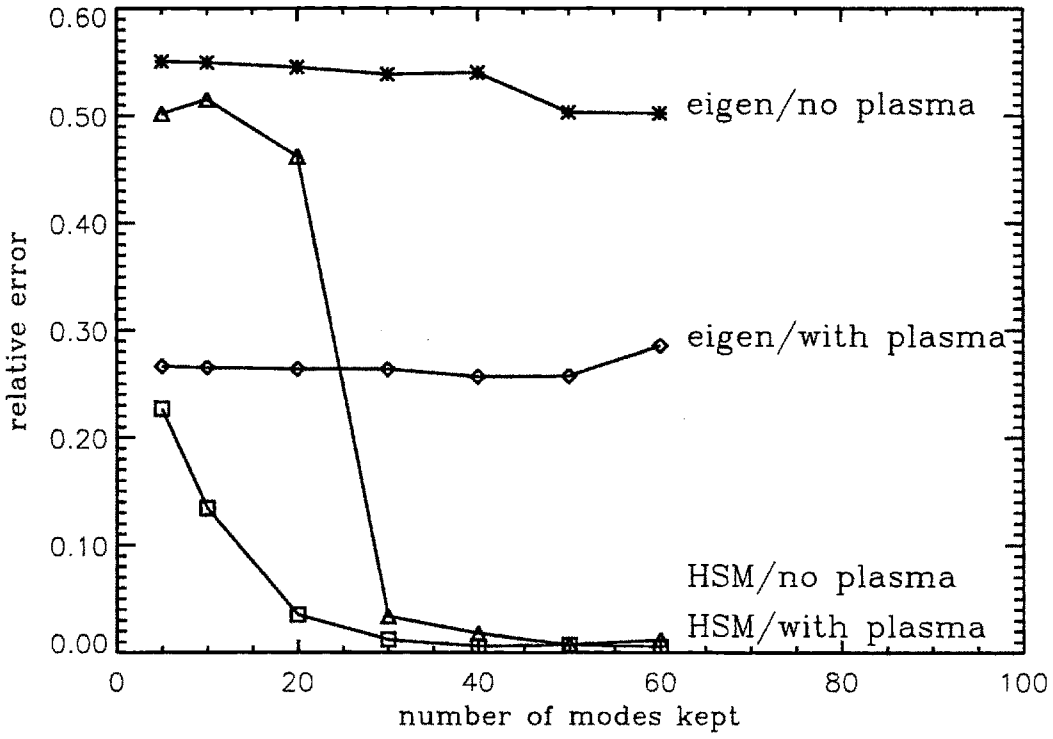

Figure 4-4: ϵ_r at 10 Hz as a function of number of modes kept for eigenmode (eigen) and Hankel singular mode (HSM) reduction of the composite vessel/structure system with and without a generic plasma.

Fig. 4-4 once more shows how the error in eigenmode reduction stays unaffected as the number of modes kept is increased for the composite vessel/structure system. In contrast, HSM reduction shows a decrease in error if more than 20 modes are kept. In both cases, the reduction with a generic plasma response yields smaller error for the same number of modes kept.

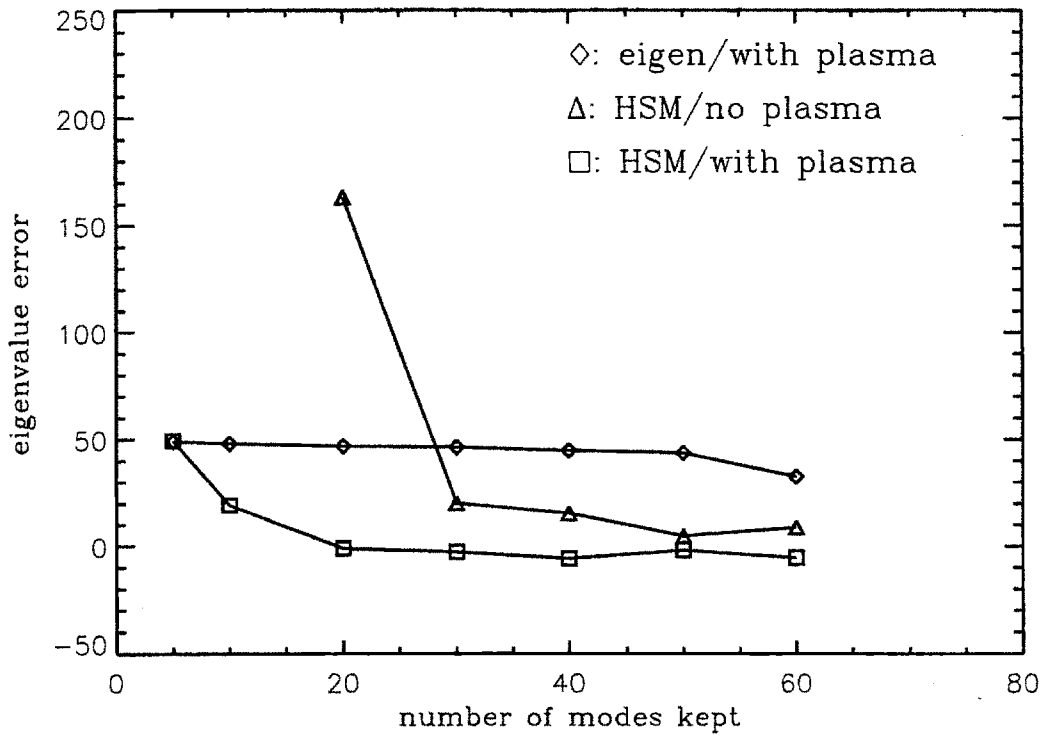

Figure 4-5: Difference between reduced model and full model unstable eigenvalue (279.1 rad/sec) as a function of number of modes kept for eigenmode (eigen) and Hankel singular mode (HSM) reduction of the composite vessel/structure system with and without a generic plasma.

Fig. 4-5 shows the difference in unstable eigenvalue between reduced and full models for composite vessel/structure reduction. Note that none of the reduced models obtained with eigenmode reduction but without a generic plasma response give an unstable mode. The same holds for the first two models obtained by HSM reduction without a generic plasma.

Figures 4-6 and 4-7 show ϵ_r and unstable eigenvalue error for the reduction

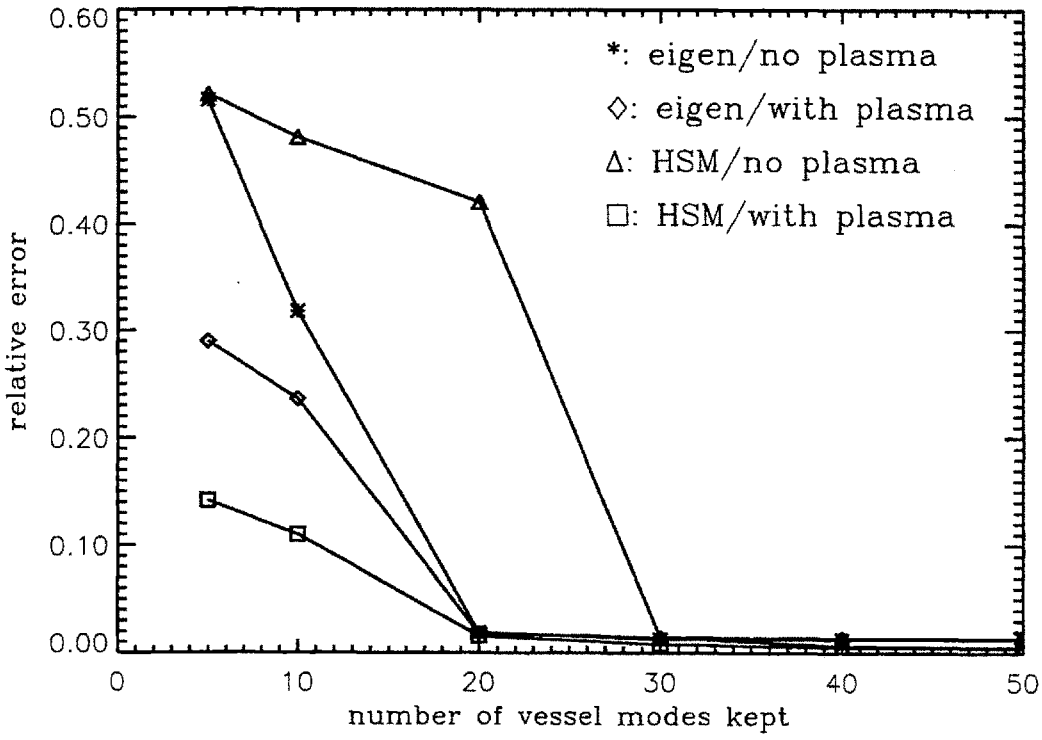

Figure 4-6: ϵ_r at 10 Hz as a function of number of vessel modes kept in addition to 10 structure modes for eigenmode (eigen) and Hankel singular mode (HSM) reduction of the separate 96-element vessel/ 94-element structure with and without a generic plasma.

of the *separate* vessel/structure model by eigenmode and HSM decomposition with and without the generic plasma response. Note how eigenmode and HSM reduction perform comparably. Also note how the error decreases if we keep more than 10 vessel modes (20 vessel/structure modes total). The generic plasma helps in both cases, but it does not help as much in the eigenmode reduction as in the HSM reduction.

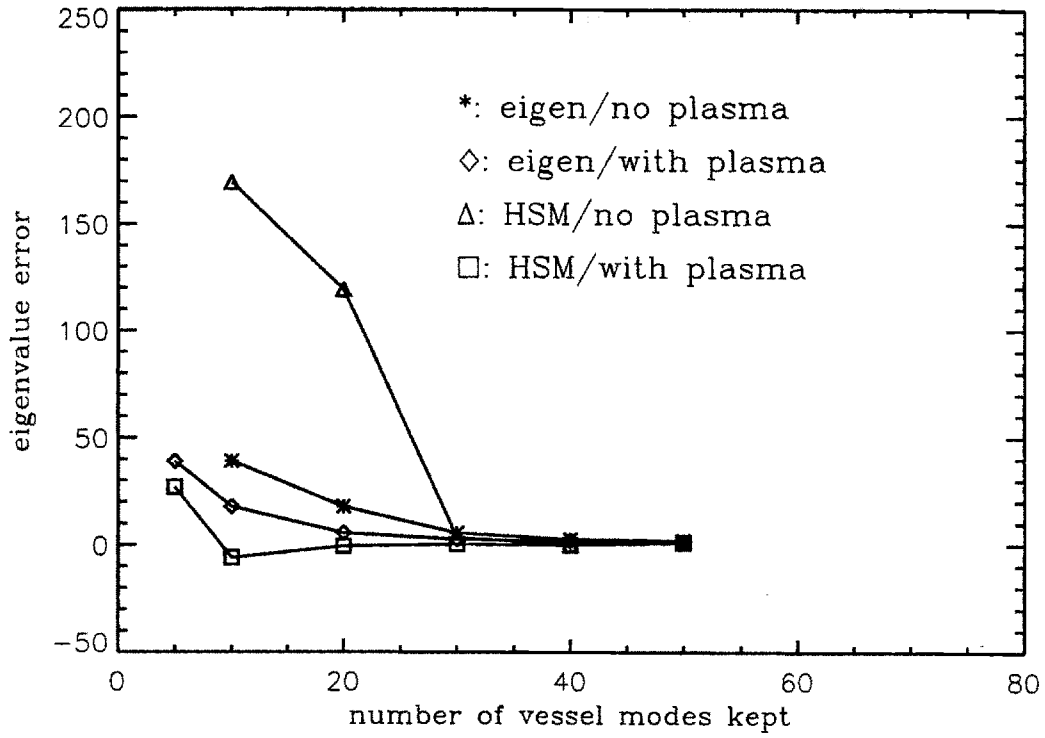

Figure 4-7: Difference between reduced model and full model unstable eigenvalue (279.1 rad/sec) as a function of number of vessel modes kept in addition to 10 structure modes for eigenmode (eigen) and Hankel singular mode (HSM) reduction of the separate 96-element vessel/ 94-element structure with and without a generic plasma.

We have seen in this chapter that, in a tokamak with such complicated vacuum vessel and conducting superstructure as Alcator C-Mod, more than just a few passive modes have to be taken into account. Keeping the slowest eigenmodes erroneously lead one to neglect the vacuum vessel altogether. Only by resorting to

a splitting of the vacuum vessel and the structure into two models, and keeping the slowest modes of each gave a reduced model with reasonable error. The reduction based on Hankel singular modes on the other side performs comparably with either the composite or the partitioned models. Transformation matrices for the model reductions are calculated once either without a plasma or with a generic plasma and then applied to the plasma response matrix of each particular case. The inclusion of a generic plasma was beneficial. In the results presented in Chapter 6 a reduced model with 30 modes for the vacuum vessel and 10 modes for the structure was used. The reduction was performed via HSM decomposition and the generic plasma used in the examples in this chapter was included.

Chapter 5

Comparison to Experiment Part I: Open Loop

This chapter presents analysis of experiments which were performed on Alcator C–Mod during the Fall of 1993 for the purpose of testing the validity of the linear plasma response models presented in Chapter 2. Even though the idea behind these experiments is simple – turn off the feedback and observe plasma behavior –, they had not, to the author's knowledge, been performed on another tokamak with elongated plasmas previously, mainly because of the associated danger of disruptions.

5.1 Equilibrium Reconstruction

In order to form the linear plasma response model, we need to define the operating point about which we consider the plasma to be perturbed. We consider a time well into the so–called "flattop" part of the discharge, when the total plasma current is constant, the plasma has been shaped and the large amounts of eddy currents induced in the vacuum vessel and superstructure at the beginning of the discharge have largely decayed away. Then, we can use the different measurements

to reconstruct the state of the plasma at some instant in time in the form of an equilibrium that satisfies the Grad–Shafranov equation and does not contradict any of the measurements. We present in this section two ways to do this: one of them, in the form of the code EFIT, uses only the data at the time of interest in a fitting procedure, while the other, based on the circuit equation relies on the history of the data from the beginning of the discharge until the time of interest.

5.1.1 Reconstruction Using EFIT

In recent years, the EFIT code [49] has been used at several research centers as a reliable and efficient method to reconstruct the plasma current profile parameters in tokamaks, as well as the plasma shape and a flux surface geometry consistent with the Grad–Shafranov equation from the magnetic and coil current measurements without changing the measurements significantly. The reconstruction is a non–linear optimization problem, but EFIT transforms it into a series of linearized minimizations interwoven with the iterations of the equilibrium solver. The linearized minimizations can be carried out easily with the singular value decomposition technique. The method is fast enough that a typical 1-sec Alcator C–Mod discharge can easily be analyzed at 20 msec intervals in under five minutes. It usually takes 20 minutes between two discharges; magnet cooling and building up of stored energy make this waiting time necessary. The EFIT code is then an indispensable tool in the decision making process between two discharges in Alcator C–Mod.

After EFIT is run at the time of interest, one gets as output a set of coil currents, passive element currents, and parameters defining the $p(\psi)$ and $F(\psi)$ profiles. The inputs for the free–boundary code (ASEQ) used for the perturbational equilibrium plasma response can be derived from this information. Using the mapping procedure of Eq. 2.16, the passive currents can be transformed into an equivalent set of coil currents that produces the same poloidal flux inside the vacuum vessel as the

passive currents. The profile parametrization in EFIT is different than in ASEQ. $\frac{dp(\psi)}{d\psi}$ is given as a third degree polynomial while $F(\psi)\frac{dF(\psi)}{d\psi}$ is only assumed to vary linearly with ψ. This parametrization can be transformed into the Strickler profile parametrization (Eqs. 2.12 and 2.13) via a simple fitting process. The distribution of plasma current in space is also an output of EFIT (or ASEQ) and can be used for a multifilament representation of the plasma.

We now have a plasma equilibrium which can reproduce the magnetic signals that were used to derive it. It should be noted that, since the currents in the passive elements cannot be measured, they are free parameters used in the fitting process. The 190–element model for the passive elements described in Chapter 3 is also used in EFIT. The fitting problem that EFIT solves is not well conditioned enough to result in a unique set of passive currents. The passive currents that result from running EFIT are, therefore, not unique, even though they may reproduce the measurements accurately. As a result, they do not necessarily correspond to the physical passive current distribution at the time of interest.

5.1.2 Reconstruction Using the Circuit Equation

Another way to estimate the passive currents is to use the circuit equation (Eq. 3.1) as we did in Section 3.1.2 with no–plasma shots. The only difference, of course, is the presence of a plasma. If we represent the plasma as a set of filaments, the plasma current coupling to the passive elements can be added as another term to the circuit equation:

$$\mathbf{M}_{gg}\dot{\vec{I}}_g + \mathbf{M}_{gc}\dot{\vec{I}}_c + \mathbf{M}_{gp}\dot{\vec{I}}_p + \mathbf{R}_{gg}\vec{I} = \vec{0} \qquad (5.1)$$

Here, $\mathbf{M}_{gp}$ is the mutual coupling between the plasma filaments and the passive conductors, and $\vec{I}_p$ is a vector containing the currents in the filaments. It is assumed in Eq. 5.1 that the plasma current distribution is known at all times. This is not true, however. The time step necessary when integrating Eq. 5.1 has to be less

than the penetration time of the passive conductors or of the order of 1 msec. The only information pertaining to the plasma current, however, that is experimentally available with such temporal resolution is the total plasma current and the location of the plasma current centroid.

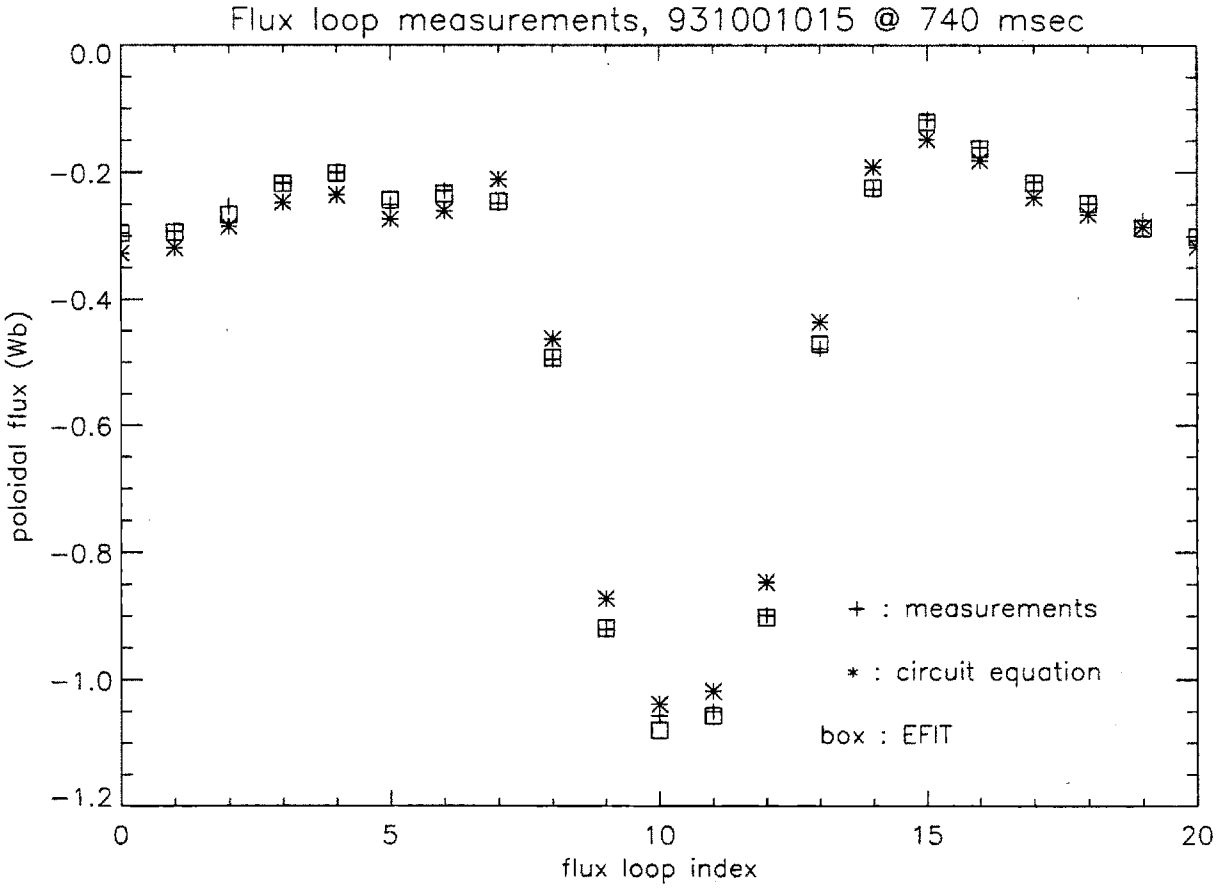

Figure 5-1: Comparison between actual poloidal flux measurements (+), predictions from EFIT (box), and the circuit equation/free boundary code combination (*).

Nevertheless, we can use the argument that was made in Section 2.2 to prove, that, in order to get a first approximation of the passive currents, all we really need is knowledge of the total plasma current and the location of the current centroid. Because of the toroidal geometry, the flux pattern created at the location of magnetic diagnostics – and, therefore, at the vacuum vessel as well – by a distributed plasma current is very similar to the flux created by a single filament carrying the total

plasma current and located at the location of the current centroid. $\vec{I}_p$ then becomes a scalar, I_p, in Eq. 5.1 and $\mathbf{M}_{pg}$ becomes a vector, $\vec{M}_{pg}$. Given $I_p(t)$, $\vec{M}_{pg}(t)$ and $\vec{I}_c(t)$, we can solve for $\vec{I}_g(t)$ starting at a time when there were no currents flowing in any of the coils. We have then the passive currents and the coil currents at any time of interest. Using the mapping procedure of Eq. 2.16, we can transform the passive currents into an equivalent set of coil currents, as was mentioned in the previous section. The only ASEQ inputs missing then are the $p(\psi)$ and $F(\psi)$ profile parameters. For lack of another source of this information, it is taken from the EFIT reconstruction, after the appropriate transformation from EFIT to ASEQ parametrization has been performed as mentioned in the previous section. It is assumed here that plasma response is not strongly dependent on the profiles. Note that the magnetic diagnostics are not used at all in this procedure.

Both techniques for reconstruction can reproduce the magnetic measurements at the time of interest satisfactorily. Fig. 5-1 shows a comparison of the magnetic flux loop readings at some time during a discharge and also their values as calculated from the plasma reconstruction using EFIT and the circuit equation approach. The EFIT reconstruction performs slightly better in this respect, which is to be expected since it uses the magnetic diagnostics in the fitting process.

The two methods give significantly different distribution of passive currents, but the flux pattern due to the passive currents inside the vacuum vessel is almost identical. This can be seen in Figs. 5-2 and 5-3. Fig. 5-2 shows the current density in the 190 elements representing the passive conductors and the poloidal flux generated by these currents inside the vacuum vessel, as these were calculated using EFIT at one instant during a discharge. Fig. 5-3 displays the same information as calculated using the circuit equation approach. Note how EFIT tends to put large currents on the inboard elements of the upper and lower domes that are closer to the midplane. To compensate for these, it has to put negative currents in the neighboring vacuum vessel elements. Integrating the circuit equation on the other

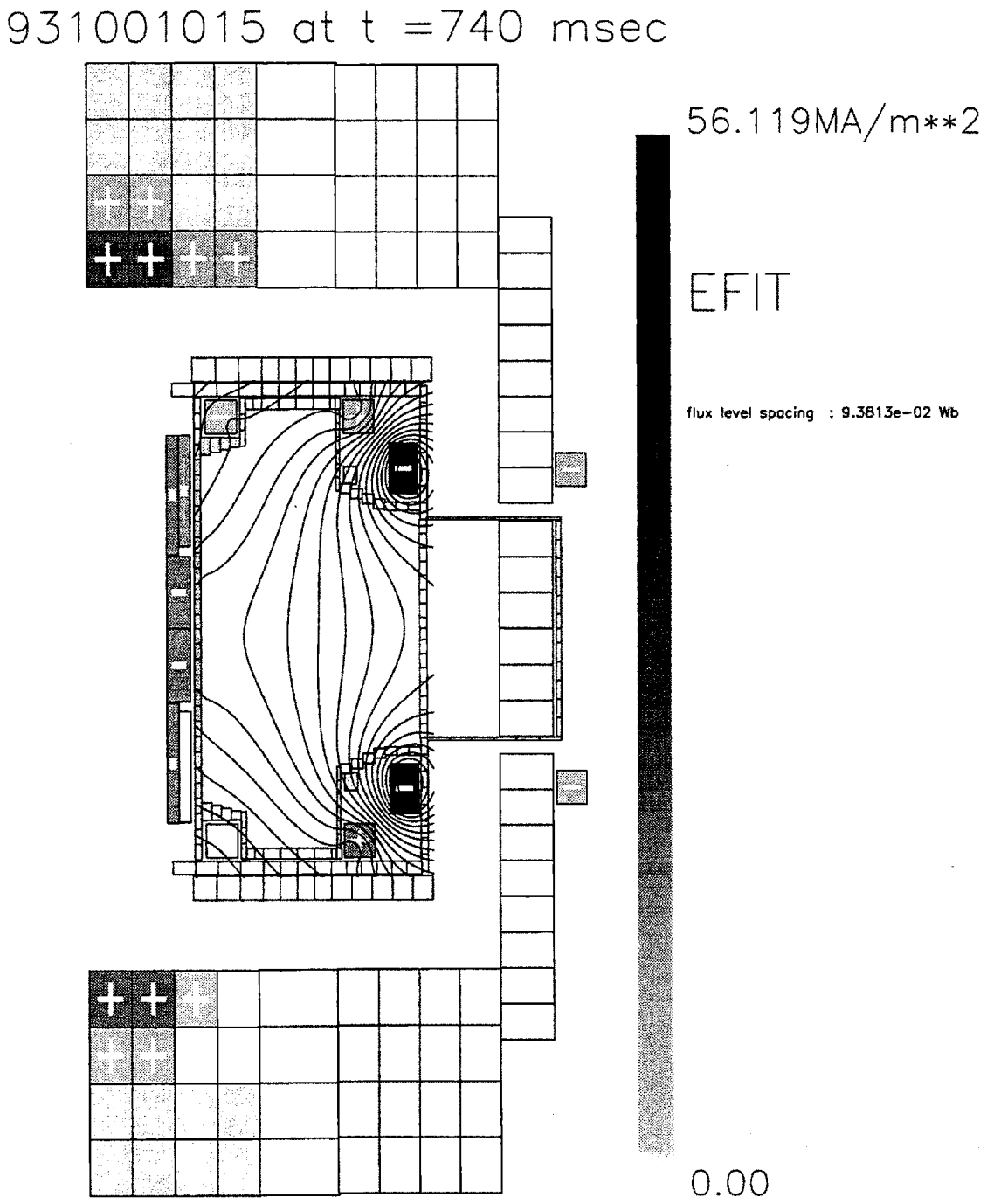

Figure 5-2: Current density in the passive conductor elements and poloidal flux due to the passive conductor currents as they are estimated using EFIT. The sign in each element indicates current direction.

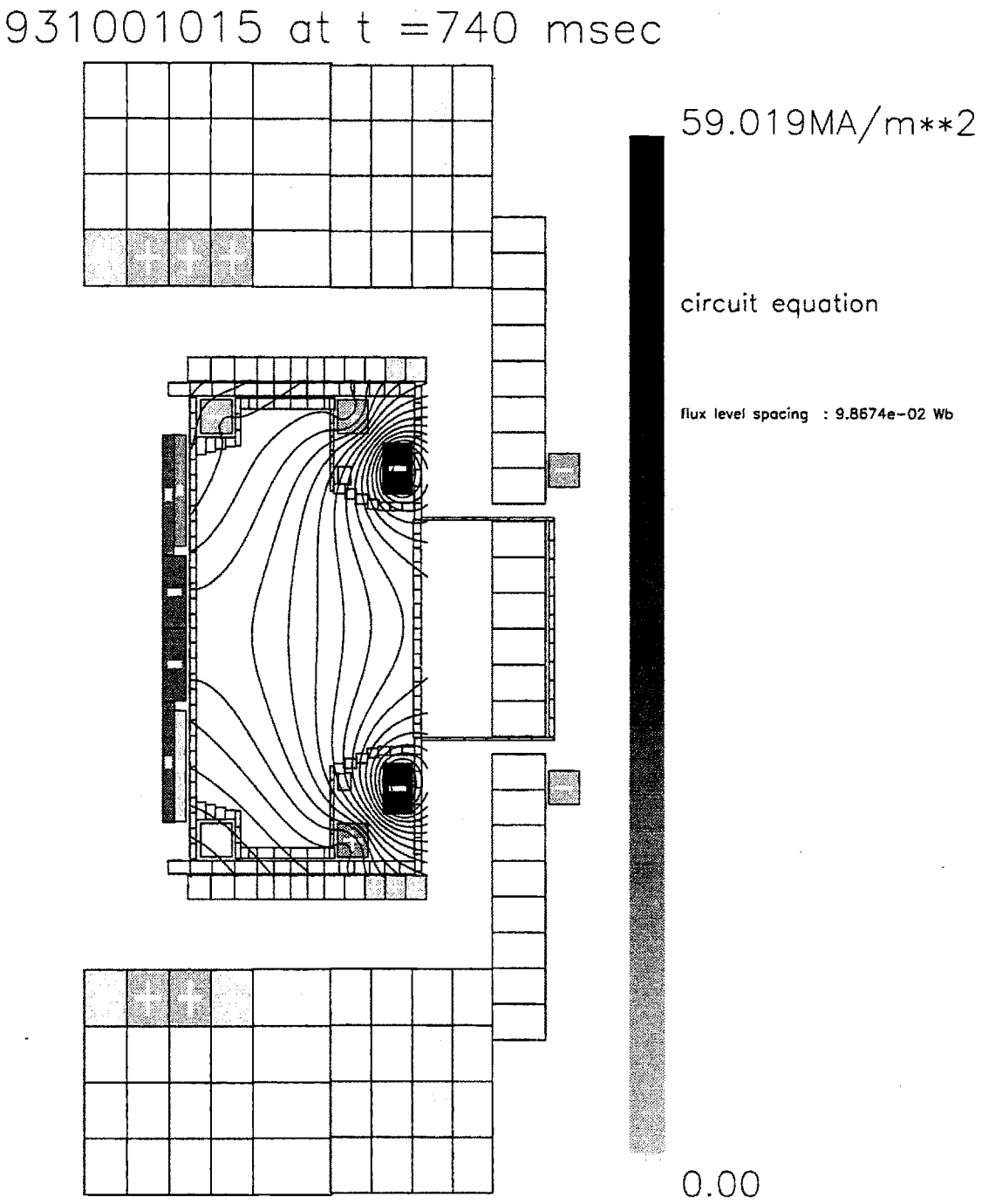

Figure 5-3: Current density in the passive conductor elements and poloidal flux due to the passive conductor currents as they are estimated using the circuit equation. The sign in each element indicates current direction.

hand, tends to give lower currents of the same sign in these elements. Although there is no way to measure the passive currents, the latter distribution should be closer to what one would expect the actual distribution to be, since all modes with neighboring elements carrying currents of opposite sign are very damped.

The flux created inside the vacuum vessel by the passive currents as calculated by the two methods is the same; all other inputs to the free–boundary equilibrium code being the same, the plasma equilibria calculated with inputs from the two methods are almost identical, and so is the plasma response calculated from them. The results presented in this and the next chapter were calculated using the circuit equation to estimate the passive currents.

5.1.3 Calculation of the Open–Loop Eigenvalues

Once the base equilibrium has been determined, the filament model or the perturbed equilibrium model can be used to determine the matrix $\mathbf{X}$ in Eq. 2.2, or matrices $\mathbf{X}$ and $\mathbf{Y}$ in Eq. 2.40 for the flux conserving version of the perturbed equilibrium model. Then, the response matrix $\mathbf{A}$ is obtained. Eigenvalue analysis of $\mathbf{A}$ shows, that, for elongated plasmas, there is always one (and only one) unstable open–loop eigenmode. The pattern of this mode is always of a vertical nature. Fig. 5-4 shows the normalized current density in the coils and passive conductor elements due to the eigenvector of the unstable mode for a typical case. Note how the mode corresponds to a distribution of currents which is almost perfectly antisymmetric with respect to the midplane, thereby creating mainly radial magnetic field in the center of the vacuum vessel, which forces the plasma to move vertically.

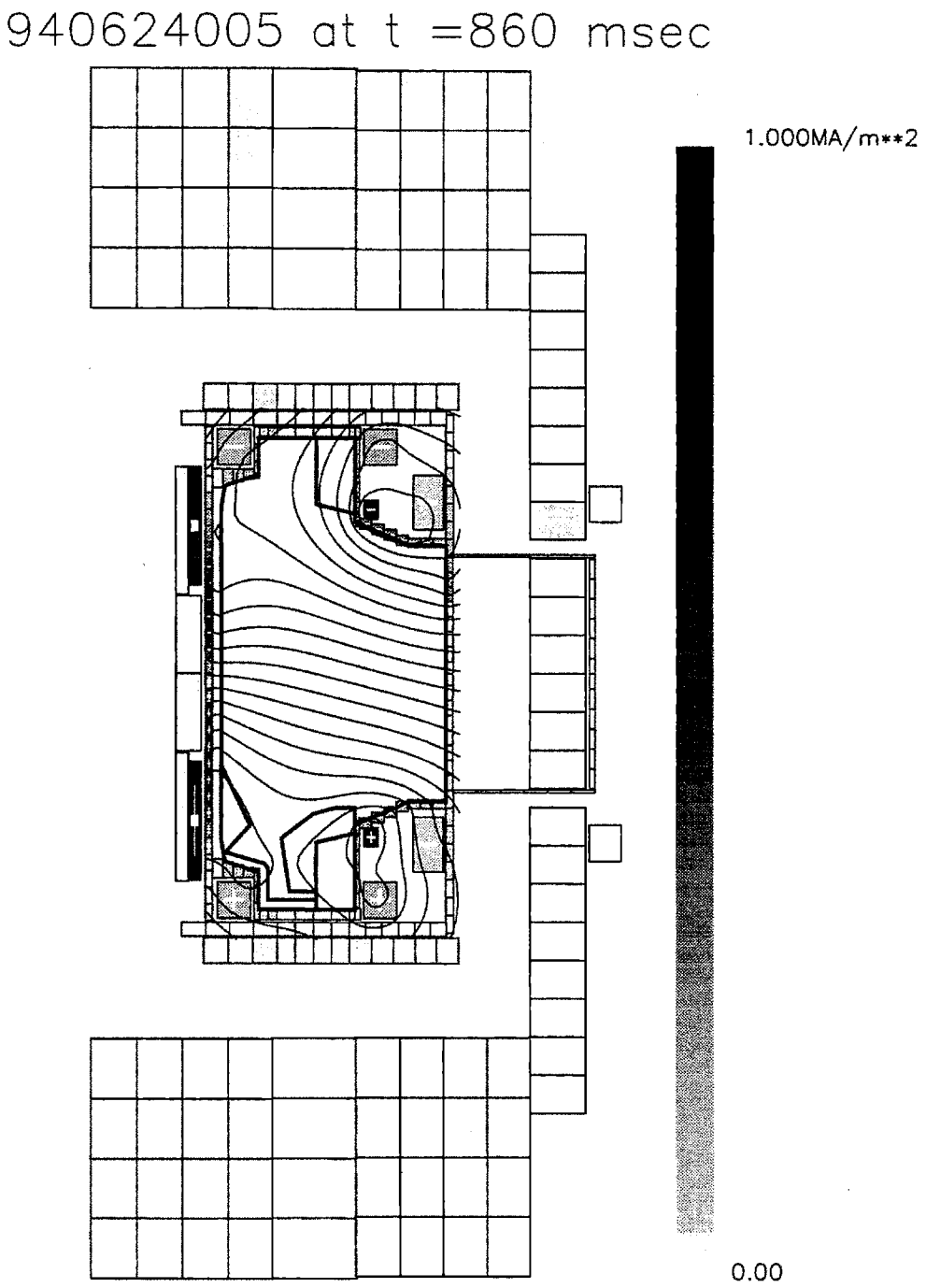

Figure 5-4: Normalized conductor current density corresponding to the eigenvector of the open-loop unstable eigenmode of a typical elongated plasma. The sign in each element indicates current direction. The flux due to these currents is also shown.

5.2 Open–Loop Experiments

The validation of the electromagnetic model of the vacuum vessel and structure in Section 3.1.2 was easy to implement in an open–loop configuration, i.e., with no feedback, since the system we were testing is stable and no feedback was needed. Testing of a plasma response model is not as easy, though, since feedback is essential in producing and sustaining a plasma, especially an elongated plasma. It is also not possible to test the $\mathbf{X}$ and $\mathbf{Y}$ matrices by themselves since the plasma always moves in the presence of the conductors around it. But, since the model of the conductors was validated very satisfactorily in Section 3.1.2, any test of the plasma–conductor system is essentially a test of the plasma response. In this section we present some experiments in which we allowed a vertically unstable plasma stabilized by means of feedback control to actually become unstable by turning off the feedback control. Predicted and observed responses are compared.

5.2.1 Experiments

In the Fall of 1993 a limited set of experiments was performed to obtain open–loop growth rates of elongated plasmas that can be compared with the theoretically predicted ones. These experiments consist mainly of fewer than 10 shots in which an elongated plasma was formed and, at some point, the vertical position feedback was turned off for a short interval and then turned back on. The duration of the interval was 10 msec. As expected, the plasma moved up– or downwards driven by the vertical instability. The feedback was turned off by setting the PID gains (see Fig. 1-7) of the feedback channels responsible for vertical position control equal to zero for 10 msec. Fig. 5-5 shows one of these gains as a function of time as well as some other signals on the same timescale. Feedback is turned off at 0.7 sec. At this point, the system consisting of the plasma and the conductors around it is in an unstable equilibrium. The slightest perturbation from this equilibrium will cause

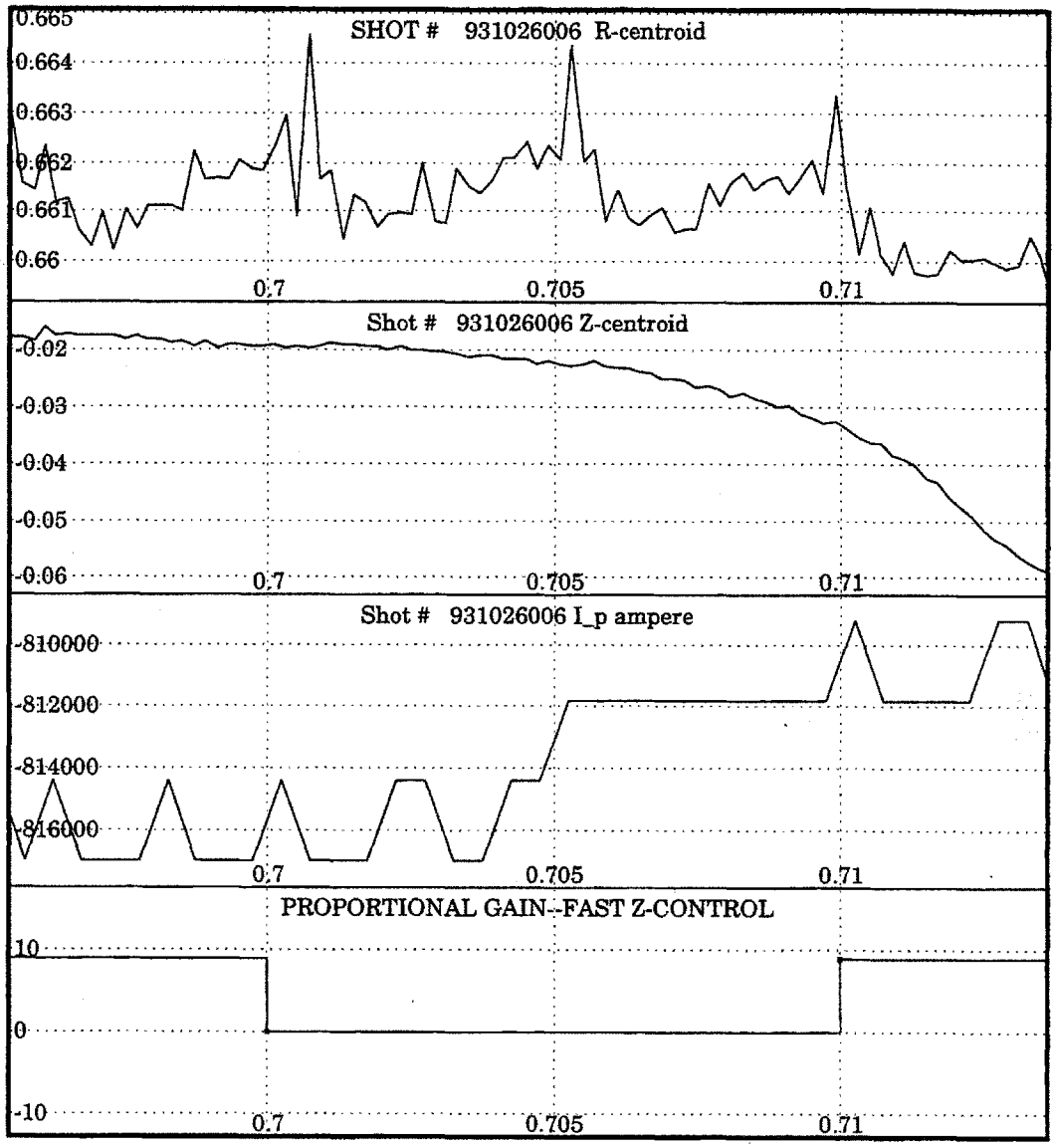

Figure 5-5: Traces characteristic of the shots where the feedback was turned off to observe plasma behavior. Shown are the R– and Z–location of the plasma current centroid (top two plots), the total plasma current (second from bottom), and the proportional gain in one of the feedback channels (bottom).

the plasma to move vertically. In most of these shots, the perturbation seems to have been a jump in the EFC coil current. The power supply for these coils can only carry current in one direction. Because of this, the coil has to carry a bias current so that one has the ability to add or subtract current. Consequently, a constant preprogrammed voltage must be applied to the EFC coil in addition to the feedback part of the demand signal. Zero output from the controller (see sketch of the PCC in Fig. 1-7) does not result in zero demand to the power supply, but rather in a demand that results in enough voltage to sustain the bias current. If the average EFC current was not exactly equal to the bias current at the time when the feedback was turned off, a zero demand signal to the supply will cause a sudden jump in the average coil current. This effect is shown in Fig. 5-6.

The total plasma current and the radial position of the plasma current centroid do not change while the vertical position becomes increasingly negative in an exponential way. At 0.71 sec, the feedback was turned back on, but it was not able to bring the plasma back to its original position. The plasma had already moved into an area where the curvature of the magnetic field was too destabilizing. The shot ended in a disruption. Unfortunately, most of these discharges ended up in disruptions. In an attempt to avoid these disruptions, some shots were run in which the time interval during which the feedback was off was 5 msec. These shots did not end up in disruption, but the vertical position excursion did not have enough time to develop the exponential pattern from which a growth rate can be read. They were, therefore, not useful for the purposes of these open–loop tests. The danger of disruption that this kind of experiments bears, is the main reason why they are not performed often. To the author's knowledge, this was the first time that the results of such experiments are ever published.

5.2.2 Results

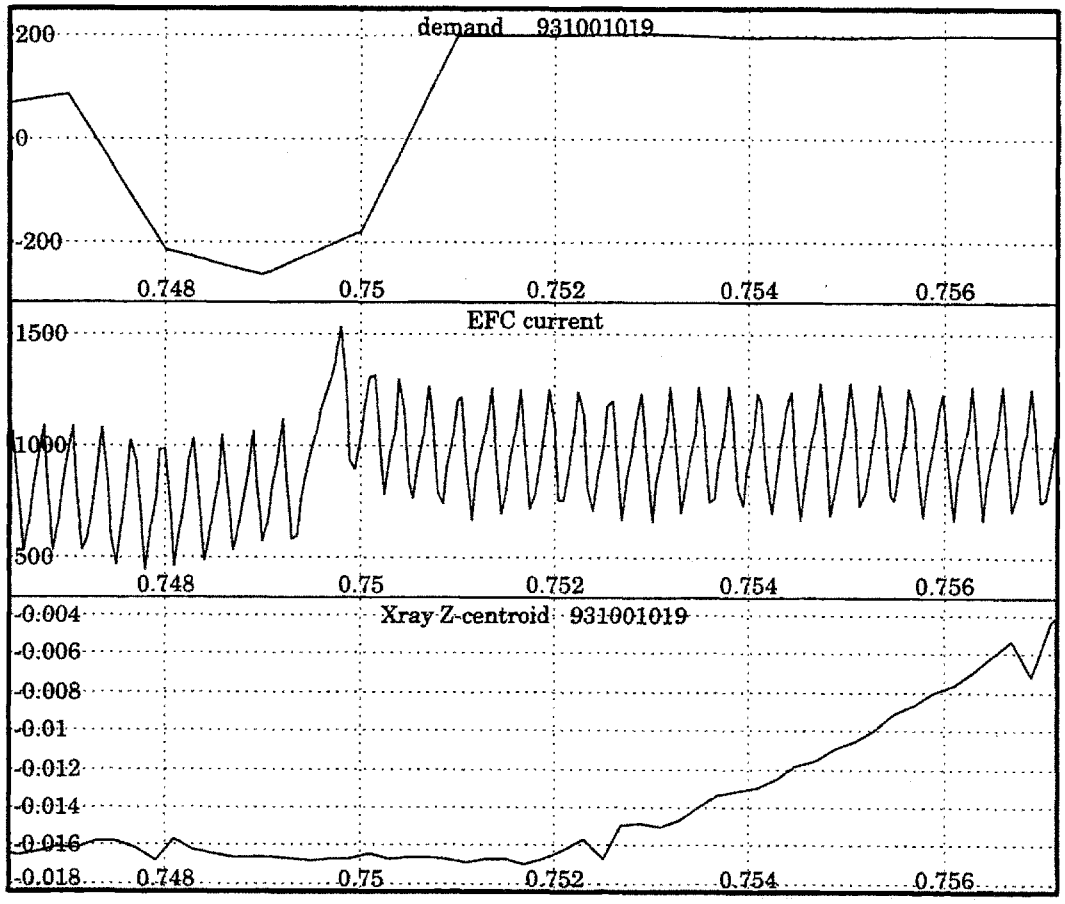

Figure 5-6: Characteristic jump in the EFC current when the feedback is turned off. Also shown is the demand to the EFC power supply and the Z–position of the plasma current centroid. The feedback is turned off at 0.75 sec.

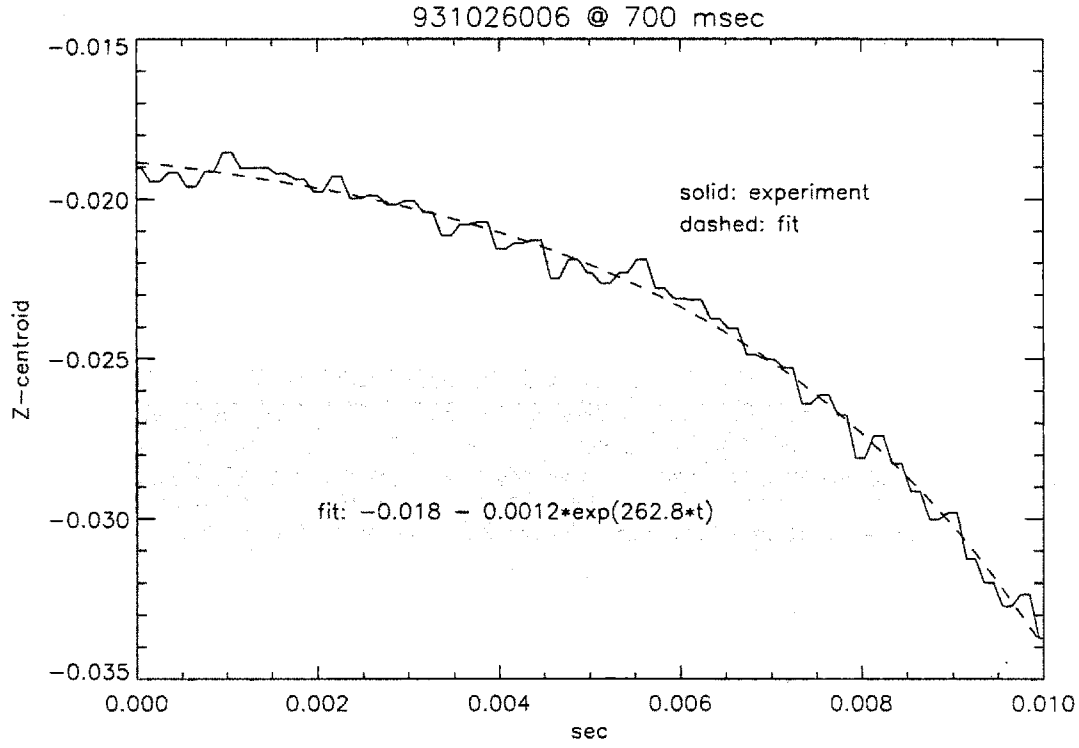

Figure 5-7: Experimentally observed rise in the Z-position of the current centroid during the 10 msec of turning off of the feedback is fitted to an exponential in order to be compared to theoretical growth rate predictions.

Shot number	observed	perturbational	filament
930916025	49.5	75.6	16.4
931001005	281.1	300.1	127.5
931001010	370.0	418.1	184.2
931001015	256.4	335.3	164.7
931001019	220.1	208.4	153.2
931026006	262.8	246.9	111.9

Table 5.1: Growth rates in sec^{-1} for some shots where the feedback was turned off.

As shown in Fig. 5-7, the measured Z-position of the current centroid as a function of time was fitted to an exponential function,

$$Z(t) = a_0 + a_1 e^{\gamma t}, \tag{5.2}$$

with a real γ, which is the experimentally observed growth rate. To compute the theoretically predicted growth rate, the plasma equilibrium was reconstructed at a time immediately prior to the time when the feedback was turned off. The $\mathbf{X}$ and $\mathbf{Y}$ matrices can then be computed using either the filament or the perturbed equilibrium methods. As discussed in Section 5.1.3, the eigenvalue of the one resulting unstable eigenmode is what we call here the theoretically predicted growth rate.

Table 5.1 shows the shots where the feedback was turned off for 10 msec. The column titled *observed* denotes the growth rate fitted to the observed rise in Z of the current centroid. *Perturbational* denotes predicted growth rates based on the perturbed equilibrium plasma response model. *Filament* denotes predicted growth rates based on a rigid filament model of the plasma. The same information is shown graphically in Fig. 5-8.

We see that the *filament* growth rates are always considerably lower than the *perturbational* growth rates. This is to be expected, since the rigid, current conserving, purely vertical mode of response that the filament model is assuming requires more energy than the energy minimizing MHD eigenmode. The perturbational equilibrium, on the other hand does not place any of these three constraints on the mode of response and should, therefore, be closer to the energy minimizing MHD

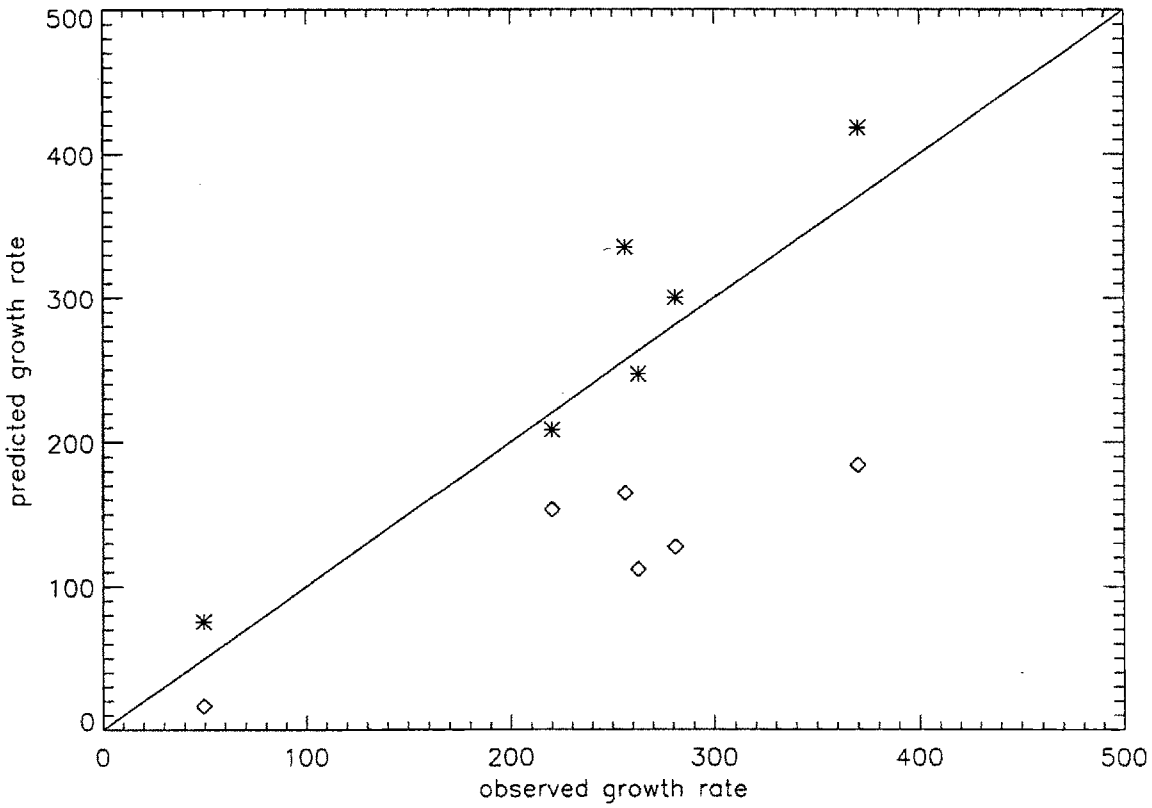

Figure 5-8: Theoretically predicted vs experimentally observed growth rates. Stars and diamonds denote growth rates calculated using the perturbed equilibrium model and the filament model respectively.

eigenmode. The agreement between *observed* and *perturbational* is within 40%, 30% for the higher elongation cases, i.e., all cases in Table 5.1 except shot 930916025.

The *observed* growth rates were calculated using a non–linear least squares fitting routine. As a crude attempt at error analysis, however, let us suppose that the *observed* growth rate is calculated in a simple way using only two points of the Z–position vs. time plot, the beginning and the end of the no–feedback interval. The equations for the first and last points are:

$$Z_1 = Z_0 + \beta e^{\gamma t_1}$$

$$Z_2 = Z_0 + \beta e^{\gamma t_2}$$

where Z and t refer to Z–position and time respectively, the subscripts "1" and "2" refer to the starting and ending points respectively and Z_0, β, and γ are fitting parameters, γ being the growth rate. We can then write:

$$\gamma = \frac{ln\frac{(Z_2 - Z_0)}{(Z_1 - Z_0)}}{t_2 - t_1} \tag{5.3}$$

Taking the derivative with respect to Z_2:

$$\frac{d\gamma}{dZ_2} = \frac{1}{(Z_2 - Z_0)(t_2 - t_1)} \tag{5.4}$$

If we call ΔZ_2 the uncertainty in measuring the vertical position, then the uncertainty in the *observed* growth rate is:

$$\Delta\gamma = \frac{\Delta Z_2}{(Z_2 - Z_0)(t_2 - t_1)} \tag{5.5}$$

Let us assume an experimental uncertainty of 5.0 mm. Discrepancies as large as 5.0 mm between the Z–position as measured using X–ray measurements (the method that was used in obtaining the *observed* growth rates) and the Z–position as obtained from the EFIT code have been observed. If we consider an excursion of 1.5 cm, then, for the 10 msec interval, $\Delta\gamma$ is of the order of 30 sec^{-1}. This error bar in *observed* growth rates is enough to explain the discrepancy between *observed* and *perturbational* growth rates for most cases in Table 5.1.

Chapter 6

Comparison to Experiment Part II: Closed Loop

6.1 Calculation of Closed Loop Eigenmodes

Fig. 6-1 shows a sketch of the closed loop we are trying to model. The box labelled "plasma, conductors, diagnostics" contains the plasma and conductor models described in Chapters 2 and 3. The "prime" denotes state space with no power supply dynamics. The box labelled "power supplies" contains the power supply dynamics described in Chapter 3. The rest of the sketch shows the parts of the plasma control computer (PCC). The previous chapter concerned itself with the open loop system consisting of the plasma, the coils, the vacuum vessel and the structure. Therefore, the $\mathbf{A}'$–matrix without any extra dynamics, was all that was needed for eigenmode analysis. When the loop is closed, however, several other systems come into play, as shown in Fig. 6-1. These are the diagnostics, the power supplies, and the PCC. The diagnostics are mainly magnetic flux and field measurements and coil current measurements and, as we saw in Chapter 2, they are related to the state by the $\mathbf{C}'$–matrix without introducing any additional dynamics. The power supplies

do introduce additional dynamics, described by the matrices, $\mathbf{A}_{ps}$,$\mathbf{B}_{ps}$, and $\mathbf{C}_{ps}$ in Fig. 6-1. These extra dynamics can be appended to the dynamics of the plasma and conductors as discussed in Chapter 2.

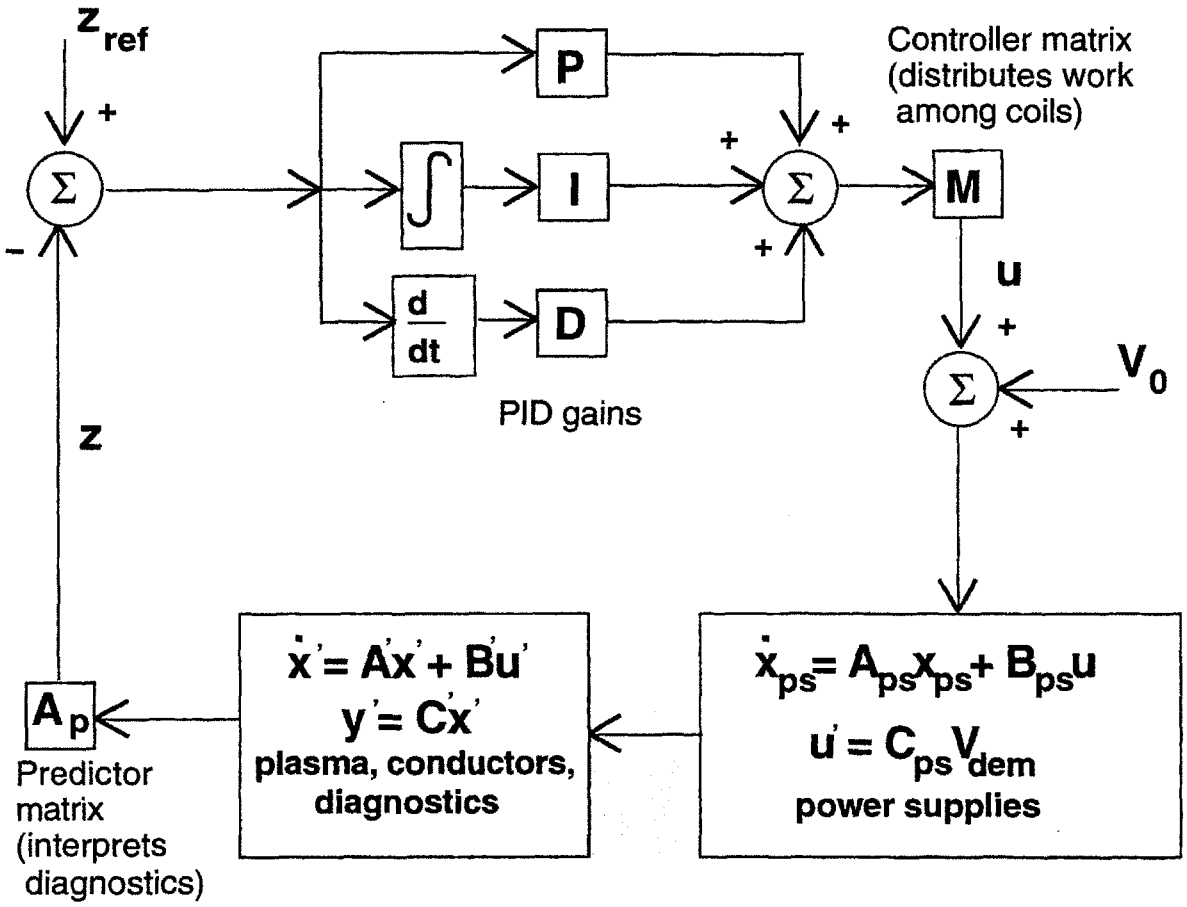

Figure 6-1: The subsystems of the closed loop.

Supposing then that, at any instant, we can reconstruct the plasma equilibrium so that we have a model for the plasma, the conductors, the power supplies and the diagnostics described by the matrices $\mathbf{A}$, $\mathbf{B}$ and $\mathbf{C}$, the diagnostic measurements can be described by $\vec{y} = \mathbf{C}\vec{x}$, the output of this system. This vector then goes through the PCC, which gives the input to the system, $\vec{u}$, namely the demand voltages to the power supplies. We should remember, that we are always dealing with perturbations from some operating point.

As shown in Fig. 6-1, the PCC consists of three parts. The predictor, the PID and the controller. The predictor matrix, $\mathbf{A}_p$, multiplies the measurement signals to give a set of linear combinations that can be identified as instantaneous values of parameters which need be controlled. No nonlinear calculation may be performed during the plasma discharge.

These predictors are calculated as follows: The locus of the magnetic diagnostics defines a surface. One usually chooses to represent the plasma current distribution as a set of toroidal currents, $\vec{I}_{in}$, inside this surface, and the currents in the coils, the vessel and the structure as another set of toroidal currents, $\vec{I}_{out}$, outside this surface. The locations where the currents $\vec{I}_{out}$ flow do not necessarily have to coincide with the real conductors. It is easy then to find the influences of these currents on the measurements, $\vec{y}$, as mutual inductances and Green's functions, $\mathbf{G}_{in}$ and $\mathbf{G}_{out}$. Given the measurements, one can then estimate these currents as

$$\begin{bmatrix} \vec{I}_{in} \\ \vec{I}_{out} \end{bmatrix} = \begin{bmatrix} \mathbf{G}_{in} & \mathbf{G}_{out} \end{bmatrix}^{\dagger} \vec{y} \tag{6.1}$$

where the "†" denotes a pseudoinverse based on singular value decomposition. The plasma current, I_p, is then the sum of the elements of $\vec{I}_{in}$. If the R– and Z–values of the locations where $\vec{I}_{in}$ flow are denoted by $\vec{R}_{in}$ and $\vec{Z}_{in}$ respectively, then the magnetic axis location of the plasma, (R_{ma},Z_{ma}), can be estimated as

$$I_p R_{ma} = \vec{R}_{in}^T \vec{I}_{in} \tag{6.2}$$

$$I_p Z_{ma} = \vec{Z}_{in}^T \vec{I}_{in} \tag{6.3}$$

One can also calculate the matrices that give the flux, magnetic field components and their gradients due to $\begin{bmatrix} \vec{I}_{in} \\ \vec{I}_{out} \end{bmatrix}$ at any location inside the vacuum vessel using $\mathbf{G}_{in}$ and $\mathbf{G}_{out}$. Combinations of these can give useful quantities to be controlled. Predictors for R_{ma} and Z_{ma} can also easily be implemented as the difference in flux at two points. A special case is the location of the lower x–point. Suppose

we have the matrices, which, when postmultiplied by $\begin{bmatrix} \vec{I}_{in} \\ \vec{I}_{out} \end{bmatrix}$, give B_{R0}, B_{Z0}, $\frac{\partial B_{R0}}{\partial R}$, $\frac{\partial B_{R0}}{\partial Z}$, $\frac{\partial B_{Z0}}{\partial R}$, and $\frac{\partial B_{Z0}}{\partial Z}$, the field components and their derivatives at some nominal x–point (denoted by the subscript "0") in the vicinity of the real x–point. A first order expansion about the real x–point gives a relation between these quantities and the radial and vertical distances between the nominal point and the real x–point:

$$\begin{bmatrix} B_{R0} \\ B_{Z0} \end{bmatrix} = \begin{bmatrix} \frac{\partial B_{R0}}{\partial R} & \frac{\partial B_{R0}}{\partial Z} \\ \frac{\partial B_{Z0}}{\partial R} & \frac{\partial B_{Z0}}{\partial Z} \end{bmatrix} \begin{bmatrix} \Delta R \\ \Delta Z \end{bmatrix} \tag{6.4}$$

Inverting the matrix in Eq. 6.4 would be a nonlinear operation since the quantities involved contain $\vec{y}$, the measurements. However, if one uses values for the derivatives from the precalculated plasma equilibrium that defined the nominal x–point – scaled by the plasma current – the matrix inversion is straight forward and one should get a good estimate.

After the predictor, the vector of parameters to be controlled, $\mathbf{A}_p\vec{y}$, goes through the PID. There, each parameter, its derivative and its integral are multiplied by different gains. Define square, diagonal matrices $\mathbf{P}$, $\mathbf{I}$ and $\mathbf{D}$ whose diagonals contain the proportional, integral and derivative gains respectively to multiply each parameter. The output of the PID is then:

$$\left(\mathbf{P}\mathbf{A}_p\vec{y} + \mathbf{I}\mathbf{A}_p\int_t \vec{y}dt' + \mathbf{D}\mathbf{A}_p\dot{\vec{y}}\right) \tag{6.5}$$

Next comes the controller (M–matrix) which distributes among the different coils the work that has to be done to bring the parameters to be controlled to their prescribed values. The output of the controller is the demand voltage to the power supplies, which is the input, $\vec{u}$, to the modeled system [**A B C**]:

$$\vec{u} = -\mathbf{M}\left(\mathbf{P}\mathbf{A}_p\vec{y} + \mathbf{I}\mathbf{A}_p\int_t \vec{y}dt' + \mathbf{D}\mathbf{A}_p\dot{\vec{y}}\right) \tag{6.6}$$

When only proportional gain is used, we can substitute $\vec{u} = \mathbf{M}\mathbf{P}\mathbf{A}_p\mathbf{C}\vec{x}$ into

the state equation to get

$$\dot{\vec{x}} = (\mathbf{A} - \mathbf{BMPA}_p\mathbf{C})\,\vec{x} \equiv \mathbf{A}_{CL}\vec{x} \tag{6.7}$$

where $\mathbf{A}_{CL}$ is the closed loop response matrix containing all the closed loop eigenmode information.

When proportional and derivative gains are used, we can use the output and the state equations to substitute for $\vec{y}$ and $\dot{\vec{y}}$ in Eq. 6.6 to get

$$\mathbf{A}_{CL} = \mathbf{A} - \mathbf{B}\,(\mathbf{1} + \mathbf{MDA}_p\mathbf{CB})^{-1}\,(\mathbf{MPA}_p\mathbf{C} + \mathbf{MDA}_p\mathbf{CA}) \tag{6.8}$$

where $\mathbf{1}$ is the unit matrix.

When proportional, integral and derivative gains are used, the number of states has to be increased to account for the dynamics of the integration. We define $\vec{x'} \equiv \begin{bmatrix} \vec{x}_1 \\ \vec{x}_2 \end{bmatrix}$ where $\vec{x}_1 = \vec{x}$ and $\vec{x}_2 = \dot{\vec{x}}$, and the new system has the following state space matrices:

$$\mathbf{A}_i = \begin{bmatrix} \mathbf{0} & \mathbf{1} \\ \mathbf{0} & \mathbf{A} \end{bmatrix} \quad \mathbf{B}_i = \begin{bmatrix} \mathbf{0} \\ \mathbf{B} \end{bmatrix} \quad \mathbf{C}_i = \begin{bmatrix} \mathbf{C} & \mathbf{0} \end{bmatrix} \tag{6.9}$$

$\dot{\vec{u}}$ is the input to this system. The closed loop response matrix now becomes:

$$\mathbf{A}_{CL} = \begin{bmatrix} \mathbf{0} & \mathbf{1} \\ \mathbf{Q}_3 & \mathbf{Q}_1^{-1}\mathbf{Q}_2 \end{bmatrix} \tag{6.10}$$

where

$$\mathbf{Q}_1 = \mathbf{1} + \mathbf{BMDA}_p\mathbf{C} \tag{6.11}$$

$$\mathbf{Q}_2 = \mathbf{A} - \mathbf{BMPA}_p\mathbf{C} \tag{6.12}$$

$$\mathbf{Q}_3 = -\mathbf{Q}_1^{-1}\mathbf{BMIA}_p\mathbf{C} \tag{6.13}$$

$\mathbf{A}_{CL}$ is of twice the size of $\mathbf{A}$ and will have half of its eigenvalues equal to zero. It should be emphasized here that the gains used in the closed-loop analysis are the actual gains used in the PCC as they are read from the hardware.

While in the open loop case it is easy to find the vertical mode – for elongated plasmas, it is the one unstable mode – in the closed loop case there are usually no unstable modes – this is after all the primary purpose of feedback control – and one has to look at the modes carefully to discern the vertical ones. This is done by looking at contour plots like the ones in Fig. 6-4. The left plot shows the contours of constant poloidal flux created by the eigenvector of a mode. Remember that the eigenvector is a combination of currents in the coils, vessel and structure. Where the contour lines are horizontal, i.e., $\frac{\partial \psi}{\partial R} = 0$, $B_Z = 0$; therefore the magnetic field is purely radial and exerts a vertical force on the plasma. Modes that have a large area of nearly horizontal flux contour lines near the magnetic axis of the plasma are thus identified as vertical modes. The right plot shows plots of the equilibrium poloidal flux contours (solid lines) taking the plasma into account. The dotted lines are contour plots of the sum of the equilibrium poloidal flux and the flux due to the eigenvector multiplied by an arbitrary constant. This plot is a visual aid in determining the plasma motion caused by an eigenmode.

6.2 Comparison to Experiment

6.2.1 Background Oscillations

As mentioned in Section 3.2, one experimental observation that can be identified as an eigenmode and be compared to the theoretically predicted closed loop eigenmodes is a background oscillation in the Z–position of the plasma that occurred often during early elongated discharges. Their frequency is not always the same; it varies between 50 and 120 Hz. It has been believed ([50]) that this oscillation was due to the slow response of the OH2 power supplies. In the first phase of the 1993 campaign, this oscillation usually had a frequency of approximately 100 Hz, which could arise if the OH2 power supplies had a 0.005 sec delay. This seems reasonable,

although, the power supply dynamics had not been determined experimentally yet. It has been argued([50]) that his oscillation goes away when integral gain is applied to the slow Z–position feedback channel and the proportional is decreased. However, a maintenance period elapsed between the campaign phase, when the integral gain was not available, and the last phase of the 1993 campaign, when it was. During this maintenance period Alcator C–Mod was reconfigured to produce poloidal and toroidal fields and plasma current of sign opposite to that of before. The amplitude of these oscillations was indeed considerably reduced after the maintenance break as compared to before. However, a "same–conditions" comparison has not been made to investigate the effect of integral gain. The nearest thing to such a comparison

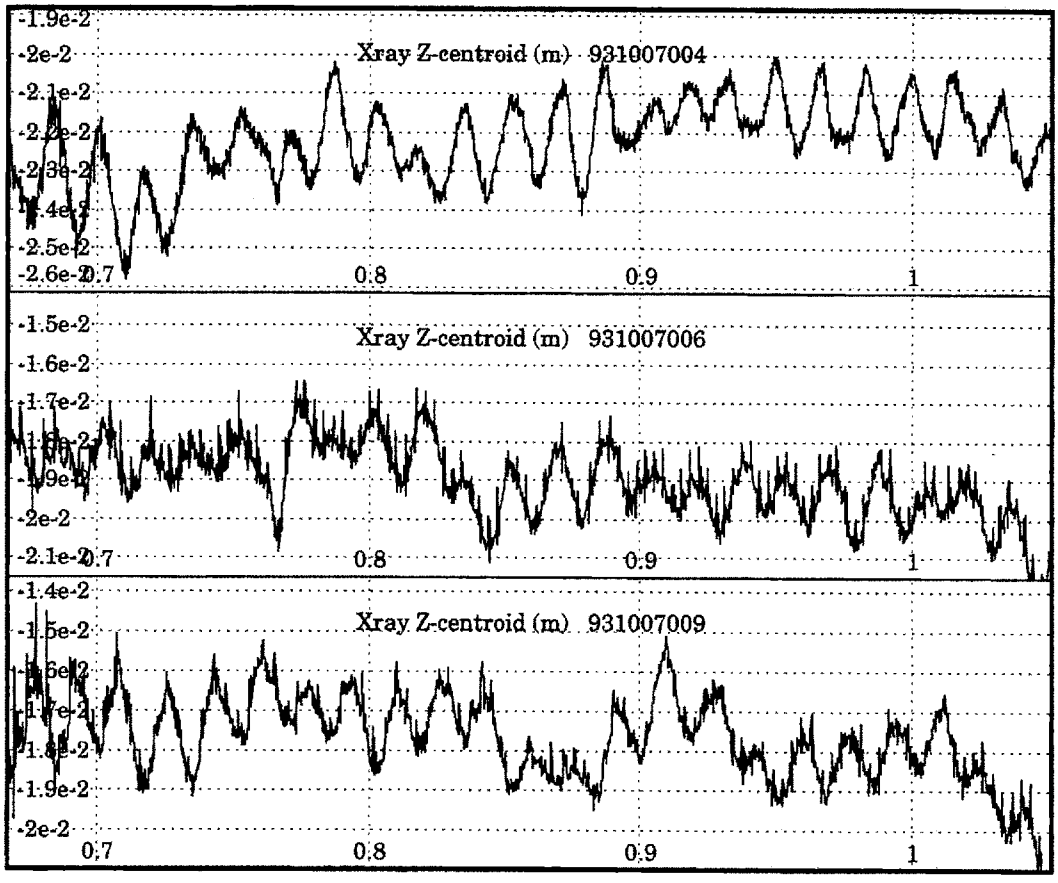

Figure 6-2: Z–position traces of the plasma current centroid as calculated from soft X–ray tomography measurements for three shots from the day when integral gain was applied for the first time.

shot number	proportional gain	integral gain	derivative gain
931007004	1.0	0.0	1.0
931007006	1.0	2.0	1.0
931007009	0.48	4.0	1.0

Table 6.1: Feedback gains applied to the slow Z–position control channel for three cases.

that exists so far is shown in Fig. 6-2. It shows the Z–position trace for three shots from the first day when integral gain was applied. A set of gains was chosen for the slow Z–position control channel on that day which was not changed during the rest of the 1993 and the 1994 Alcator C–Mod campaign. The gains applied to the slow Z–position are shown in Table 6.1; these numbers are out of a maximum of 10. All traces in Fig. 6-2 have a 2 mm peak–to–peak oscillation, even though the integral gain has been increased and the proportional gain decreased gradually from the first to the third. There is also a difference in the plasma equilibrium between the top and the bottom two traces in Fig. 6-2. Even though all three equilibria have the same elongation, the bottom two have a higher average Z–position. Hence this comparison is also not at the same conditions.

It is clear that one ought to scan the gains to see what the exact cause of the vertical oscillation is. It is not clear that OH2 dynamics is the cause and more integral gain the cure. As a counterpoint the argument will be made in this section that this vertical oscillation is not due to OH2 power supply dynamics but rather due to the interaction between the plasma and the EFC coils.

Fig. 6-3 shows an example of such an oscillation at 110 Hz. If we carry out the eigenmode analysis outlined in the previous section for this case, we find a single oscillatory vertical mode with eigenvalue $-97.9 \pm 608.7i$. Its flux pattern is shown in Fig. 6-4. This mode has a frequency close to the observed one but seems too strongly damped to be consistent with the observed quite coherent oscillations. It will be referred to as the vertical mode (to be distinguished from power

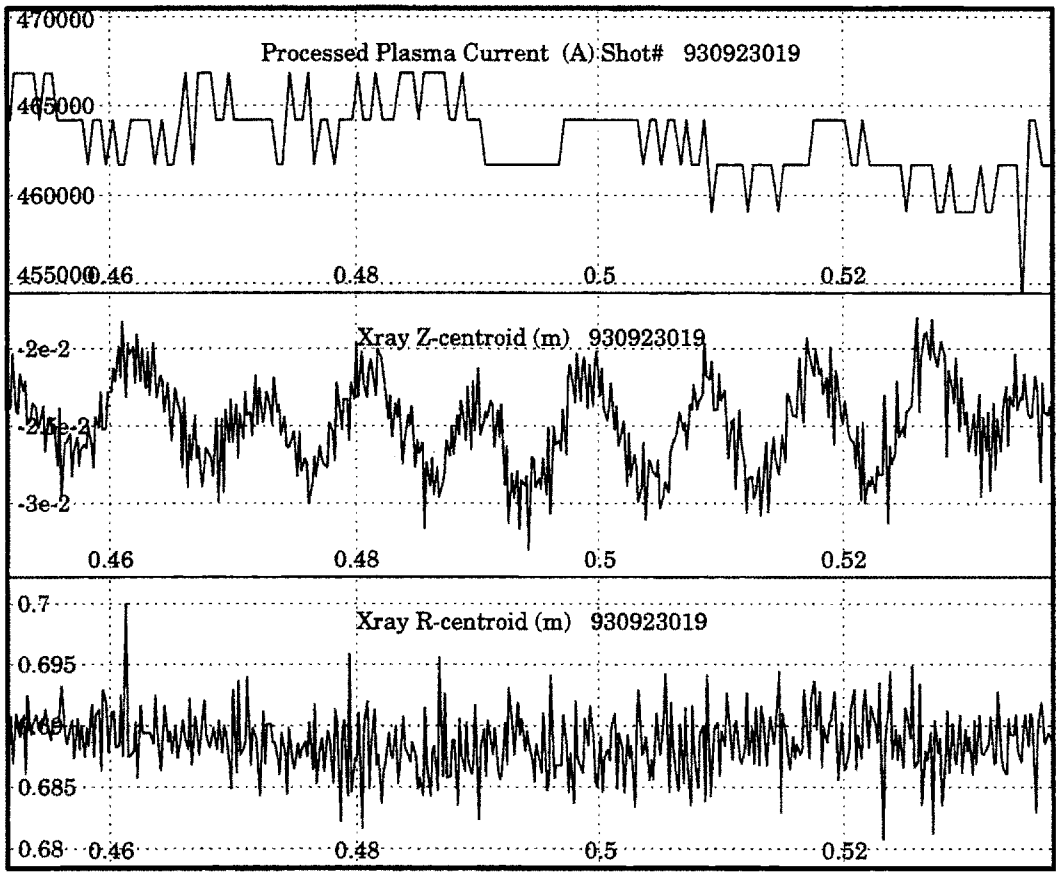

Figure 6-3: Traces characteristic of the vertical oscillation. The top trace shows the plasma current. The bottom two traces show the Z– and R–position of the plasma current centroid as calculated from soft X–ray tomography measurements.

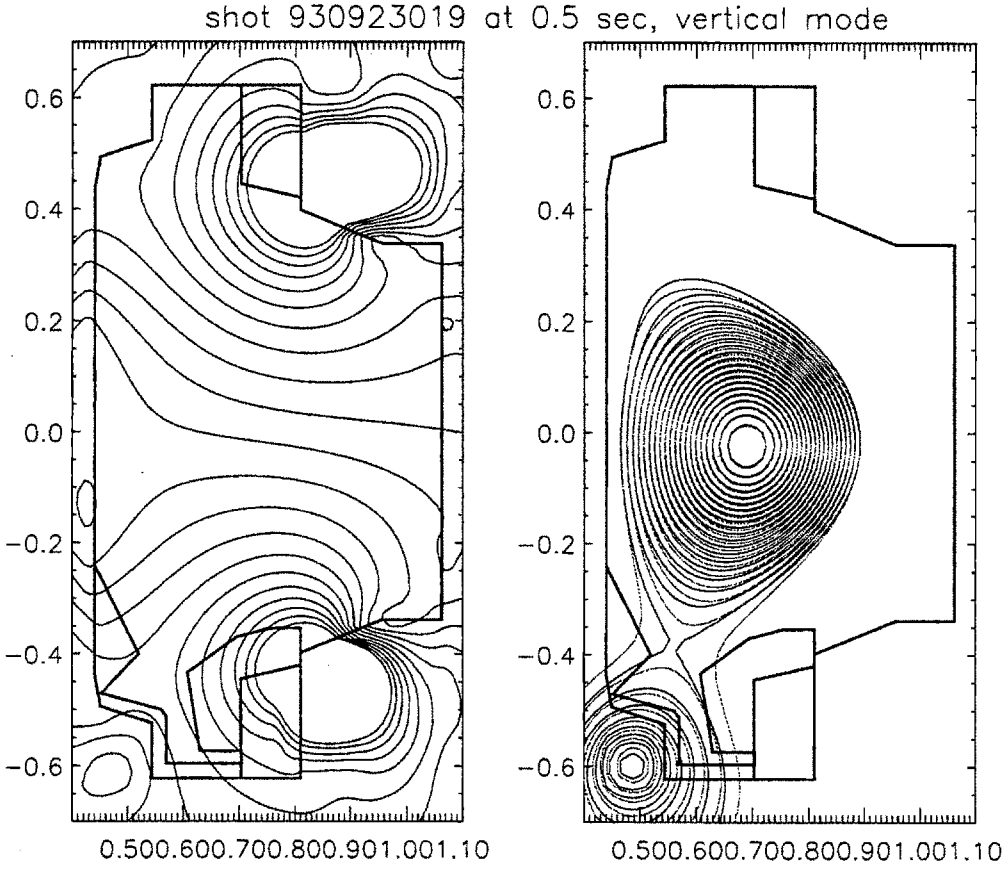

Figure 6-4: Flux created by the eigenvector of the vertical mode by itself (left) and overlaid on the plasma equilibrium flux (right).

supply modes which may cause vertical motion), because it exists even when perfectly responsive power supplies are assumed: if the above calculation is carried out without considering the OH2 power supply dynamics, we still get a vertical mode of eigenvalue $-34.7 \pm 641.9i$, indicating that the OH2 power supplies are not its cause. In order to determine the nature of this mode, one useful test is to check how the calculated eigenvalues move when the gains are varied. Fig. 6-5 shows the root locus (i.e., the location of the eigenvalue) of the above theoretically predicted vertical mode as the output of the controller to the EFC power supply is multiplied by the factor indicated next to each point. A factor of one indicates the actual gain used in the particular discharge. We see that the eigenvalue of the vertical mode is greatly affected by how much the EFC coil is used in the feedback process. Fig. 6-5 also shows the root locus of a mode of a vertical nature due to OH2 power supplies. The reason this mode is attributed to the to OH2 power supplies is that, when the OH2 supply dynamics are not included in the calculation, this mode does not appear. As the EFC controller gain decreases, the task of controlling the vertical position falls increasingly on the OH2 coils, and their power supply dynamics drive the system unstable. As the EFC controller gain increases, the vertical mode becomes increasingly more damped, until at some point the gain becomes too much, turns the locus curve around and drives the vertical mode unstable. At the same time the OH2 supply mode goes to the position it has when the power supplies are not connected to the rest of the system, indicating that they are not being used in the control process. This plot also indicates that, with a slightly larger gain (around 1.25), the vertical mode would be only marginally damped, while the frequency would still be similar to the observed one. Given the uncertainty in the EFC power supply dynamics, and in the variation of gains as a function of demand, it may indeed have been the case that the overall gain of the EFC power supplies was 1.25 times the gain measured in the power supply characterization experiments.

If the output of the controller to the OH2 power supplies is varied (Fig. 6-6),

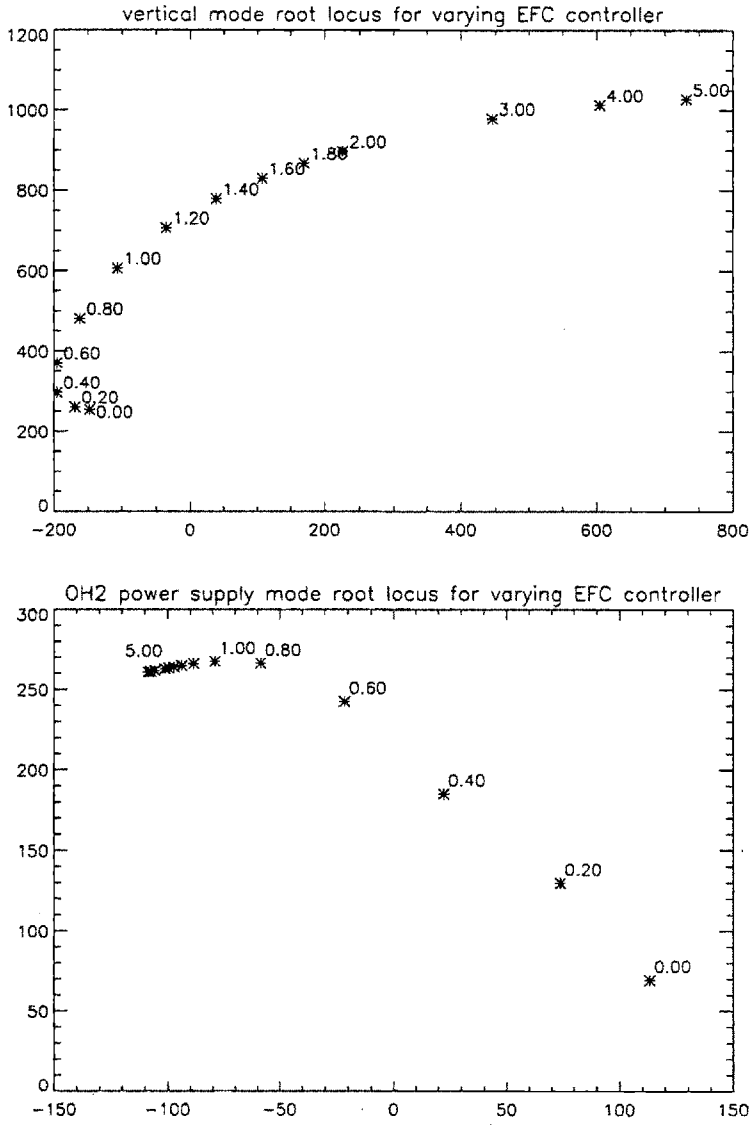

Figure 6-5: Root locus of the vertical mode (top) and the OH2 power supply mode (bottom) when the EFC controller gain is varied.

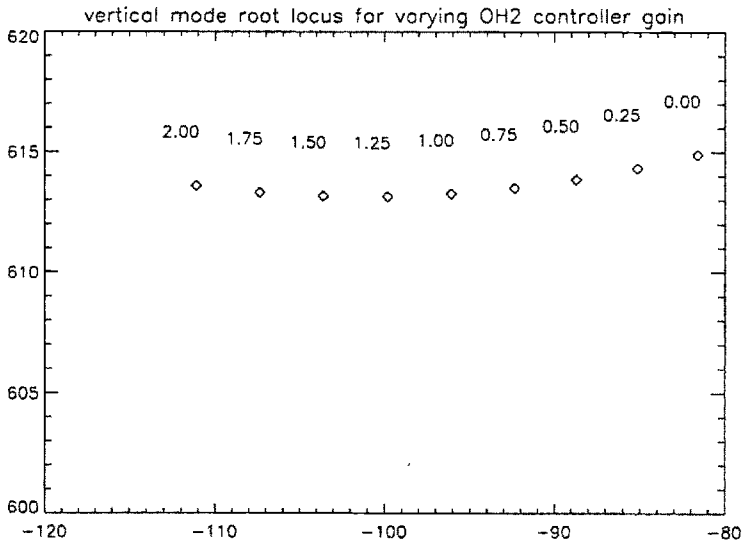

Figure 6-6: Root locus of the vertical mode when the OH2 controller gain is varied.

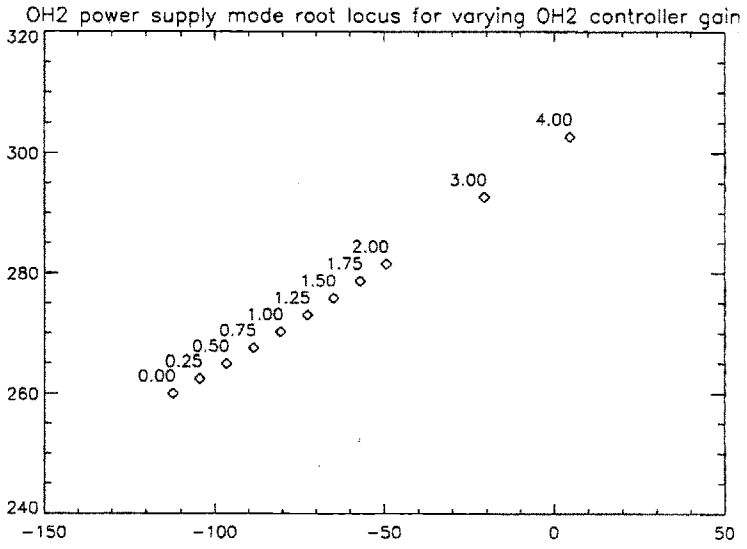

Figure 6-7: Root locus of an OH2 power supply mode when the OH2 controller gain is varied.

the eigenvalue of the vertical mode is not affected as much. It is also noteworthy that one of the eigenmodes peculiar to the OH2 power supply dynamics, which normally has a pole at $-112 \pm 255i$, moves considerably and eventually becomes unstable when the gain becomes larger than what was used in this shot (Fig. 6-7). However, this mode is not of a vertical nature (see Fig. 6-8) and the imaginary part of its eigenvalue is not near the observed oscillation frequency.

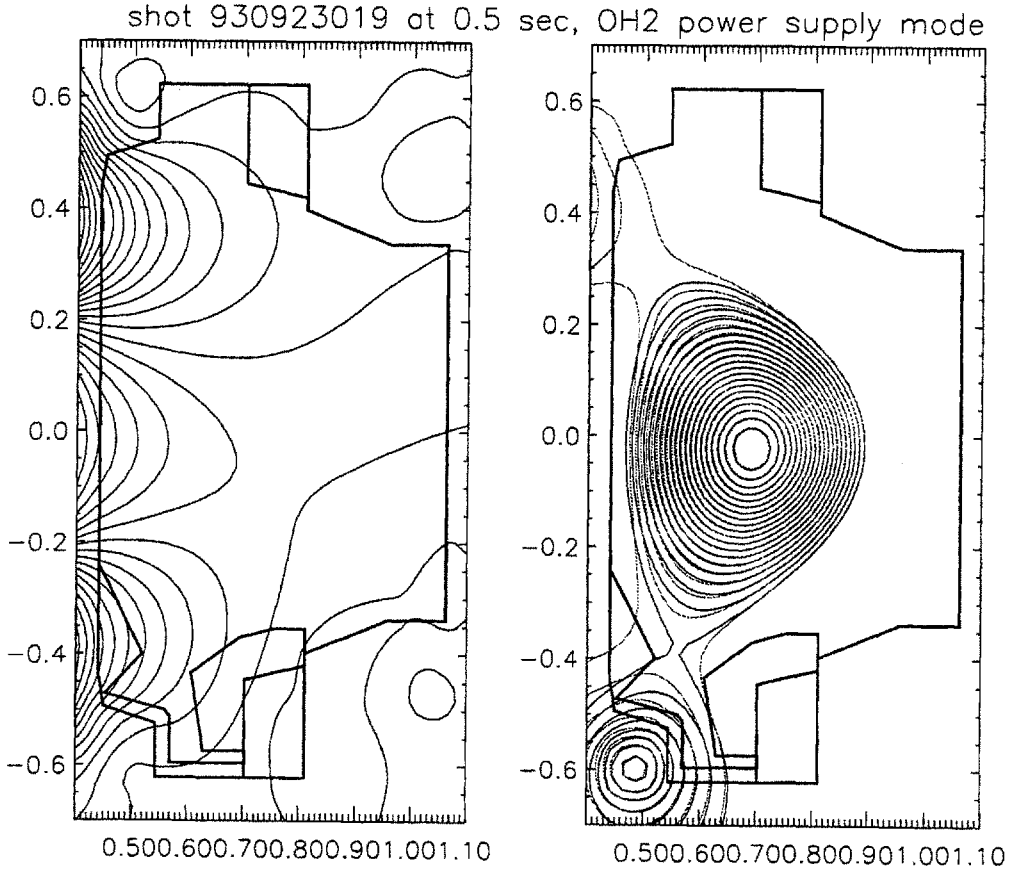

Figure 6-8: Flux created by the eigenvector of one of the OH2 modes by itself (left) and overlaid on the plasma equilibrium flux (right).

Searching through the existing data, a case could be found, where the only difference between two shots is the derivative gain on the fast Z–position feedback channel which only drives the EFC coils. The Z–position traces for these two shots are shown in Fig. 6-9. The only difference between these two shots is that one of

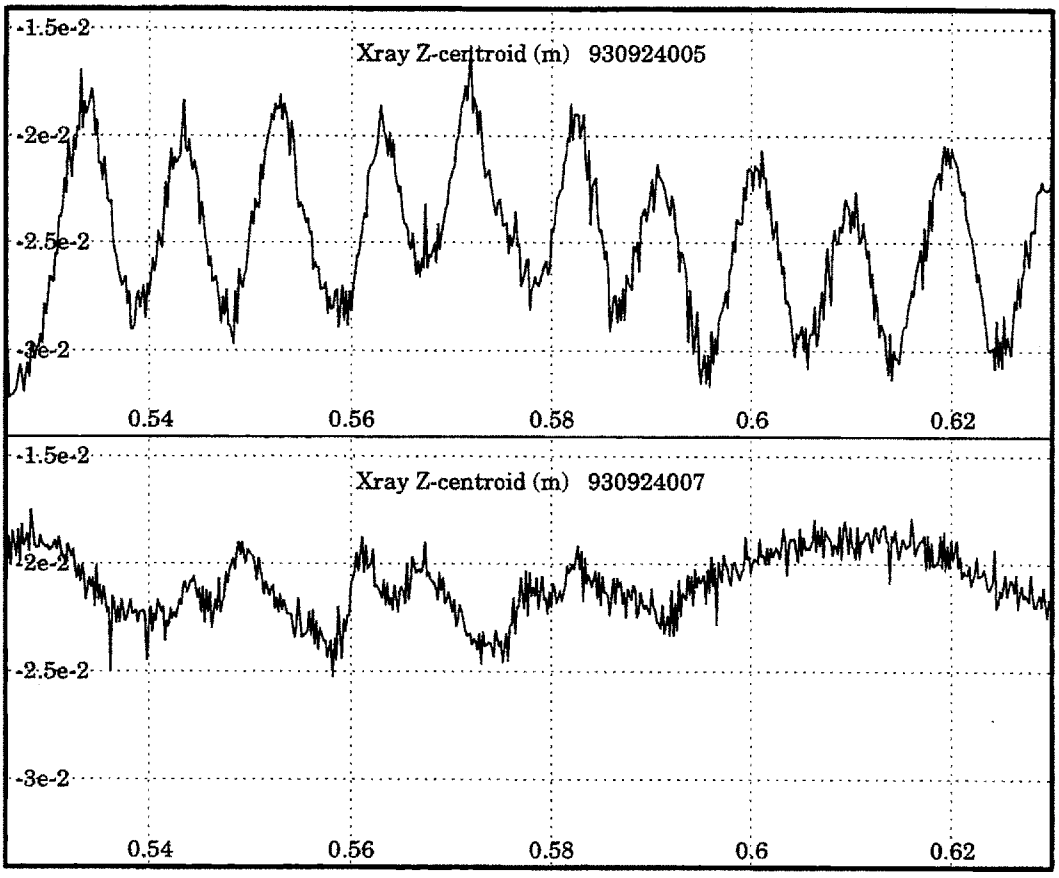

Figure 6-9: Z–position of the plasma current centroid as calculated from soft X–ray tomography measurements for two shots with different derivative gain in the fast Z–position control channel.

them (top) has no derivative gain on the fast Z–position feedback channel while the other (bottom) has a gain of 3. The oscillations have been clearly suppressed in the shot with the derivative gain.

All the above seems to indicate that these background oscillations are not due to the inadequacies of the OH2 power supplies as implied in [50]. In order to prove this, one would have to do some gain scans in the real experiment and observe response.

6.3 Perturbative Tests

The previous section concerned itself with comparison to theory of observed phenomena which were not caused intentionally for that purpose. In June 1994, one day of shots was dedicated to vertical stability tests. Unfortunately, midway through that day, an accident involving the coaxial cable feeding the OH2L coil occurred which caused operation of Alcator C–Mod to be stopped for repairs for the following four months. Several shots were obtained on that day related to the vertical stability of elongated plasmas.

The main idea in all these shots is to inject a square wave perturbation into the programming of the desired value of $I_p Z_{ma}$ and watch how the plasma relaxes to its new equilibrium after each shot. Something similar to this was done in [13]. The only difference is that, whereas in [13] the perturbations were injected after any derivative gain had been applied, in our case they were injected between the predictor matrix and the PID (see Fig. 1-7). This approach can lead to large spikes which may cause the power supplies to reach their operational current or voltage limits. This is especially important for the EFC power supply chopper which mainly takes care of fast Z–position control. This chopper used to have an overcurrent protection circuit capable of terminating the shot, but, prior to the 1994

operating campaign, this circuit was replaced by a current limiting circuit. When the current reaches a preset limit, this circuit reverses the sign of the demand signal to the chopper momentarily, so that the effect is one of saturation rather than shot abortion. The fact that the output of the PID and controller matrices has a maximum level presented another potential problem. The spikes could cause the demand signals to saturate. From an operational point of view, this may not be a problem, provided the power supply voltage and current limits are not exceeded. Saturated demand signals add nonlinearity to the closed–loop system, however, which will make it more difficult to compare its response to that of the the linear theoretical model of the system, especially since the EFC chopper behavior tends to be considerably different than the empirically derived model of Chapter 3 under such conditions. The magnitude of the Z–perturbation was large enough to occasionally result in some saturation of the demand signals. The shots that were analyzed and are presented in this section are the ones that have a minimum amount of saturation. The effect of saturation of the demand signals is discussed further in Section 6.4.

The nominal plasma parameters in these shots were $I_p = 600$ kA, $B_T = 5.4$ T, $R_{ma} = 0.68$ m, and elongation of slightly larger than 1.5. They were all of a lower single–null configuration. Fig. 6-10 shows characteristic traces from one of these shots. The top left trace shows steps injected into the I_pZ_{ma} reference signal. We are feeding back on I_pZ_{ma} rather than Z_{ma}. In addition, we are feeding back on I_p and the steps are injected during a time when the plasma current is constant so that they are essentially 1 cm steps in Z_{ma}. The change from one value of the step to the other is completed in 1 msec. The middle left trace shows the difference between the I_pZ_{ma} output of the predictor matrix and the reference signal. The spikes due to the steps are pronounced. This error signal goes into two different feedback channels, the slow Z–position channel which mainly drives the OH2 coils and the fast Z–position channel which drives the EFC coils. The bottom left trace

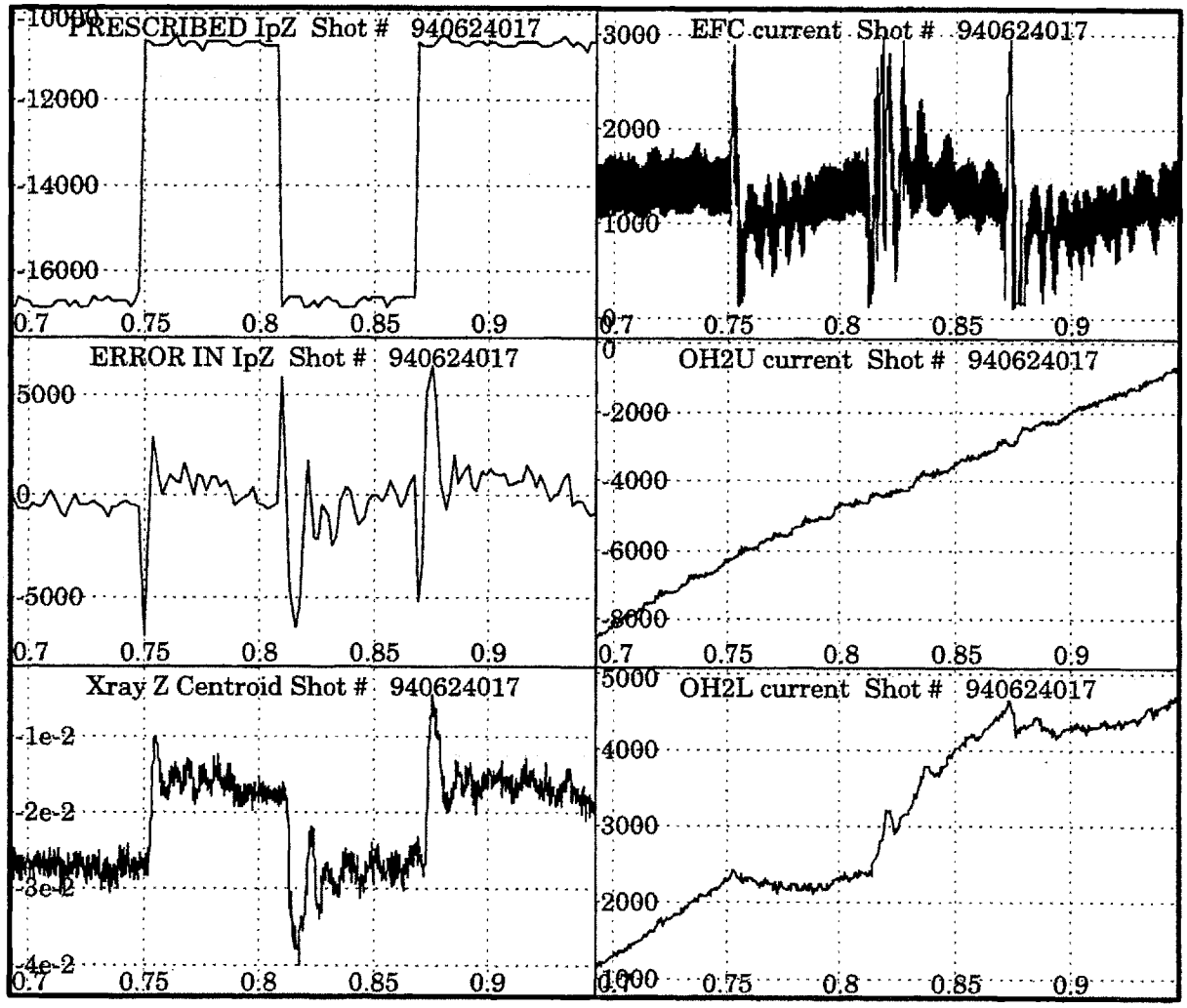

Figure 6-10: Characteristic traces from a shot with steps in the prescribed Z-position.

shows the Z–position of the plasma current centroid as calculated from the soft X–ray tomography measurements. The top right trace shows the current of the lower EFC coil current. The on– and off–pulses of the chopper give this signal its "noisy" appearance. The middle and bottom right traces are the OH2U and OH2L coil currents. The OH2U current seems unaffected by the steps; the ramping up of the current has to do with plasma current control. The OH2L is affected by the steps, because it is also involved in the control of the position of the lower x–point, which is apparently very sensitive to vertical displacements.

What happens in these traces can be explained with the help of the following simplified picture: Looking at the 0.75 sec step, the error in $I_p Z_{ma}$ suddenly becomes negative. This sends a demand signal to the EFC coils that produces the first (upward) current spike in the lower EFC coil current trace. Fig 6-11 shows the polarity of the EFC coil and plasma currents. Let us portray the plasma as a current carrying filament originally sitting in the equilibrium field generated by the coils. The equilibrium position is where $B_R = 0$. Remember, that we are considering response on the 1 msec timescale so we are not dealing with plasma inertia. Neglecting eddy currents in the vacuum vessel, if we apply a positive (into the page) current step to the lower EFC coil (which also means a negative current step to the upper EFC coil, since they are connected in antiseries), the radial field will increase so that the $B_R = 0$ point of the field due to the coils alone moves below the plasma. Of course the plasma is always on the $B_R = 0$ point of the total field, i.e., the eddy currents keep the plasma where it is in the beginning so it ends up above the equilibrium point of the field due to the active coils. As the damping effect of the eddy currents decays, the plasma moves upwards so as to create more eddy currents and compensate for their decay. All this presupposes that the EFC coils have better coupling to the plasma than the eddy currents. This first EFC current spike then has the effect of pulling the plasma upwards. As the plasma moves upwards, the output of the PID due to the proportional part of the fast Z–position

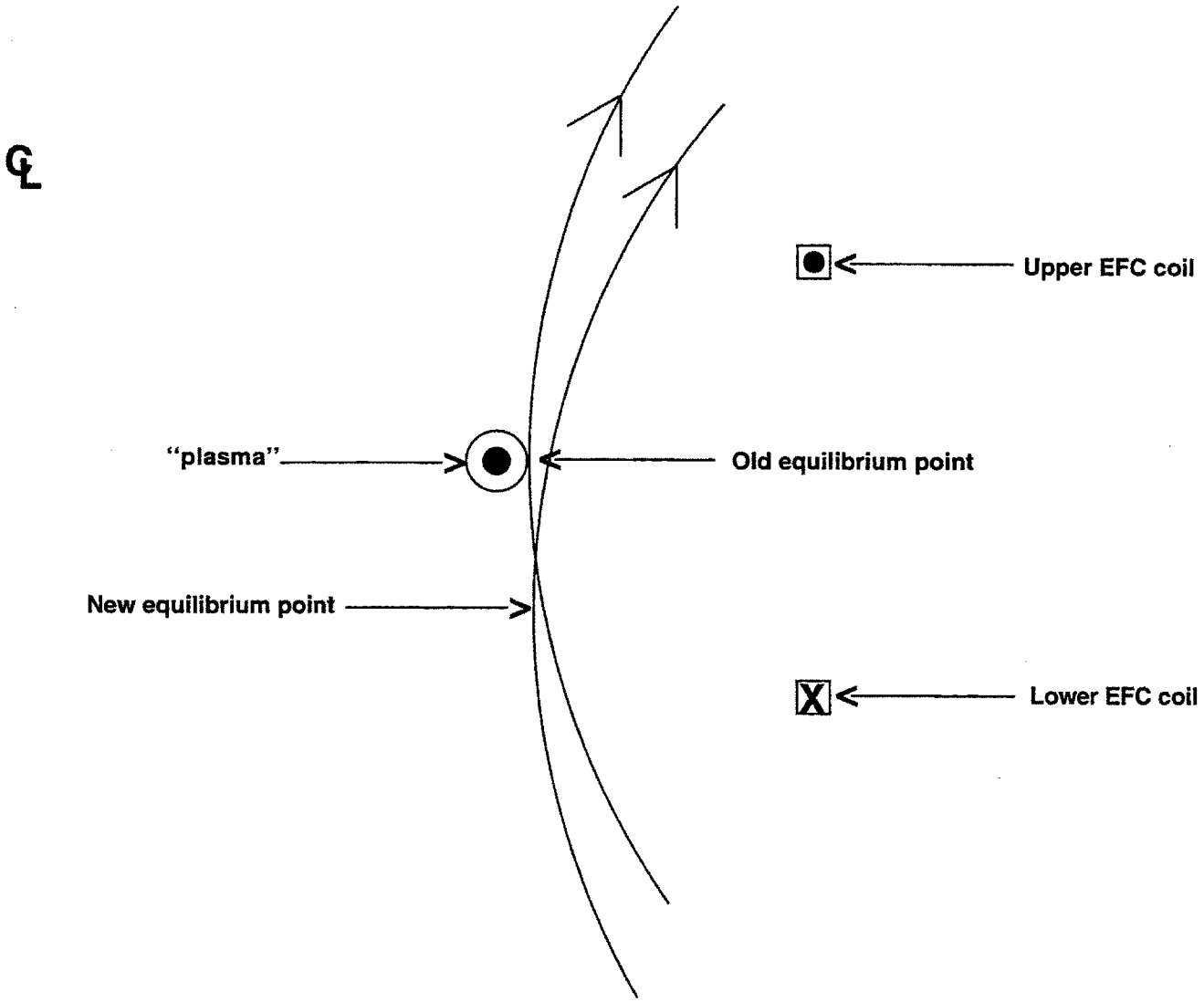

Figure 6-11: Simplistic picture of a"filament plasma" in the presence of the vertical field created by the EFC coils.

error control channel decreases (and eventually changes sign if there is overshoot as in the case of Fig. 6-10), while the derivative part increases. The demand to the EFC eventually changes sign resulting in the second (downward) spike in the lower EFC coil current, which tries to push the plasma down or decrease the rate at which it is moving upwards. Eventually an intermediate equilibrium is reached, where the average EFC current is different than the 1500 A bias current before the step. This is only possible as long as the Z-position error trace is non–zero, as is the case. Now the equilibrium field due to the coils has moved above the old position of the plasma and the eddy currents are not playing a big role any more.

Until now only the EFC coils have been playing a role in vertical feedback control. The reason for this, besides the fact that the other coils involved with vertical control (primarily the OH2 coils) are slower to respond, is that, for these shots, much smaller gains are used in the slow Z–position control channel, which drives the OH2 coils, than in the fast Z–position channel. The intermediate equilibrium mentioned above cannot last since the error in $I_p Z_{ma}$ is non–zero and there is another feedback channel (the slow Z–position channel) trying to control it. Eventually the OH2 coils reduce the error in Z–position to zero and bring the EFC current back to its normal bias value.

Using the method described in Chapter 5, the equilibrium was reconstructed at a time long enough after the step that the plasma had settled in its new position; typically 50 msec after the step. The perturbed equilibrium procedure was applied then to get the open–loop plasma response. Table 6.2 shows shot number, time in the shot and the calculated open–loop growth rates for ten such cases. Then, the procedure outlined in Section 6.1 was used to find the closed–loop eigenmodes. The vertical mode was identified in order to be compared to observed behavior. In essence, we have a closed–loop stable plasma and we see how it behaves when it is pushed 1 cm above or below its equilibrium position. Table 6.3 shows the theoretical and experimental growth rates and oscillation frequencies for the ten

case	shot number	time (msec)	theoretical open–loop growth rate (1/sec)
1	940527020	700	148.9
2	940624003	800	286.8
3	940624003	860	140.9
4	940624005	800	256.0
5	940624005	860	184.7
6	940624005	900	174.7
7	940624009	800	293.1
8	940624014	800	316.6
9	940624014	900	171.6
10	940624017	800	319.5

Table 6.2: Open–loop growth rates calculated theoretically for ten cases with step perturbations.

case	theoretical closed–loop growth rate (1/sec)	theoretical closed–loop oscillation frequency (rad/sec)	experimental closed–loop growth rate (1/sec)	experimental closed–loop oscillation frequency (rad/sec)
1	-240.2	315.6	-112.6	396.8
2	-226.4	465.3	-126.7	788.8
3	-194.5	363.8	-114.9	309.0
4	-341.2	537.4	-150.5	673.5
5	-232.0	435.2	-216.9	376.6
6	-279.5	447.9	-249.1	625.4
7	-289.1	534.2	-164.9	762.4
8	-322.3	554.1	-135.6	731.8
9	-235.5	434.8	-242.2	749.1
10	-304.2	522.1	-216.0	795.0

Table 6.3: Comparison of theoretical to experimental closed–loop eigenvalues for the ten cases considered in this chapter.

cases of Table 6.2. The experimental values were derived as follows: Looking at the Z–position trace in Fig.6-10, we see that, after each step, the Z–position first follows a strongly damped oscillation and then settles into an intermediate phase where the final Z–position has not been reached yet, because the slow Z–controller has not had an effect yet. During this time there is some fluctuation in Z–position but it is not clearly an oscillation, hence not a phenomenon that could be reproduced by the linear model. As a result, a fit to a single exponential was made only to the initial damped oscillation according to the formula:

$$Z(t) = a_0 + e^{\gamma t}(a_1 sin(\omega t) + a_2 cos(\omega t)) \tag{6.14}$$

Here, $a_{0,1,2}$ are fitting parameters, while γ and ω are the growth rates and oscillation frequencies listed in Table 6.3. A typical fit is shown in Fig. 6-12. The information in Table 6.3 also portrayed graphically in Figs. 6-13 and 6-14. The error bars were

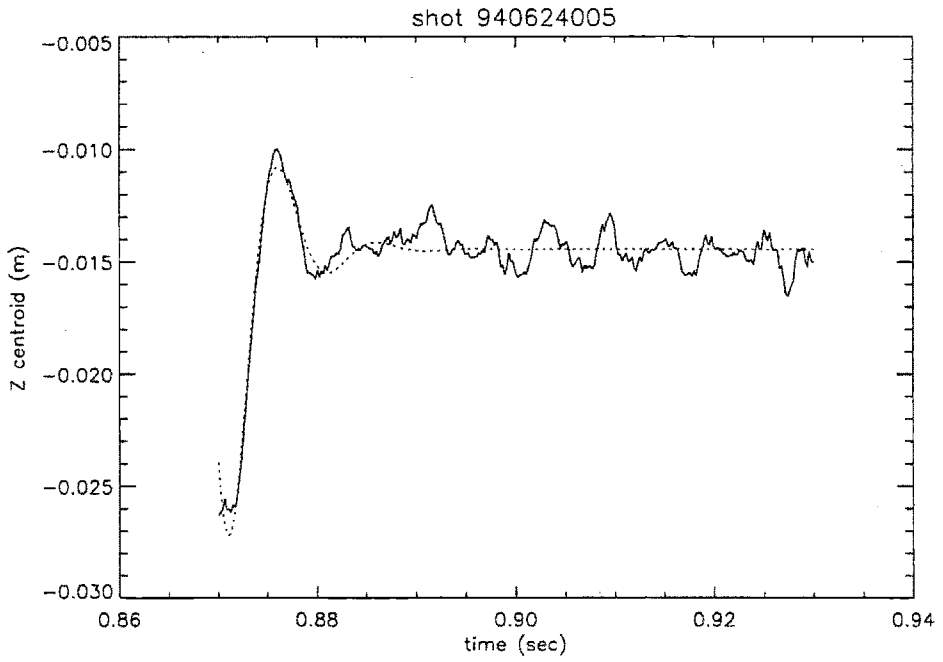

Figure 6-12: Z–position trace during a step change (solid line) and fit to the initial behavior (dotted line).

obtained by doing the calculation with 25% more and 25% less overall controller

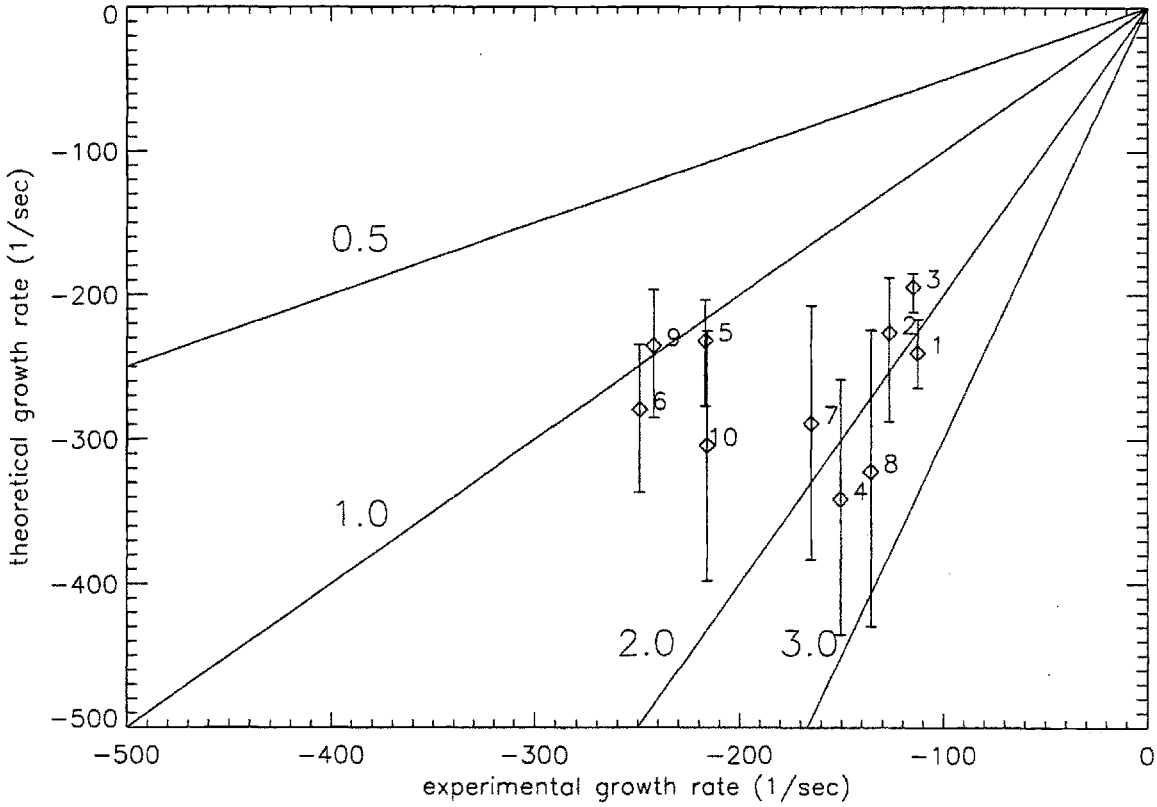

Figure 6-13: Comparison of theoretical to experimental closed–loop growth rates for the ten cases considered in this chapter. The lines through the origin of slope 1/2, 1, 2, and 3 are shown.

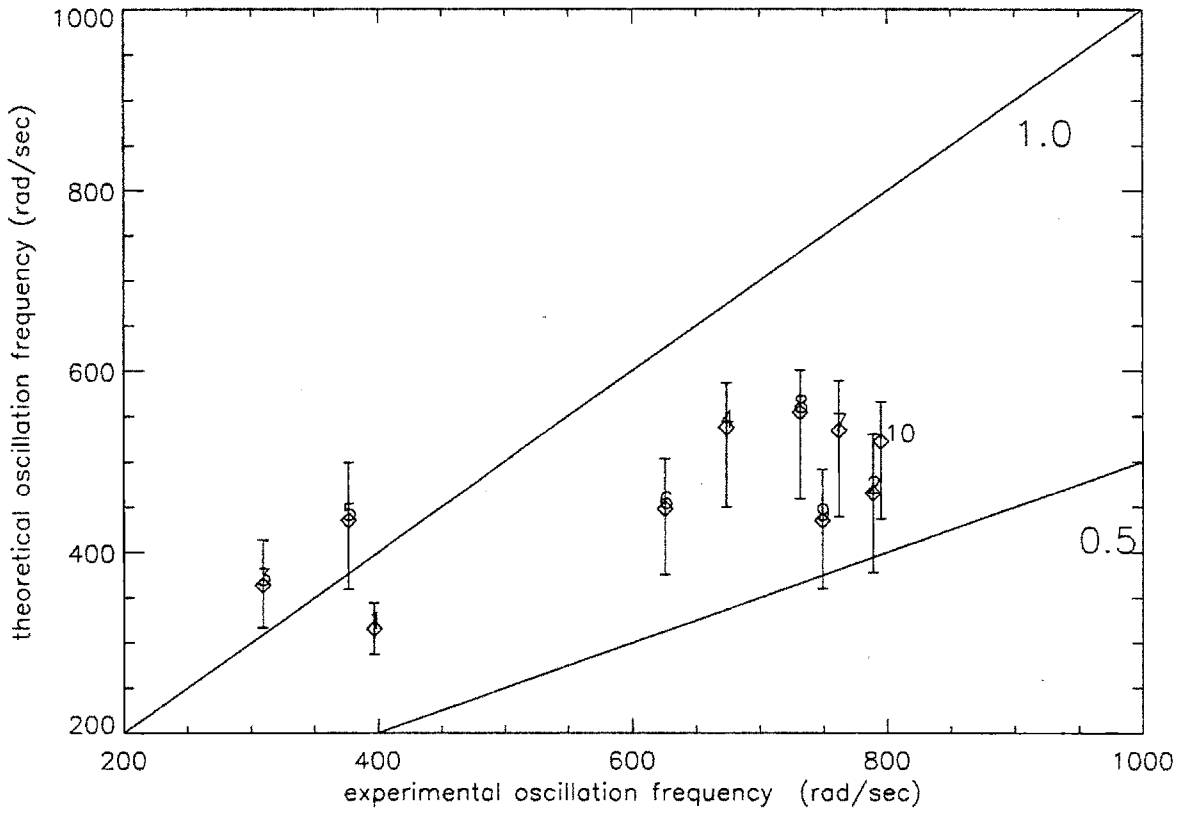

Figure 6-14: Comparison of theoretical to experimental closed-loop oscillation frequencies for the ten cases considered in this chapter. The lines through the origin of slope 1/2 and 1 are shown.

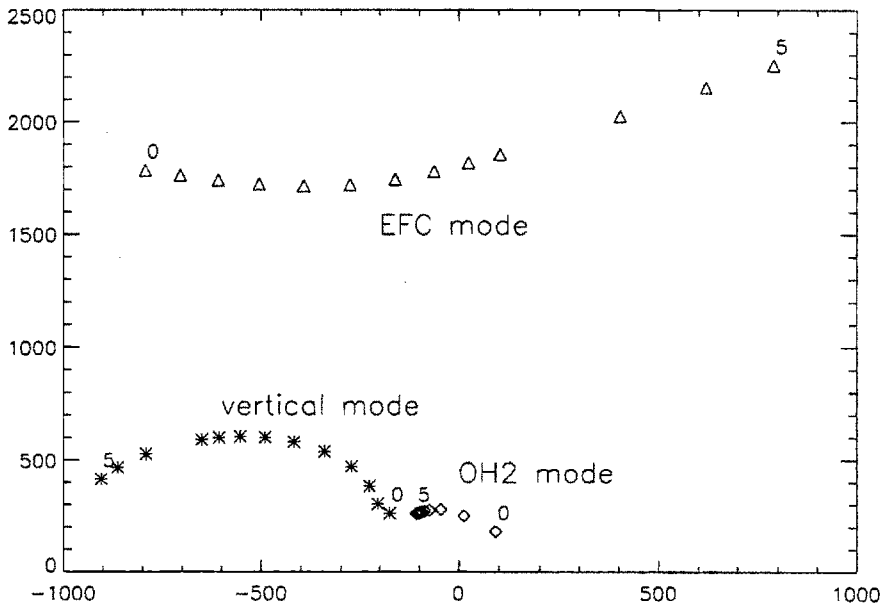

Figure 6-15: Root locus of one EFC power supply mode (triangles), one OH2 power supply mode (diamonds), and the vertical mode (stars) as controller gain to the EFC power supply is varied from zero to five.

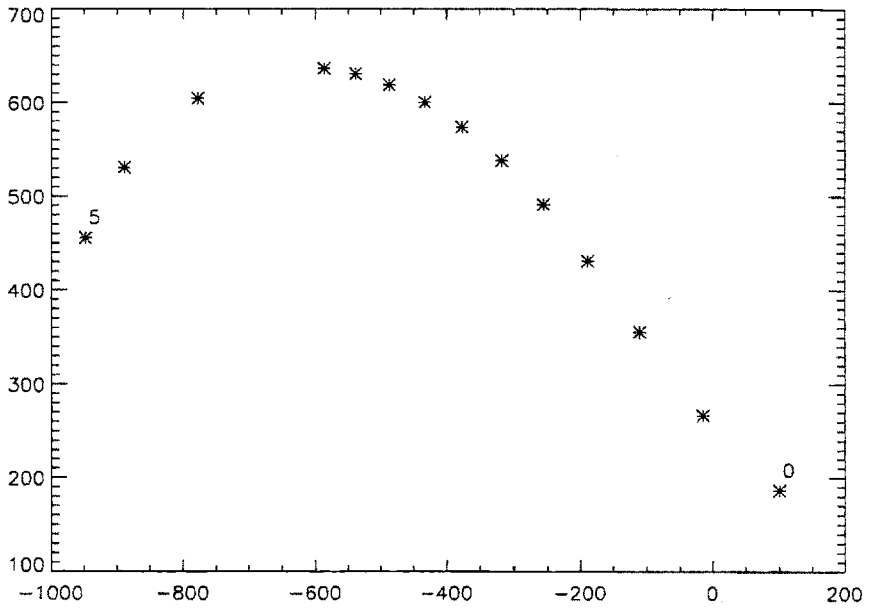

Figure 6-16: Root locus of the vertical mode as controller gain to the EFC power supply is varied from zero to five neglecting all power supply dynamics.

gain to the EFC power supply than what was used in the experiment. Note that these error bars are correlated: as the growth rate moves along the error bar in such direction as to approach the line of slope one, the oscillation frequency moves in a direction away from it. This can be seen more explicitly in Figs. 6-15 and 6-16. Fig. 6-15 shows the root locus of the vertical mode, one of the EFC power supply modes and one of the OH2 power supply modes as the controller gain to the EFC power supply is varied by a factor of zero to five times what was used in the experiment. The power supply modes shown are the only power supply related modes affected by this gain scan. As the gain is increased, the eigenvalue of the OH2 mode converges to the value that it has when the power supply is not connected to the rest of the system. This was also seen in one of the earlier shots with persistent oscillations (Fig. 6-5). What is different from those shots is the behavior of the vertical mode: as the gain is increased the vertical mode becomes more stable, whereas in Fig. 6-5 it turned around and became unstable. Also, as the gain increases, the EFC mode becomes unstable, but its frequency is higher than anything observed experimentally. Fig. 6-16 shows the root locus of the vertical mode as the EFC controller gain is varied, assuming perfect power supplies. The behavior is similar to that of Fig. 6-15 indicating that it is not due to some interaction with a power supply mode. This behavior is observed in all shots with steps in the Z–position. The reason for the differences in the root loci of the vertical mode for the two cases in Fig. 6-5 (shot 930923019) and Fig. 6-15 (shot 940624005) is that in earlier shots (as in Fig. 6-5) no derivative gain was used in the fast Z–position feedback channel. Indeed, if the calculation for shot 930923019 is redone with an artificial derivative gain equal to what was used in shot 940624005, the resulting root locus changes to look more like that of Fig. 6-15 (see Fig. 6-17). A similar variation of the controller gain to the OH2 power supplies produces negligible variation in the eigenvalues.

From Fig. 6-13, it can be concluded that the model gives a more damped closed–

loop system than observed, approximately by a factor of two. From Fig. 6-14, we see that the oscillation frequency is predicted correctly by the model to within a factor of two. In this figure, two clusters of points can be discerned: one in the 700 rad/sec experimentally observed frequency area and one in the 400 rad/sec area. This second set (cases 1, 3, and 5) are equilibria that seem to be more open–loop stable to begin with (see Table 6.2).

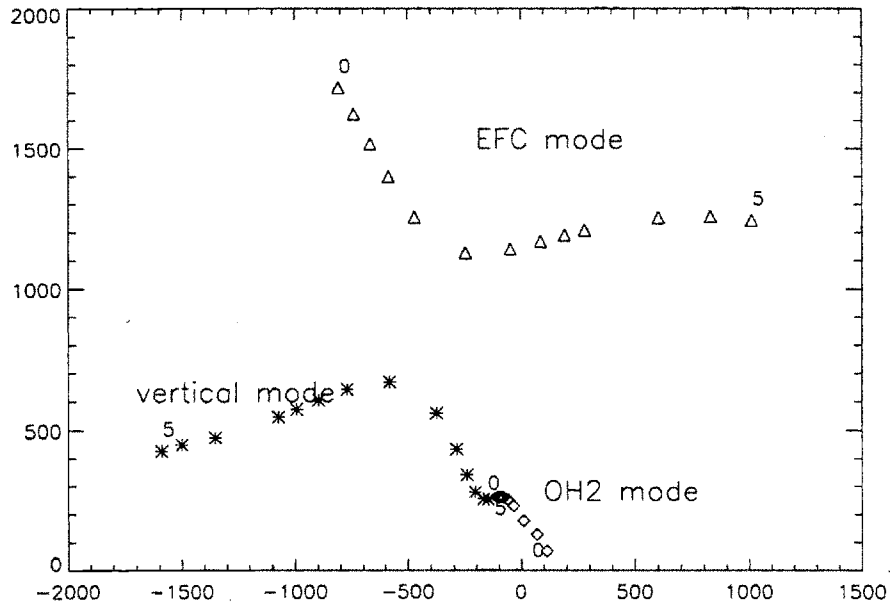

Figure 6-17: Root locus of one EFC power supply mode (triangles), one OH2 power supply mode (diamonds), and the vertical mode (stars) as controller gain to the EFC power supply is varied from zero to five. This is shot 930923019 with fast Z–control derivative gain from shot 940624005.

One of the things that was to be studied on the run day on which the above experiments were performed (and possibly on additional ones) was the effect of feedback gains on closed–loop behavior. Unfortunately, the malfunction of the OH2L coaxial cable, ended the run day and the run period before any such gain scan could be accomplished. It was also seen in the previous section that this is essential to determine what causes the ubiquitous 50–120 Hz oscillation and how to suppress it.

6.4 Nonlinear Simulations

As was mentioned in the previous section, saturation of the demand signal to the power supplies can be a source of nonlinear behavior. In this section we examine to what extent it can explain the discrepancy between experimentally observed behavior and theoretically predicted behavior based on linear models.

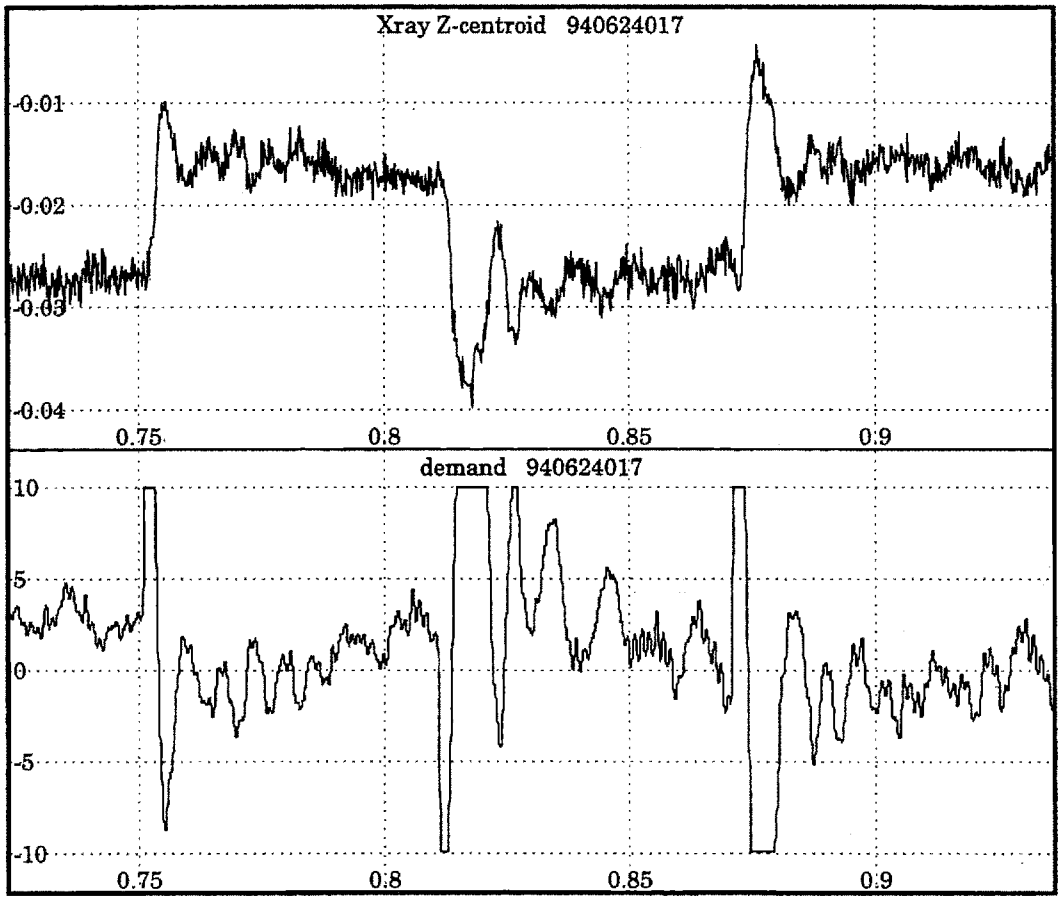

Figure 6-18: Z–position of the plasma current centroid (top) and demand signal (bottom) to the EFC power supply showing the saturation effect.

Fig. 6-18 shows the demand signal to the EFC power supply for one of the shots mentioned in the Section 6.3. At each step in the requested I_pZ_{ma}, there is a spike in the error in I_pZ_{ma} (see Fig. 6-10), which, when multiplied by the appropriate elements of the **P**, **I**, **D**, and **M** matrices produces a demand signal to the EFC

which is larger than the value that the signal transmission hardware can handle. It is, therefore, clipped off at the maximum value allowed by the hardware. All of the shots mentioned in the previous section have some saturation. The shots that were analyzed stayed saturated for approximately 3 msec. Shots with longer intervals of saturation were not analyzed because of their highly nonlinear nature.

We can look at the demand signal saturation effect by looking at a simulation of the time evolution of the system. Once the matrices **A**, **B**, and **C** have been determined, the state and output equations determine the time evolution of the linear system with the appropriate inputs and initial condition. The steps in $I_p Z_{ma}$ which were injected in the shots considered on the previous section can be handled in two equivalent ways:

- one can choose as operating point the equilibrium at some time after the step when the plasma has settled in its new position. $\vec{u}(t)$ is then given by Eq. 6.6. The initial condition is then non–zero. One can reconstruct the equilibrium right before the step and take the difference between the two equilibria to be the initial condition.

- one can choose as operating point the equilibrium right before the step. The initial condition is then zero, but the input is:

$$\vec{u}(t) \equiv \vec{u}_{linear}(t) = -\mathbf{M}\left(\mathbf{P}\mathbf{A}_p\vec{y} + \mathbf{I}\mathbf{A}_p\int_t \vec{y}dt' + \mathbf{D}\mathbf{A}_p\dot{\vec{y}}\right) - \\ - \mathbf{M}\left(\mathbf{P}\vec{Z}_{ref} + \mathbf{I}\int_t \vec{Z}_{ref}dt' + \mathbf{D}\dot{\vec{Z}}_{ref}\right) \qquad (6.15)$$

  where $\vec{Z}_{ref}$ is a vector containing the reference inputs for the quantities which are being fed back on. In this case, $\vec{Z}_{ref}$ only has nonzero values for the elements corresponding to $I_p Z_{ma}$.

Let us adopt the second approach. The effect of the demand signal saturation can be added by using as input:

$$\vec{u}(t) = \begin{cases} \vec{u}_{linear}(t) & if \quad |\vec{u}_{linear}(t)| < \vec{u}_0 \\ \vec{u}_0 & if \quad |\vec{u}_{linear}(t)| \geq \vec{u}_0 \end{cases} \tag{6.16}$$

where $\vec{u}_0$ is a vector containing the maximum absolute values of the demand signals allowed by the hardware and $|\vec{u}_{linear}(t)|$ denotes a vector consisting of the absolute values of the elements of $\vec{u}_{linear}(t)$. The solution to the state and output equations is given in Eq. 4.3. Using $\vec{x}(t = t_0) = \vec{0}$ and $\vec{u}(t)$ as prescribed by Eq. 6.16, we get the evolution of the state as a function of time and from it the evolution of the Z–position.

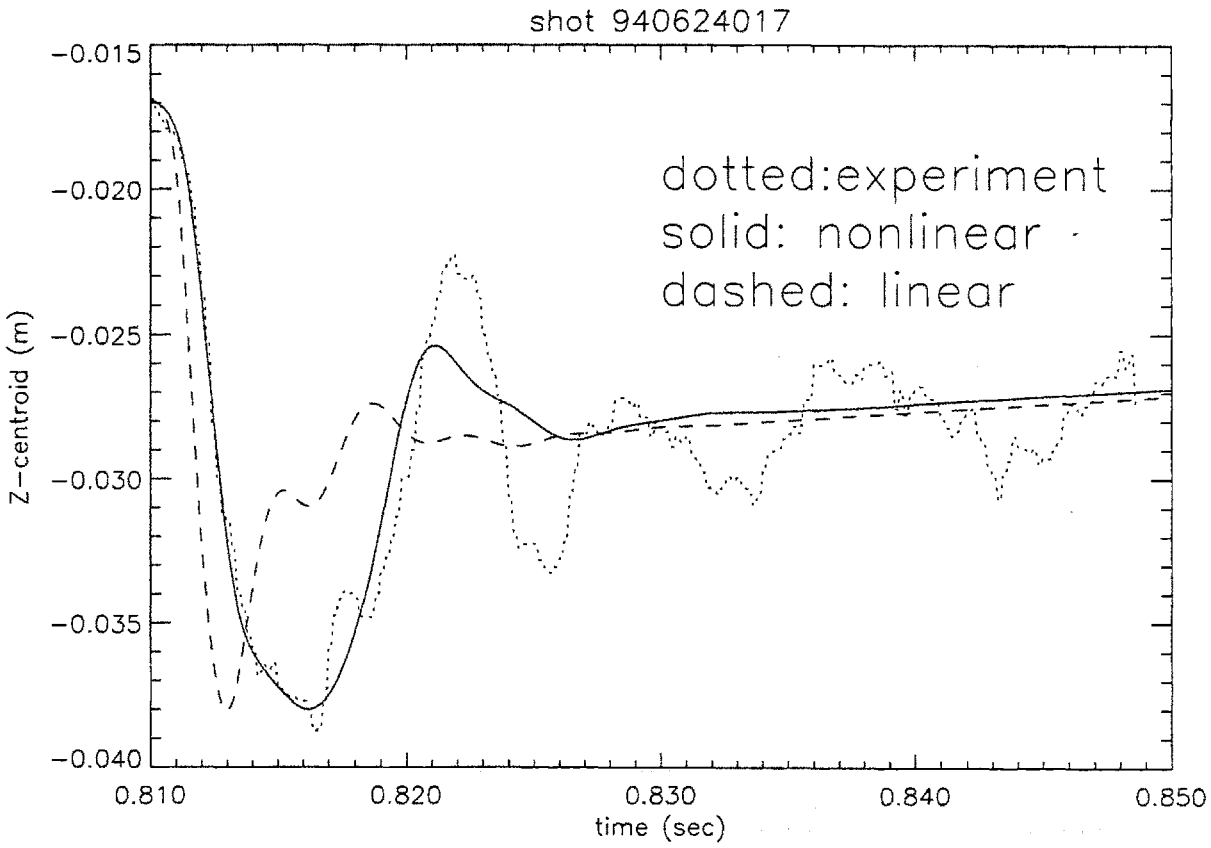

Figure 6-19: Vertical position after a step as measured (dotted), and as calculated by means of a linear (dashed) and a nonlinear (solid) simulation.

This procedure was carried out for the shots of Table 6.2. The results for one case are shown in Figs. 6-19 and 6-20. The linear response model assumes that any

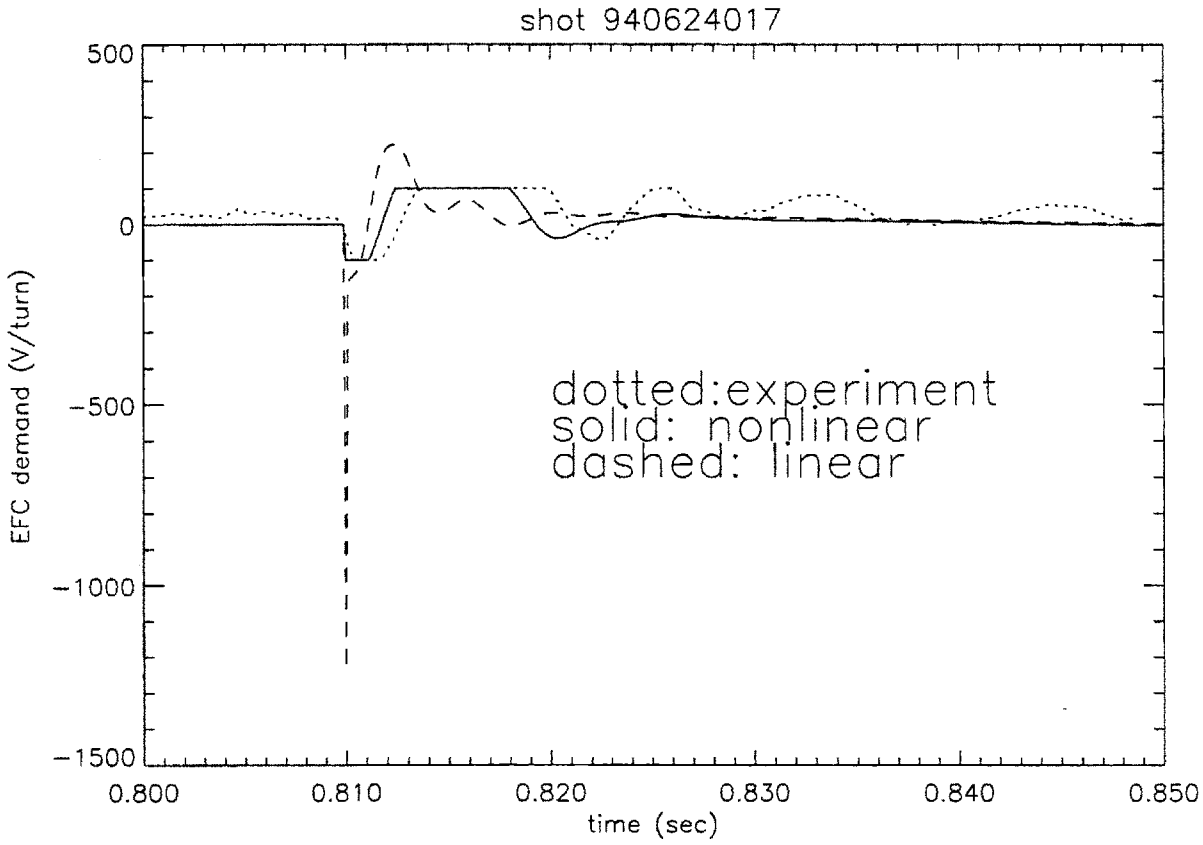

Figure 6-20: Demand signal to the EFC power supply after a step as measured (dotted), and as calculated by means of a linear (dashed) and a nonlinear (solid) simulation.

amount of demand signal to the EFC power supply is attainable. Therefore, when the step in $I_p Z_{ma}$ is applied, it immediately asks the EFC power supply for a very large amount of voltage. This is the 1300 Volt/turn spike seen in Fig. 6-20. Note that the EFC power supply cannot deliver more that 100 Volts/turn and the signal processing hardware is calibrated so that the maximum demand signal corresponds to the maximum output voltage of the power supply. If the hardware were able to deliver the 1300 Volt/turn spike in the demand signal, the Z–position would go to its requested value much more quickly that it actually does (see Fig. 6-19). From Fig. 6-19 we can see that the time evolution without the saturation effect suggests an oscillation frequency larger than the observed one. In the previous section, however, we saw that the theoretically predicted oscillation frequency was usually smaller than the observed one. What was listed as theoretically predicted oscillation frequency in the previous section was that of the vertical mode. There is an EFC mode, though, with an oscillation frequency at approximately 1700 rad/sec which seems to be what is governing the time evolution in the absence of the saturation effect. In other words, the response is determined essentially by the dynamics of the EFC power supply, because of the very large demand. If we do not allow the demand to the EFC power supply to exceed 100 Volts/turn, the demand signal stays saturated for a long time and the Z–position takes longer to reach its desired value. This nonlinear simulation looks much more like the measured response than the linear simulation.

In order to make some contact with Figs. 6-13 and 6-14, an oscillating exponential was fitted to the initial part of the nonlinear simulation of the time evolution of the Z–position in the same way as an exponential was fitted to the measured Z–position in Fig. 6-12. The results are shown in Figs. 6-21 and 6-22. The agreement between theory and experiment is much better than in Figs. 6-13 and 6-14, namely to within 50%.

We can conclude from this section, that the nonlinear effect of the saturation

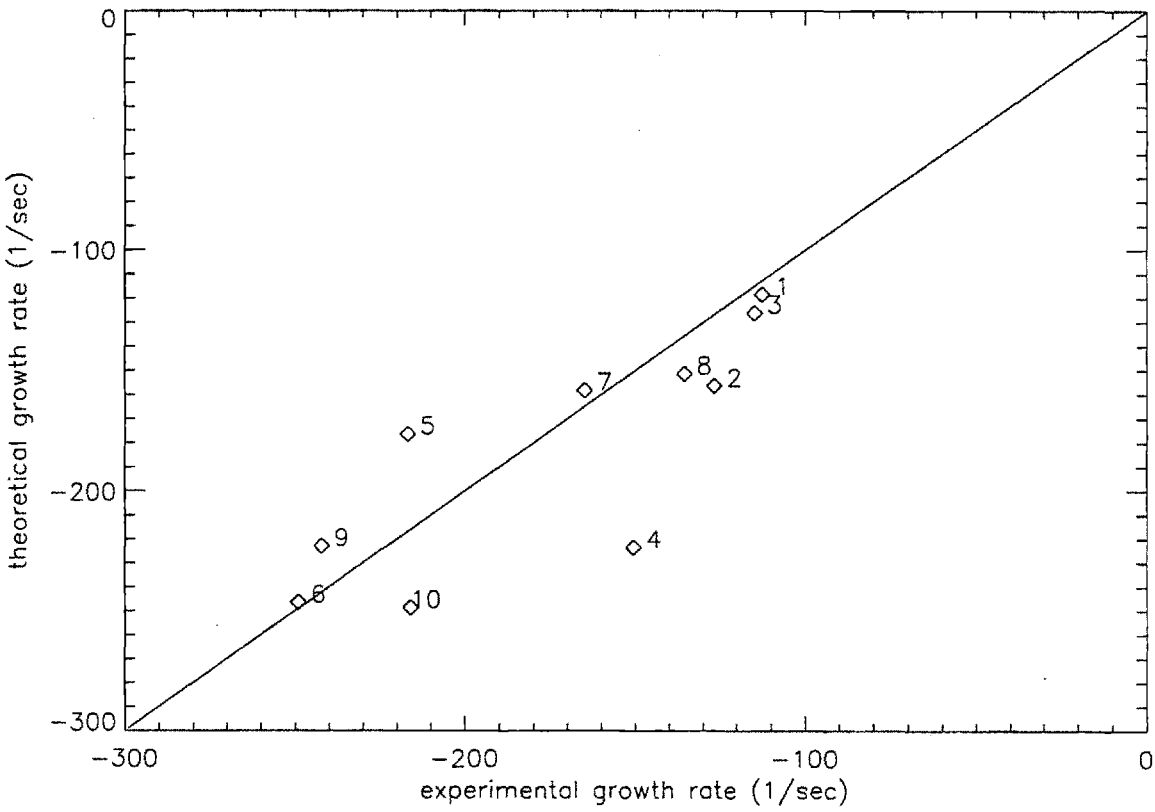

Figure 6-21: Comparison of theoretical to experimental closed-loop growth rates for the ten cases considered in this chapter. The line through the origin of slope one is shown. Theoretical growth rates were derived from the nonlinear evolution.

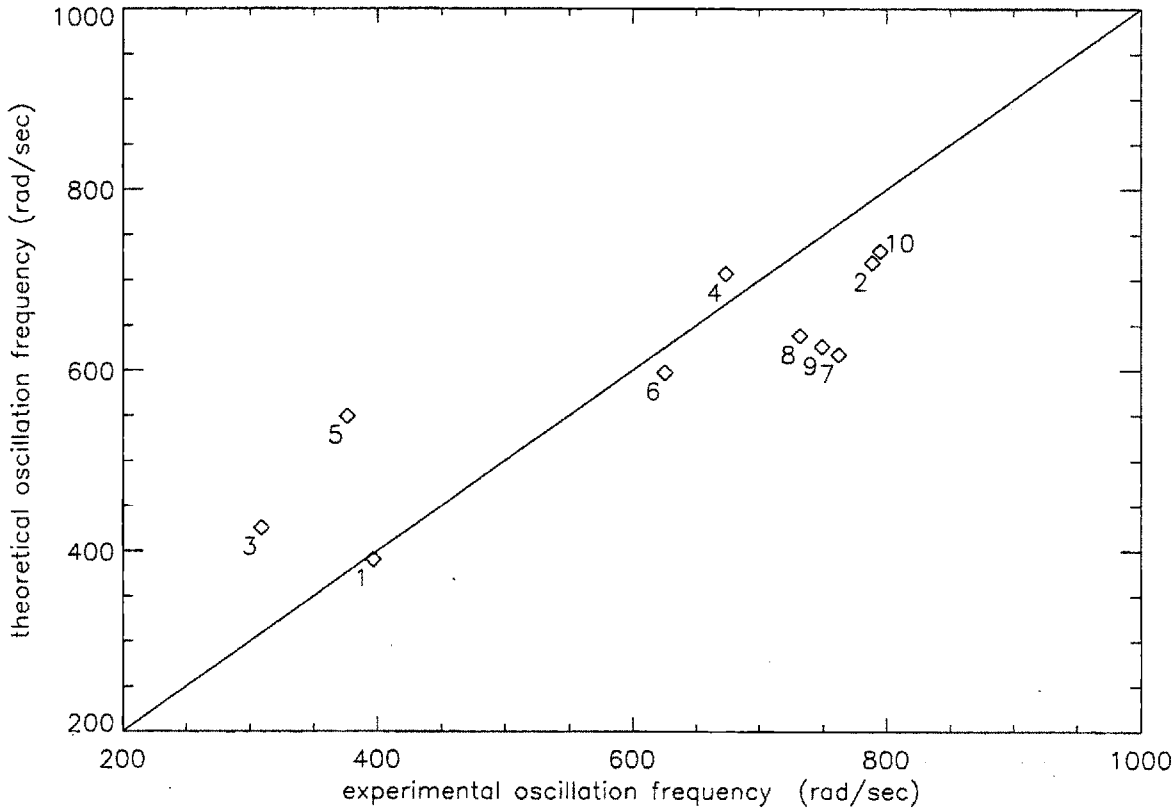

Figure 6-22: Comparison of theoretical to experimental closed–loop oscillation frequencies for the ten cases considered in this chapter. The line through the origin of slope one is shown. Theoretical oscillation frequencies were derived from the nonlinear evolution.

of the demand signal goes a long way towards explaining the discrepancy between theoretical and experimental growth rates and oscillation frequencies.

Chapter 7

Summary and Conclusions

Elongated plasmas are inherently unstable and present, therefore, a challenge as far as control of plasma shape and position is concerned. Until now, control of tokamaks has been carried out largely in a trial–and–error fashion. The reason for this lies mainly in hardware limitations. The hardware necessary for feedback control on the timescale of the vertical instability has been of an analog nature offering very little flexibility. Recent technological advances have made more flexible feedback control computers available. An example is the Alcator C–Mod hybrid analog–digital control computer which offers the fast response of analog signal processing with the flexibility of digital programming of the feedback gains. Digital feedback computers that are fast enough for tokamak control have also recently become available, making it possible to use frequency dependent feedback gains. This new technology allows us to exploit some powerful methods of modern control theory for more effective and efficient tokamak control. All these methods, however, presuppose the existence of some linear model of the system to be controlled. The existence of a model is not necessary if the feedback gains are determined by trial and error. Many models of plasma response already exist with a wide range of complexity. Before modern control theory can be used, however, for designing

feedback control laws, the models upon which the control laws are based have to be tested. So far, little has been done in the area of testing linear plasma response models against experimentally observed behavior. The only published comparisons of theory to experiment involve rigid filament representations of the plasma.

This work has attempted to make a comparison between more sophisticated theory and experiment using data from the Alcator C–Mod tokamak. A linear model for each subsystem of the closed–loop system constituting an Alcator C–Mod discharge under feedback control has been constructed. No new theories have been developed here. The following aspects of the study, however, are original:

- A non–rigid, approximately flux–conserving, perturbed equilibrium plasma response model was used in the comparison to experiment.
- A detailed toroidally symmetric model of the vacuum vessel and the supporting superstructure was used.
- Modeling of the power supplies feeding the active coils has been included.
- Experiments were conducted with vertically unstable plasmas where the feedback was turned off and the plasma response was observed in an open–loop configuration. Such experiments have not been performed previously on other tokamaks because of the danger of disruptions associated with them.
- Nonlinear simulation of the time evolution of the closed–loop experiments was done in an effort to account for the discrepancies between linear theory and experiment.

The agreement between theory and experiment in the open–loop configuration was very satisfactory, proving that the perturbed equilibrium plasma response model and a toroidally symmetric electromagnetic model of the vacuum vessel and the structure can be trusted for the purpose of calculations for control law design.

When the power supplies and the feedback computer hardware are added to the system, however, as they are in the closed–loop configuration, they introduce non-linearities that make it difficult to explain observed behavior with linear theory. A recapitulation of the major points and conclusions of each chapter follows as a well as some suggestions for further work.

7.1 Linear Plasma Response Models

When studying axisymmetric modes of plasma behavior in the presence of resistive conductors for the purpose of axisymmetric control, the assumption can be made that the timescale of plasma response is of the same order as the L/R time of the conductors, which is much longer than the Alfvén timescale characteristic of MHD phenomena. The plasma inertia can then be ignored and the plasma can always be assumed to be in equilibrium, moving from one equilibrium state to another very slowly. The law that determines how the equilibrium moves from one equilibrium state to another is the circuit equation of the conductors around the plasma. The plasma response can then be represented as an additional inductance matrix, $\mathbf{X}$, in this circuit equation describing the mutual coupling of these conductors as mediated by the plasma. A linear plasma response model is simply a prescription for $\mathbf{X}$. Two methods have been described for obtaining $\mathbf{X}$: the filament model and the perturbed equilibrium model.

In the filament model, the plasma is represented as a rigid set of current carrying filaments that can only move vertically. These filaments are added to the circuit equation of the conductors around the plasma with the assumption that their current does not change. The flux at the conductors is only affected by the change in mutual inductance as the filaments move. The massless–plasma assumption allows one to equate the force on the filaments due to the eddy currents induced in the conductors to the Lorentz force the filaments experience as they move through the

unperturbed magnetic field due to the conductors and solve for the Z–position of the filament set. Substituting the Z–position into the circuit equation gives the **X** matrix.

In the perturbed equilibrium model, a base plasma equilibrium is calculated using a free–boundary equilibrium code and used as the operating point of the linear response model. If all the coil current inputs to the equilibrium code are perturbed one by one by a small amount and the code is run again, a set of perturbed equilibria is obtained that span the space of plasma motion, i.e., the plasma is always a linear combination of this set of perturbed equilibria. If the flux at the conductor locations is one of the outputs of the equilibrium code, the **X** matrix can be defined as a matrix giving the change in flux at one conductor location due to the plasma alone due to the change in current in another conductor. The vacuum vessel and structure response can be "folded in" with no additional computational cost by assuming that a set of vessel/structure currents can be represented by a set equivalent coil currents. Furthermore, by perturbing two inputs of the equilibrium code pertaining to the plasma current profile, two constraints for approximate flux conservation can be satisfied. We thus have a non–rigid, not necessarily vertical, approximately flux conserving linear model which is a much less constrained representation of the plasma/conductor system than the filament representation.

7.2 Modeling of the Structure and the Power Supplies

The vacuum vessel and the structure have been split into 190 toroidally symmetric elements. Their mutual inductances and resistances have been estimated theoretically on the basis of geometry and materials properties. Their inductances and Green's functions to the magnetic diagnostics and to the a grid in the plasma re-

gion have also been calculated. Toroidal asymmetries like ports are the weak point of this model. The model has been tested by putting step currents into the coils. The magnetic measurements as a function of time were predicted theoretically using the circuit equation and compared to the actual measurements. The agreement was to within 10%, which is better than any published comparison of this kind.

The power supplies feeding the coils are very nonlinear devices and no attempt was made to model them from first principles, since this would involve modeling large arrays of thyristors. Instead, linear transfer functions have been determined empirically by injecting oscillations of various frequencies into the demand signal to the power supply. Then, by looking at the output of the power supply, we get a few points of gain as a function of frequency and phase as a function of frequency through which a transfer function can be fitted. Due to lack of time, the demand signal oscillations were only of a single amplitude. The effect of amplitude on power supply dynamics was not investigated. It is possible that power supply dynamics are different at different amplitudes.

7.3 Model Reduction

We have described and investigated two types of general model reduction schemes, based on eigenmodes or Hankel singular modes respectively. In application to the axisymmetric electromagnetic model of Alcator C–Mod, we find that two additional factors are also of importance, namely whether or not a plasma is included in the model during reduction, and whether the passive elements can be partitioned in such a way as to guarantee retaining the important modes of the vacuum vessel.

Reduction of the entire system using the Hankel singular modes can be achieved down to dimension 40 with negligible error and to dimension 10 with probably acceptable accuracy. In contrast, retaining even 40 of the slowest eigenmodes leads

to large errors in the system response. Plainly, case-by-case analysis of a specific complete system, for example to study optimum feedback control algorithms, will benefit greatly from model reduction using the HSM approach. The eigenmode decomposition is unsuccessful in its direct form.

An intuitive partitioning of the passive structure into separate vacuum vessel and structure allows one to obtain successful reduction using the eigenmode technique as well as HSM. However partitioning requires the use of more or less ad hoc judgement about which elements to include in which partition. It may not always be straightforward to make this judgement effectively. In our example, where partitioning is rather natural, we still need to retain between 10 and 20 vessel modes to obtain accuracy of 10% or better in the open-loop system response and unstable mode growth rate (30 when using HSM without generic plasma).

In reducing the passive elements alone, which is convenient because it allows the reduction to be done once and for all, it is very advantageous to include a generic plasma. This enables the HSM approach to obtain 10% accuracy with between 10 and 20 passive modes both with the partitioned and the unpartitioned model. Roughly twice as many are required with no generic plasma. In all the cases we have run, we have been able to adequately represent the full (vertically unstable) model with a smaller number of modes than when using no generic plasma at all, provided the generic plasma had some elongation.

The eigenmode reduction also benefits from the inclusion of a generic plasma, when partitioning is used. However, it obtains only about 20% accuracy without partitioning and this does not improve even adding up to 60 modes. This limited accuracy is likely to be even worse for larger differences between generic and actual plasmas. If a vertically stable generic plasma were chosen, for example, there would be little or no improvement over the no-plasma eigenmode reduction. What appears to happen is that the unstable generic plasma forces the inclusion of one mode dominated by the vessel (namely the unstable mode). This single vessel mode

differs from the actual unstable mode (unless one is dealing with exactly the generic plasma) by enough to cause significant errors.

We conclude that accurate axisymmetric control modeling based on system reduction by selecting the slowest eigenmodes is possible in situations where retention of the important modes is guaranteed either by system simplicity or by appropriate partitioning. The more complex HSM reduction technique can handle situations where eigenmode reduction fails but it offers no clear quantitative advantage in situations to which eigenmode reduction is well suited. Neither technique gives a quantitatively accurate representation of Alcator C–Mod with fewer than between 10 and 20 significant modes.

7.4 Open Loop Tests

After having gained confidence in the electromagnetic model of the vacuum vessel and structure, the model of the plasma response in the presence of these conductors was tested in an open–loop configuration, so that the power supplies and the plasma control computer (PCC) were not in the picture. After establishing an elongated plasma, the feedback was turned off for a brief interval and the plasma started moving up– or downwards. Fitting the evolution of the vertical position of the plasma current centroid to an exponential, a growth rate was obtained.

The plasma equilibrium shortly before the feedback was turned off was reconstructed. Two methods can be used for the equilibrium reconstruction: 1) a fitting method using only the magnetic diagnostics information at the time of interest and 2) a method based on the circuit equation which does not use the magnetic diagnostics, but uses the time history of all coil currents up to the moment of interest. The two methods give similar results but the second gives more physical distributions of eddy currents in the passive conductors.

Analysis of the response of these equilibria using both the filament and the perturbed equilibrium model gave only one unstable mode which was of an almost purely vertical nature. The eigenvalue of this mode was compared to the experimentally observed growth rate. The growth rates predicted by the filament model were significantly lower than the observed ones. This was expected, since the assumptions that go into the filament model constrain the allowable modes of response. The growth rates predicted by the perturbed equilibrium model were fairly close to the observed ones, within 30%. These tests proved that the electromagnetic model of the conductors combined with the perturbed equilibrium model of the plasma were able to predict linear plasma response satisfactorily when other dynamics – like the power supplies – are absent.

7.5 Closed Loop Tests

To model the entire closed–loop system one has to feed the output of the power supply model to the input of the plasma/conductor system. Then, the output of the plasma/conductor system is led through the feedback gains, as these are read from the PCC hardware, to the input of the power supply model. Performing eigenmode analysis on the closed–loop system gives no unstable mode; hence, one has to look at the modes carefully do discern the vertical eigenmode. In the closed–loop configuration, this vertical mode usually has a complex eigenvalue.

In some discharges dedicated to studying closed–loop behavior of elongated plasmas, steps in the desired (reference) $I_p Z_{ma}$ were injected. As the plasma moved to its new position, it overshot and displayed some oscillating behavior. The vertical position of the plasma current centroid was fitted to an oscillating exponential and the resulting growth rate and oscillation frequency were compared to the eigenvalue of the vertical eigenmode. The agreement was not satisfactory; it was to within a factor of two.

In an attempt to explain the discrepancy between theory and experiment, it was investigated how the theoretical eigenvalues change with a change to the overall gain of the demand signal to the EFC power supply. Even though the theoretical eigenvalues were affected considerably, this gain variation was not enough to explain the discrepancy.

Saturation of the demand signal to the EFC power supply was present in all closed–loop test shots. This is not a linear effect, and cannot be included in the eigenmode analysis of the closed loop. It can, however, be studied when we try to simulate the time evolution of the system from some initial condition. Then, we can require, that the input to the system does not exceed a certain value. Simulations without the saturation effect show that, when the step in the $I_p Z_{ma}$ reference signal is applied, a very large demand is sent to the power supply which brings the plasma to its new position quickly, in a time determined mainly by the power supply dynamics. Simulations with the saturation effect, however, show an evolution of the vertical position of the plasma which closely matches the experimentally observed one. The nonlinear effect of the saturation of the demand signal was able to explain to a large extent the discrepancy between theoretical and experimental eigenvalues.

7.6 Suggestions for Further Work

The Alcator C–Mod run time devoted to this work has been limited. Some more work should be done in the future to fill in the gaps. This work should concentrate in two areas: power supply characterization and closed–loop tests.

The power supply dynamics were empirically determined at one amplitude only. More power supply characterization shots like those described in Chapter 3 should be run with the amplitude of the oscillations varying. Since the power supplies are very nonlinear devices, it is impossible to come up with a linear model of general

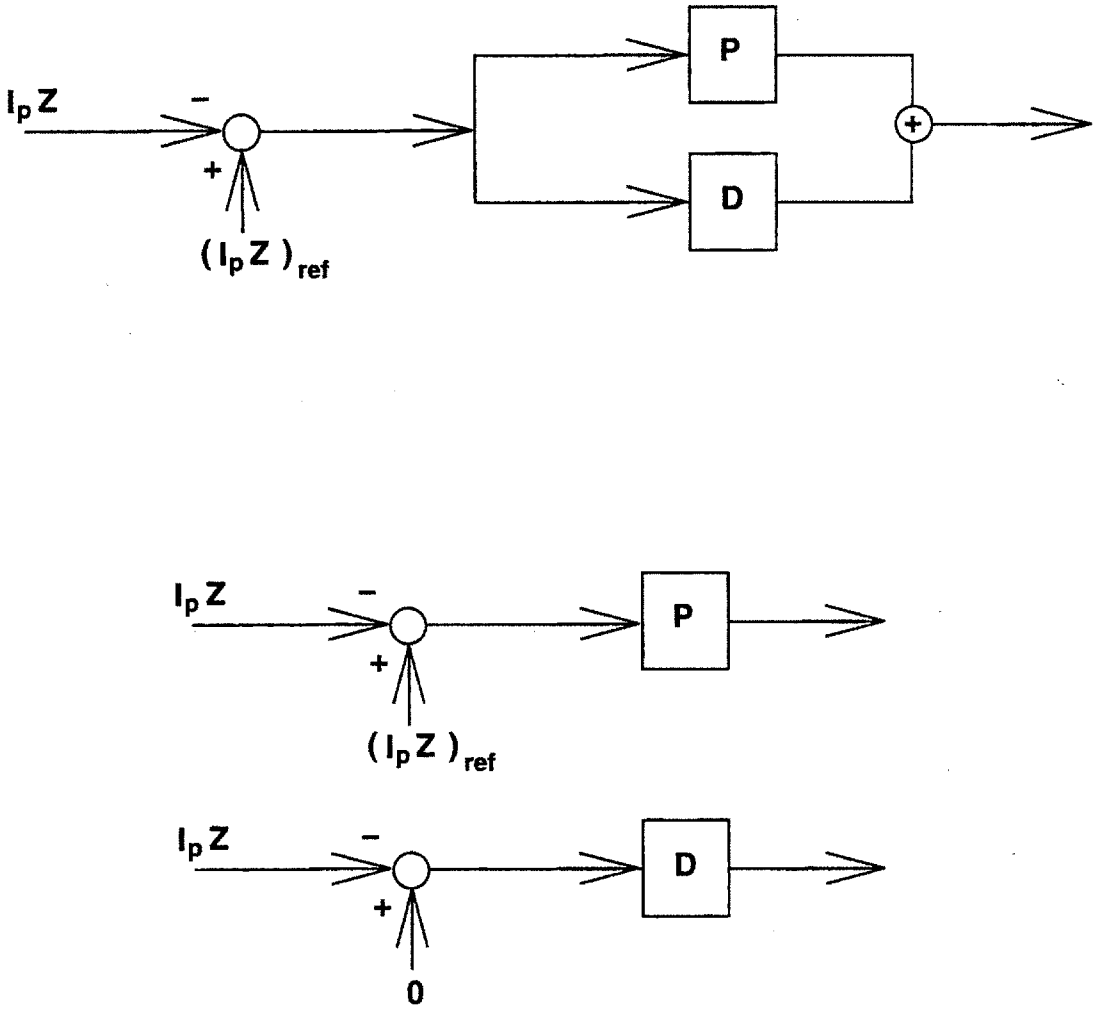

Figure 7-1: Implementation of the step in the reference $I_p Z_{ma}$ using one channel (top) and two channels (bottom).

validity, but we can have a "library" of linear power supply models valid at different amplitudes which can be applied to different cases.

One problem that plagued the closed–loop tests was the nonlinearity introduced by the saturation of the demand signal to the EFC power supply. This saturation was present in all these shots and was mainly due to the step in the I_pZ_{ma} reference signal going through the derivative part of the I_pZ_{ma} feedback channel. The top part of Fig. 7-1 shows how the step was implemented in the shots from Chapter 6. The I_pZ_{ma} signal is subtracted from the reference signal and the difference goes through both the proportional and the derivative gains. In order to avoid the spikes in the demand signals, it would be better to implement the steps using two feedback channels as shown in the bottom of Fig. 7-1. The I_pZ_{ma} signal should go into two channels, one of them only with proportional gain and the other only with derivative gain. The reference signal with the step should go only into the channel with the proportional gain. The output of the sum of the two channels will be the same as the output of the one channel of the present implementation except during the 1 msec of the step change. This implementation should help avoid the saturation effect.

Unfortunately, all the shots studied in Section 6.3 were very similar. Once the procedure has been streamlined, shots with varying elongation and varying gains should be run in an effort to scan the Alcator C–Mod operating space.

Appendix A

Interpretation of the Hankel Singular Values

The HSV's are the singular values of the mapping from past inputs to future outputs. To see this, rewrite Eq. 4.3 for $\vec{x}(t = t_0) = \vec{0}$, $t_0 = -\infty$, $\vec{u}(t) = \vec{v}(-t)$ for $t < 0$, $\vec{u}(t) = 0$ for $t > 0$ and $\mathbf{D} = \mathbf{0}$:

$$\vec{y}(t) = \mathbf{C}\exp(\mathbf{A}t)\vec{x}_0 \equiv \Gamma(t)\left[\vec{v}(t)\right] \tag{A.1}$$

where

$$\vec{x}_0 \equiv \int_0^\infty \exp(\mathbf{A}\tau)\mathbf{B}\vec{v}(\tau)d\tau \tag{A.2}$$

$\Gamma(t)$ is a time dependent integral operator mapping the input for $t < 0$ to the output for $t > 0$. Let us suppose that $\sigma_{\Gamma i}$ is a singular value of this operator with $\vec{v}(t)$ as the corresponding (time–dependent) eigenvector, i.e.,

$$\Gamma^H(t)\left[\Gamma(t)\left[\vec{v}(t)\right]\right] = \sigma_{\Gamma i}^2\vec{v}(t) \tag{A.3}$$

where

$$\Gamma^H(t)\left[\vec{y}(t)\right] \equiv \int_0^\infty \mathbf{B}^H \exp\left[\mathbf{A}^H(t+\tau)\right]\mathbf{C}^H\vec{y}(\tau)d\tau$$

Using the definition of the operator and its Hermitian, the definition of the observability grammian $\mathbf{Q}$, Eq. 4.5, and Eq. A.2 it can be shown that:

$$\Gamma^H(t)\left[\Gamma(t)\left[\vec{v}(t)\right]\right] = \mathbf{B}^H \exp(\mathbf{A}^H t)\mathbf{Q}\vec{x}_0 \tag{A.4}$$

Using Eqs. A.3 and A.4, we get (Glover [45]):

$$\mathbf{PQ}\vec{x}_0 = \sigma_{\Gamma i}^2 \vec{x}_0 \tag{A.5}$$

which is equivalent to Eq. 4.8, the definition of the HSV's.

Bibliography

[1] Sykes, A., Turner, M.F., et al., in *Proceedings of the 11th European Conference on Controlled Fusion and Plasma Physics*, Aachen (EPS Petti–Lanci, Switzerland, 1983), Vol. 2, pp. 363.

[2] Troyon, F., Gruber, R., et al., Plasma Phys. Contol. Fusion **26** (1984), 209.

[3] Goldston, R.J., Plasma Phys. Contol. Fusion **26** (1984), 87.

[4] Yamazaki, K., Amano, T., et al., Nuclear Fusion, **25** (1985), 1543.

[5] Lazarus, E.A., Chu, M.S., et al., Phys. Fluids B **3** (1991), 2220.

[6] Freidberg, J.P., *Ideal Magnetohydrodynamics*, Plenum Press, New York (1987).

[7] "ITER Blanket Shield and Material Data Base," ITER Documentation Series, No.29, IAEA, Vienna (1991).

[8] Bertolini, E., Mondino, P.L., and Noll, P., Fusion Technology, **11** (1987), 71.

[9] Noll, P., Aigle, R., et al., in *Proceedings of the 11th Symposium on Fusion Engineering, Austin, 1985*, Vol. 1, pp. 33.

[10] Garribba, M., Ciscato, D., et al., in *Proceedings of the 15th Symposium on Fusion Technology, Utrecht, 1988*, Vol. 2, pp. 1658.

[11] Garribba, M., private communication.

[12] Lazarus, E.A., Lister, J.B., et al., Nuclear Fusion, **30** (1990), 111.

[13] Lister, J.B., Lazarus, E.A., et al., Nuclear Fusion, **30** (1990), 2349.

[14] Walker M.L., Humphreys, D.A., and Nerem, A., *Toward Integrated Digital Control of the DIII–D Tokamak*, General Atomics Rept. GA–A21481, 1993.

[15] Albanese, R., Blum, J., et al., *Numerical Studies of the Next European Torus via the PROTEUS Code*, paper presented at the 12th Conf. on Numerical Simulation of Plasmas, San Francisco, 1987.

[16] Gruber, O., Gernhardt, J., et al., in *Proceedings of the 17th Symposium on Fusion Technology, Rome, 1992*, Vol. 2, pp.1042.

[17] Braams, B.J., Jilge, W., and Lackner, K., Nuclear Fusion, **26** (1986), 699.

[18] Jardin, S.C., Pomphrey, N., and DeLucia, J., J. Comput. Phys., **66** (1986), 481.

[19] Bruhns, H., Cha, S., et al., in *Proceedings of the 15th Symposium on Fusion Technology, Utrecht, 1988*, Vol. 2, pp. 1653.

[20] Woyke, W., Bruhns,H., et al., in *Proceedings of the 15th Symposium on Fusion Technology, Utrecht, 1988*, Vol. 2, pp. 1648.

[21] Bottura, L., Albanese, R., et al., in *Proceedings of the 17th Symposium on Fusion Technology, Rome, 1992*, Vol. 1, pp. 699.

[22] Albanese, R., Bottura, L., et al., in *Proceedings of the 17th Symposium on Fusion Technology, Rome, 1992*, Vol. 1, pp. 684.

[23] Marcus, F.B., Hofmann, F., et al., Nuclear Fusion, **30** (1990), 1511.

[24] Hofmann, F., and Jardin, S.C., Nuclear Fusion, **30** (1990), 2013.

[25] Ward, D.J, et al., J. Comput. Phys., **104** (1993), 221.

[26] Ward, D.J., and Hofmann, F., Nuclear Fusion, **34** (1994), 401.

[27] Ward, D.J., and Jardin, S.C., Nuclear Fusion, **32** (1992), 973.

[28] Crisanti, F., and Santinelli, M., in *Proceedings of the 13th Symposium on Fusion Engineering, Knoxville, 1989*, Vol. 2, pp. 913.

[29] Humphreys, D.A., and Yoshino, R., *JT-60 Upgrade Vertical Stability Experiments and Analysis*, Japan Atomic Energy Research Institute Rept. JAERI-M 92-069, 1992.

[30] Humphreys D. A., and Hutchinson I. H., *Filament-Circuit Analysis of Alcator C-Mod Vertical Stability*, Plasma Fusion Center Rept., PFC/JA-89-28, Massachusetts Institute of Technology, 1989.

[31] Albanese, R., Coccorese E., et al, Nuclear Fusion, **29** (1989), 1013.

[32] Humphreys D. A., and Hutchinson I. H., Fusion Technology, **23** (1993), 167.

[33] Haney S. W., and Freidberg J. P., Phus. Fluids B, **1** (1989), 1637.

[34] Jardin, S.C., and Larrabee, D.A., Nuclear Fusion, **22** (1982), 1095.

[35] Hutchinson I.H., Nuclear Fusion, **29** (1989), 2107.

[36] Golub G. H., and Van Loan C. F., *Matrix Computations*, 2nd ed., The Johns Hopkins University Press, Baltimore (1989).

[37] Press W. H., Flannery B. P., Teukolsky S. A., and Vetterling W. T., *Numerical Recipes*, Cambridge University Press, Cambridge, (1986)

[38] Pillsbury, R. D. Jr, *SOLDESIGN User's Manual*, Plasma Fusion Center Report PFC/RR-91-3, Massachusetts Institute of Technology, 1991.

[39] Grimm, R.C., Greene J.M., et al., Meth.. Comput. Phys., **16** (1976), 253.

[40] Johnson, J.L., Dalhed, H.E., et al., J. Comput. Phys., **32** (1979), 212.

[41] Friedland B., *Control System Design*, McGraw-Hill Book Co., New York (1986).

[42] Neilson G. H., Dyer G. R., and Edmonds P. H., Nuclear Fusion, **24** (1984), 1291.

[43] Seidel U., Lackner K., Lappus G., Preis H., Woyke H., *Plasma Position Control in ASDEX-Upgrade*, from *Tokamak Start-Up*, edited by H. Knoepfel, Plenum (1986).

[44] Hofmann F., Pomphrey N., and Jardin S. C., Nuclear Fusion, **32** (1992), 897.

[45] Glover, K., Int. J. Control, **39** (1984), 115.

[46] Moore, B. C., IEEE Trans. on Automat. Contr., **AC-26** (1981), 17.

[47] Safonov, M. G. and Chiang, R. Y., IEEE Trans. on Automat. Contr., **TA-7** (1988), 1036.

[48] Chiang R. Y., Safonov M. G., *Robust-Control Toolbox*, The MathWorks Inc., Natick (1988).

[49] Lao, L.L., St. John, H., et al., Nuclear Fusion, **25** (1985), 1611.

[50] Horne, S., Greenwald, M., et al., in *Proceedings of the 15th Symposium on Fusion Engineering, Hyannis, 1993*, Vol. 1, pp. 242.